Development and Validation of an Active Grille Shutter Testing Platform

by

Shaurya Rana

A thesis submitted to the
School of Graduate and Postdoctoral Studies in partial
fulfillment of the requirements for the degree of

Master of Applied Science in Automotive Engineering

Department of Automotive, Mechanical and Manufacturing Engineering

Faculty of Engineering and Applied Science

University of Ontario Institute of Technology (Ontario Tech University)

Oshawa, Ontario, Canada

September 2020

THESIS EXAMINATION INFORMATION

Submitted by: **Shaurya Rana**

Master of Applied Science in **Automotive Engineering**

Thesis title: Development and Validation of an Active Grille Shutter Testing Platform

An oral defense of this thesis took place on August 31, 2020, in front of the following examining committee:

Examining Committee:

Chair of Examining Committee	Dr. Sayyed Ali Hosseini
Research Supervisor	Dr. Martin Agelin-Chaab
Examining Committee Member	Dr. Dipal Patel
Thesis Examiner	Dr. Amirkianoosh Kiani

The above committee determined that the thesis is acceptable in form and content and that a satisfactory knowledge of the field covered by the thesis was demonstrated by the candidate during an oral examination. A signed copy of the Certificate of Approval is available from the School of Graduate and Postdoctoral Studies.

ABSTRACT

In this thesis, a testbench is developed for testing the functionality of Active Grille Shutters (AGS) and radiators in wind tunnels. Additionally, a generic pressure plate is designed to mimic commercial radiators, and a testing procedure is developed for AGS testing. Together, they provide a comprehensive and consistent platform for AGS testing with or without the radiator in a wind tunnel. The platform has been validated using an actual test vehicle in a full-scale wind tunnel. The results show that the testbench produces data consistent with those obtained from the actual test vehicle for validation. Furthermore, leakage characteristics of the testbench were quantified and can be used to replicate the engine bay conditions of any production vehicle.

Keywords: Aerodynamics, Active Grille Shutter (AGS), radiator, condenser, pressure drop, testbench, test platform, DrivAer model, engine bay flow, ANSYS, Fluent, simulation, pressure plate, wind tunnel.

AUTHOR’S DECLARATION

I hereby declare that this thesis consists of original work of which I have authored. This is a true copy of the thesis, including any required final revisions, as accepted by my examiners.

I authorize the University of Ontario Institute of Technology (Ontario Tech University) to lend this thesis to other institutions or individuals for scholarly research. I further authorize the University of Ontario Institute of Technology (Ontario Tech University) to reproduce this thesis by photocopying or by other means, in total or in part, at the request of other institutions or individuals for scholarly research. I understand that my thesis will be made electronically available to the public.

Shaurya Rana

SHAURYA RANA

STATEMENT OF CONTRIBUTIONS

I hereby certify that I am the sole author of this thesis and that no part of this thesis has been published or submitted for publication. I have used standard referencing practices to acknowledge ideas, research techniques, or other materials that belong to others. Furthermore, I hereby certify that I am the sole source of the creative works and inventive knowledge described in this thesis.

ACKNOWLEDGMENTS

First and foremost, I would like to thank John Komar, the Executive Director at ACE, and the ACE management for funding the research and always inspiring me to do better. I would like to thank my supervisor, Dr. Martin Agelin-Chaab, Associate Professor in the Department of Automotive, Mechanical and Manufacturing Engineering, for his continued guidance, mentoring, and support, without which I could not even have dreamt of embarking on this journey.

I would like to thank my parents for their constant moral support and words of motivation which helped me get through tough times.

The assistance and guidance of the executives and engineers at ACE, including, Gary Elfstrom, Patrick Smith, Warren Karlson, Andrew Norman, Anthony Van De Wetering, Kevin Carlucci, Randy Burnet, Eric Villeneuve, and Vijyat Bhalla, was detrimental in realizing the outcome of this research endeavor. Furthermore, special thanks are due for Gord Koehne and Victor Mazzuocco, whose advice and in-depth knowledge of machining, fabrication, and experimental testing proved to be pivotal for this thesis.

I would also like to thank my friend, Branson Chea, for his help with the numerical simulations.

TABLE OF CONTENTS

LIST OF TABLES

CHAPTER 3

CHAPTER 4

APPENDIX E

LIST OF FIGURES

CHAPTER 1

CHAPTER 2

CHAPTER 3

CHAPTER 4

CHAPTER 5

APPENDIX

LIST OF ABBREVIATIONS AND SYMBOLS

ABBREVIATIONS

ACE	Automotive Centre of Excellence
AGS	Active Grille Shutter
ANSYS	Analysis of Systems
CWT	Climatic Wind Tunnel
DSA	Digital Sensor Array
FKFS	Forschungsinstitut für Kraftfahrwesen und Fahrzeugmotoren Stuttgart
GMC	General Motors of Canada
MAST	Multi-Axis Shaker Table
OEM	Original Equipment Manufacturer
PLA	Polylactic Acid
SAE	Society of Automotive Engineers

SYMBOLS

C_p	Specific heat capacity (J kg^{-1} K^{-1})
d_h	Hydraulic/equivalent diameter (mm)
E	Total energy (J)
f	Area ratio of a grid, orifice, or perforated plate etc. = $\Sigma \frac{f_{or}}{F_1}$
F_1	Clear area of the grid

f_{or}	Area of one orifice in the plate
k	Turbulence kinetic energy (J/kg)
k_T	Thermal conductivity (W m^{-1} K^{-1})
l	Length of flow segment
p	Pressure (Pa)
Δp	Pressure drop across the radiator
Q	Dynamic pressure (Pa)
ΔQ	Change in dynamic pressure (Pa)
Re	Reynold’s Number
v	Velocity (m/s)
w_1	Wind speed (m/s)
$\zeta_{radiator}$	Coefficient of hydraulic resistance for the radiator
ζ_{plate}	Coefficient of hydraulic resistance for the pressure plate
λ	Friction coefficient
τ	$f.(\frac{l}{d_h})$
φ	Number of holes
μ	Viscosity (Pa s)
ρ	Density of air (1.179kg/m^3)

Chapter 1 Introduction

1.1 Background

Automobiles of the modern-day and age carry hefty engines that are capable of producing huge amounts of torque and acceleration. Moreover, these engines produce a lot of heat during their normal operation, and even more so when the driver puts a greater demand on it. The engine cooling system thus has a major role to play in this aspect.

The main components of the engine cooling system include the radiator, cooling fan, pressure cap, and reserve tank, coolant pump, thermostat, and the coolant itself, which may be some artificially engineered organic compound or simply water. The major component is the radiator, without which the heat transfer would not be possible. It is basically a heat exchanger that is mounted in front of the engine block in a vehicle to absorb heat from the engine block via the coolant which is circulated in and around the engine block. It absorbs heat from all the components and then goes to the radiator inlet. It then passes through the rows of radiator tubes, thereby transferring most of the heat to the tubes. Radiator fins are lodged in between these rows of tubes and they absorb this heat. These fins have a large surface area collectively and are thus able to release the heat to the intake air that flows into the engine bay.

There are several different types of radiators and their fin designs, but the most commonly used in automobiles is the corrugated louvered fin-type (crossflow plastic aluminum radiator) since the heat transfer coefficient for this design is comparatively higher than all other types (Manglik and Bergles, 1995; Badgujar et al., 2018; Mohanta et al., 2019; Khot and Thombare, 2014). When air passes through the radiator core, it experiences a pressure drop due to the large blockage offered by the radiator surface. This increases the velocity of the air and the air leaving the radiator has low pressure, but high velocity (Manglik and Bergles, 1995). The cooling fan is installed just behind the radiator to mechanically increase the velocity of air to further improve circulation in the engine bay region.

There are many different techniques to measure the flow velocity and/or the pressure drop across the radiator, which can be used to estimate the cooling effectiveness of the radiator. Hot film/hot wire anemometers, vane anemometers, and pressure probes are some of the techniques widely used to measure the air velocity and/or the pressure drop across the radiator core (SAE J2082, 2018).

An Active Grille Shutter (AGS) is an innovation that is used to control the ram airflow into the radiator and hence the engine bay region to reduce aerodynamic drag acting on the vehicle. The AGS system is relatively a new innovation for the introduced in the automotive sector recently. Its operation is controlled by an on-board computer that programs it to open to any degree according to the speed of the vehicle, temperature of the coolant, and other relevant parameters (Team Ford, 2018).

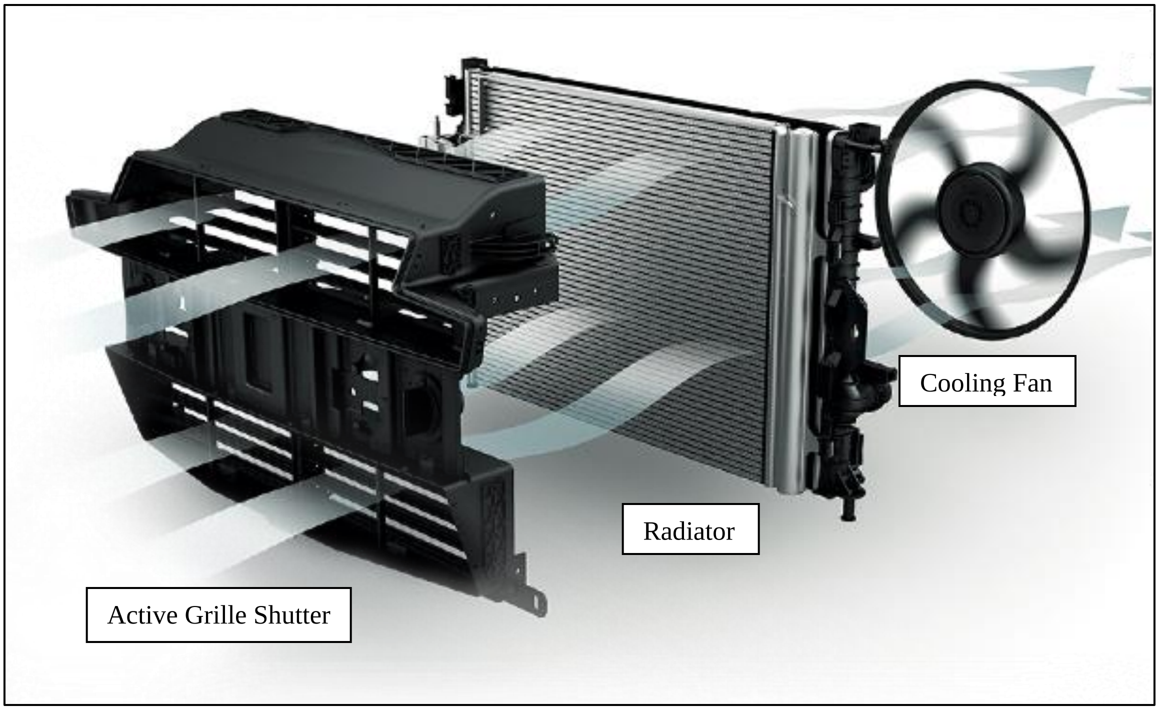

Figure 1.1 Active Grille Shutter arrangement (Ford Australia, 2020)

The AGS system is located between the condenser-radiator combination and the front grill of the vehicle. This setup has been simplified to depict only the important components as shown in Figure 1.1. The drag experienced by the vehicle reduces when the grille is in a closed position as the ram air cannot flow into the engine bay region and is directed into and out through the wheel wells. This allows the vehicle to move more efficiently through the air as it reduces the drag force acting on the vehicle and makes it 6-7% more slippery (Team Ford, 2018). This also reduces the fuel consumption because of reduced drag force on the vehicle. In addition, the engine warm-up time decreases when the grille is closed because the ram air is prevented from entering the engine bay region.

However, the testing procedure for an AGS system is neither well defined nor studied in-depth. Most companies that have implemented AGS in their vehicles keep the testing procedure on a need-to-know basis only. Every manufacturer has its own testing procedure. Many automotive manufacturers, such as the General Motors of Canada (GMC), etc. have private internal documents in which every aspect of their AGS, ranging from the electronic operation to the mechanical parts to performance, have been individually specified and the AGS must pass all the standards to be eligible for being used in an automobile. Moreover, there is hardly any literature that has been published in this regard, and whatever is available covers only the basic aspects of AGS operation while the testing methods that are used are rudimentary.

1.2 Motivation

As of today, there exists no standardized method to test the function and operating characteristics of an AGS. In fact, there is no way to compare the operating parameters related to the different AGS designs available in the market and ascertain which configuration yields the best performance in terms of drag reduction resulting from blocking incoming air from entering the engine bay area. AGS models are designed for specific vehicles, so if OEMs wish to test different AGS designs, they have to test several vehicles in a wind tunnel which is neither a cost-effective nor a time-saving procedure either. Most procedures described in literature try to measure the operating efficiency of the stepper motor that is used to operate the fins of AGS. A few SAE papers have also tried to test for the airflow and leakage through the grille when it is open, partially open, or completely closed by placing a radial fan in front of the AGS and installing vane anemometers behind it, sealing the whole section and creating an isobaric chamber. But these procedures only look at the AGS as an independent entity whereas in real-life application of an AGS is between the front grille and the condenser, followed by the rest of the engine arrangement. The effect of all these factors cannot be ignored in terms of stagnation pressure at the front, being confined in a minimal air leakage design, and the back pressure resulting from the condenser-radiator combination, the engine and the other parts in the engine bay region. Since the AGS is made to improve the cooling performance of the cooling system and it also helps in reducing the aerodynamic drag on the vehicle, a testbench design that can accurately test AGS performance is required. Thus, it is imperative to develop a general and standardized testbench that produces repeatable, uniform, and industrially acceptable results in a wind tunnel environment.

1.3 Objectives

As stated above, the lack of a standardized AGS testing procedure can lead to errors that are difficult to detect and eliminate. The objective of this research endeavor is to develop a simplified AGS testbench and procedure that provides consistency and uniformity to AGS testing.

The specific objectives are:

I. Design and fabricate a testbench that can test an AGS with or without a radiator.

II. Conduct experimental tests on an AGS with a radiator on the testing platform.

III. Measure the dynamic pressure behind the AGS at different wind speeds and fin positions.

IV. Define the operating characteristics of the testbench by determining the leakage parameters of the seals around the radiator.

V. Validate the results from the testbench by comparing it with a real on-road vehicle.

VI. Develop a pressure plate mimic the radiator’s pressure drop and acts as a generic radiator for future tests.

1.5 Thesis structure

This thesis is organized into 6 chapters as follows. Chapter 1 provides introductory background, motivation, and objectives of the thesis. Chapter 2 consists of the literature review of relevant studies in the field of radiators and AGS study. Chapter 3 focuses on the design and fabrication of the testbench. The pressure measurement techniques used in this study are explained in detail. Light has been shed on the method to design a pressure plate to replace the radiator by effectively mimicking the pressure drop across the radiator. Chapter 4 discusses the methodology as well as the experimental and numerical techniques employed in this study. It also reports an AGS testing procedure that can be used for future tests. Chapter 5 covers the analysis and discussion of the experimental and numerical results. Finally, Chapter 6 reports the conclusions and recommendations from the study.

Chapter 2 Literature Review

A comprehensive literature review was conducted to find all the relevant research that has been conducted in the field of radiator and active grille shutter testing. Additionally, since this research involves the use of pressure measurement to evaluate the effectiveness and performance, different types of pressure measurement techniques are reviewed.

2.1 Radiator Research

There are very few research papers available that actually analyze the airflow across the radiator. Most of the available research is focused on the utilization and optimization of radiator operation using different types of nanofluids and/or specially engineered fluids. Manglik and Bergles (1995) tested for the heat transfer and pressure drop correlation for rectangular offset fin strip type radiator. They collected and tabulated all the preceding research regarding the heat transfer characteristics, J, the friction factor, F, and also came up with a typical relationship between J and F. According to their findings, the value of J and F depends upon the fin geometric parameters, $\boldsymbol{\alpha}$ (ratio between the transverse spacing, *s,* and the height, *h*), $\boldsymbol{\delta}$ (ratio between the thickness, *t,* and the fin length, *l*), $\boldsymbol{\gamma}$ (ratio between the thickness, *t* and the transverse spacing, *s*) and Reynold's number. Khot and Thombare (2015) performed a synopsis of radiator performance evaluation and testing and found that radiator performance can be determined by two methods, namely – 1) Log mean Temperature Differential (LMDT) method; and 2) Effectiveness and Number of Transfer Units (NTU) method. The latter is more widely accepted, as it is robust, accurate, and time-saving. It is basically used to calculate the heat transfer rate in all kinds of heat exchangers when LMDT method cannot be used due to insufficient data. For measuring airflow across the radiator, air-to-boil (ATB) ratio and specific dissipation (SD) are two parameters used in this research. The results of their experiments show that pressure drop across the radiator increases with flow rate, heat dissipation increases with flow rate and pressure drop, and thermal resistance decreases with a decrease in pressure drop.

Badgujar et al. (2018) analyzed the characteristics of cross-flow louvered fin radiator using the effectiveness – Number of Transfer Units (NTU) method. They developed an analytical model to successfully predict the heat transfer rate, coolant, and air outlet temperatures as well as the pressure drop of coolant and the ram airside. Ng et al. (2001, 2005) have published research papers regarding a new pressure-based method that they used for quantifying radiator airflow. According to this research, they used pressure tubing in the front as well as the rear of a louvered fin-type radiator to measure the pressure on each of the respective faces. A full-scale test using the above mentioned method was also carried out on a large passenger sedan, where cobra probes instead of the normal pressure tubing were employed to measure the pressure differential (Ng, 2004). By correlating pressure drop with air velocity, they found that there is good agreement of theoretical results with those derived experimentally.

The SAE Standard J1994 (2015) outlines the procedure to be followed when testing heat exchangers, including liquid to gas (radiator), liquid to liquid (shell/tube), gas to liquid (aftercooler), and gas to gas (air to air aftercooler). For testing the operating characteristics of the radiator, it is fed with a line of incoming hot water, replicating the heated coolant which comes from the engine block. The radiator is supplied with air which has a velocity comparable to that of a moving vehicle. The efficiency of the radiator is determined by its ability to cool the incoming water. However, this method completely ignores the effect of velocity and/or pressure drop across the radiator on its operating characteristics. The engine cooling is mainly affected by the amount of ram air that actually enters into the engine bay region, and the parts installed behind the front grille play a major role in determining it. The parts behind the front grille usually include the condenser, radiator, and fan module, which is abbreviated as CRFM. New vehicles are coming equipped with an AGS in front of the condensers.

SAE J2082 (2018) collates all the cooling airflow measurement techniques that have been developed since 1992. It reveals that every institution mentioned in this document had its own techniques for measuring the velocity of cooling airflow but there exists no uniform and universally accepted method yet. Different types of anemometers such as hot wire/ hot film and vane have been used in different configurations based on velocity measurements.

Pressure based techniques involving the use of pressure probes in the front and back faces of the radiator have been employed to measure the radiators' pressure drop. From this measurement, the wind speed is calculated from the graph of pressure drop. However, blockage was usually an issue with these measurement techniques. Kuthada et al. (2008) at FKFS have developed a microprobe especially for airflow measurement and successfully reduced the blockage to airflow by carefully routing the tubing along the fin lines of the radiator resulting in an extremely low blockage ratio (2%). On the other hand, only velocities greater than 2m/s can be measured successfully due to the low probe sensitivity. Furthermore, Kuthada et al. (2015) developed a radiator simulator device that had the same pressure drop across the combination of condenser and radiator surface just like in a production car (2001 Ford Mondeo) over a range of velocities. This simulator was installed in one quarter scale open grille DrivAer model to study the effects of engine bay flow.

2.2 Active Grille Shutter Research

Most of the literature that has been published is concerned with the operation of the AGS system and its optimization to improve the resultant fuel economy improvements. Research publications on flow measurement across the AGS/radiator combination barely exist, if any. Pfeifer (2014) has suggested a new method to measure airflow leakage through the AGS when it is closed. This method involves the use of a hyperbaric chamber in front of the AGS and vane anemometer on its rear end to measure leakage. The setting up of a hyperbaric chamber, however, is an extremely difficult task, and measuring the airflow leakage through anemometers is not accurate enough as they give an averaged value over time.

Zhang (2018) has employed numerical based simulations to ascertain the effect of the size of the front grille opening, including the AGS, in a detailed realistic model of the Hyundai Veloster. Cho et al. (2017) have used numerical simulations to optimize the operation of the Active Grille Shutter, based upon the speed of the simplified model vehicle. They have designed and used highly detailed front end components to get a realistic estimation for improved fuel economy. Li et al. (2018), again, have used CFD based simulations to ascertain the best operating characteristics based upon different travel speeds and lowest aerodynamic resistance to obtain optimum engine operating temperature range. As can be seen, most of the literature available in the field of AGS research is comprised of numerical simulations alone and barely any physical experimentations have been performed.

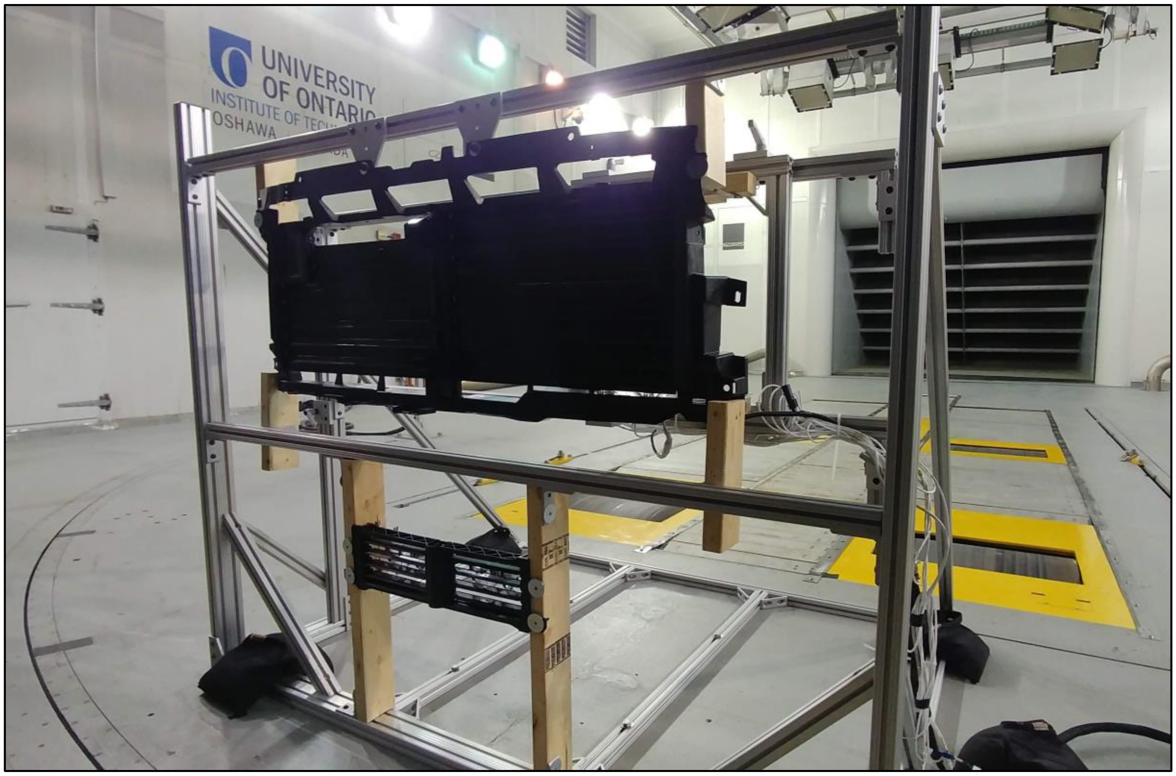

Figure 2.1 ACE's current Active Grille Shutter testing rig

The Automotive Centre of Excellence, better known as the ACE, has performed several AGS testing in the past using a makeshift rig that is shown in Fig. 2.1. This rig produced inaccurate results because the side, top, and bottom are not sealed, and there is a huge amount of air that is passing through these areas. This rig also places the AGS at a much greater height than in an actual car, which is usually around 150 to 200mm for a sedan. All these factors resulted in incorrect readings which made the testing essentially fallible.

2.3 Pressure Measurement Techniques

The Surface Vehicle Information Report, published by SAE (J2082, 2018) outlines the methods that have been used to measure cooling airflow, which is the airflow that passes through the radiator when the vehicle is in motion. Cooling airflow can be calculated either by measuring the flow velocities or by measuring the pressure of the flow and then relating it to velocity. Several flow velocity measurement techniques have been outlined, namely, anemometer based, hot-film/hot-wire anemometers, vane anemometers, etc. which have been used by numerous researchers. Each method is tailored to fit its own requirements.

Pressure measurement techniques can be categorized into two. The first is to measure the pressure drop across the radiator and compute the wind speed by plotting the pressure drop graph. The second is to find out the dynamic and static pressure within the core of the radiator and calculate the velocity based on the measurements. Berneburg and Cogotti (1993) used a cylindrical pressure probe that was installed on the face of the radiator, both front and back, to measure the difference in static pressure between the two faces. MIRA (SAE J2082, 2018) has used an array of around 30 pitot and reverse pitot tubes through the radiator faces. This method produces accurate cooling volume flow rates but is not accurate enough at low wind speeds. Ruijsink (2000) designed and used the microprobes that are inserted into the radiator core for measurement. Volvo cars used the same probe in an array of up to 30 probes of this type and resulted in a satisfactory accuracy. Kuthada et al. (2008) designed a special FKFS radiator probe that has to be inserted into the radiator to measure the pressure on its front face. The output tubing of these probes was routed such that the blockage to the flow of air through the radiator was minimal, as low as 1%. This method resulted in an accuracy that is in the range of 3% of the actual value.

Inspiration has been taken from all these methods and a special probe design, called the *Kiel probe (Kiel, 1935)*, has been chosen for pressure measurement on the rear face of the rear face of the radiator, whereas pressure tubing through the radiator core was used to measure the pressure on its front face. The Kiel probe was chosen because the measuring end of this probe is shrouded, which makes it insensitive to yaw angle changes in the direction of airflow, resulting in a more accurate measured value.

Figure 2.2 Kiel probe (United Sensor Corporation, © 2015)

Chapter 3 Design and Fabrication

This chapter gives a brief introduction about the DrivAer model and how inspiration has been drawn from this generic model to develop the testbench blueprint. Then the design and fabrication process for the testbench and pressure plate is demonstrated.

3.1 Generic Vehicle Model

Inspiration for the design of this AGS testbench is taken from the engine bay of the DrivAer Model (TUM, 2011) (Fig. 3.1). This model is an amalgamation of the design of Audi A3 and BMW 3 Series. TU Munich has released several versions of this model, which incorporate different configurations of the model, such as hatchback, notchback, fastback, smooth underbody, detailed underbody, engine bay flow, etc. (see Appendix A). This model has been created to have a uniform design for aerodynamic testing of sedans.

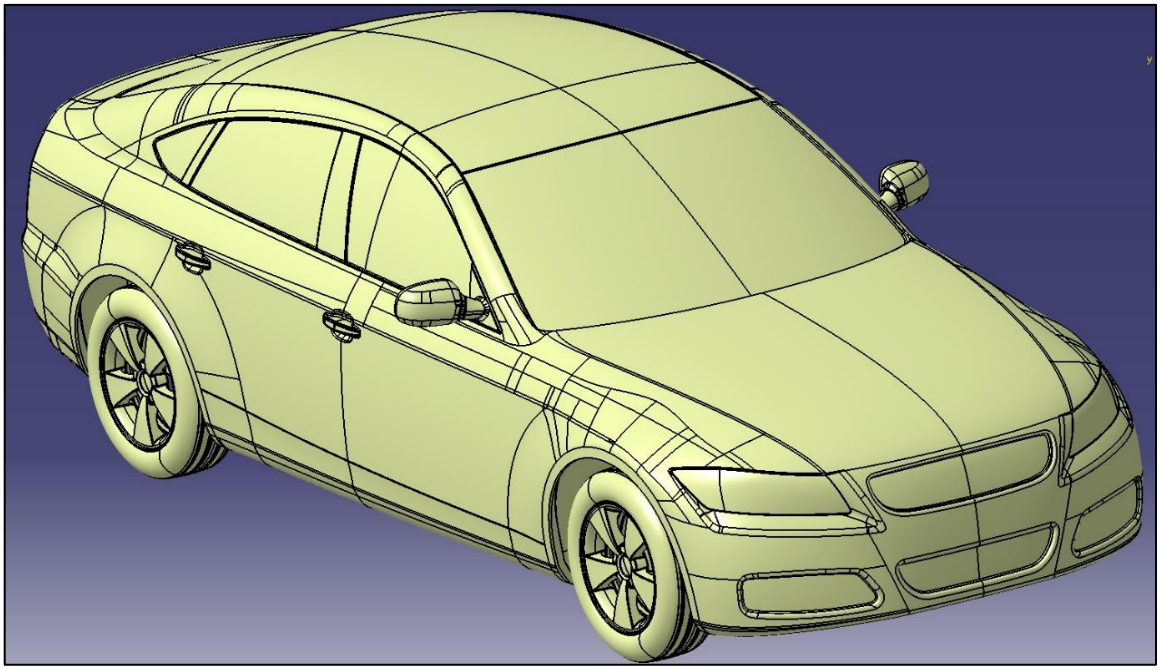

Figure 3.1 DrivAer model (TUM, 2011)

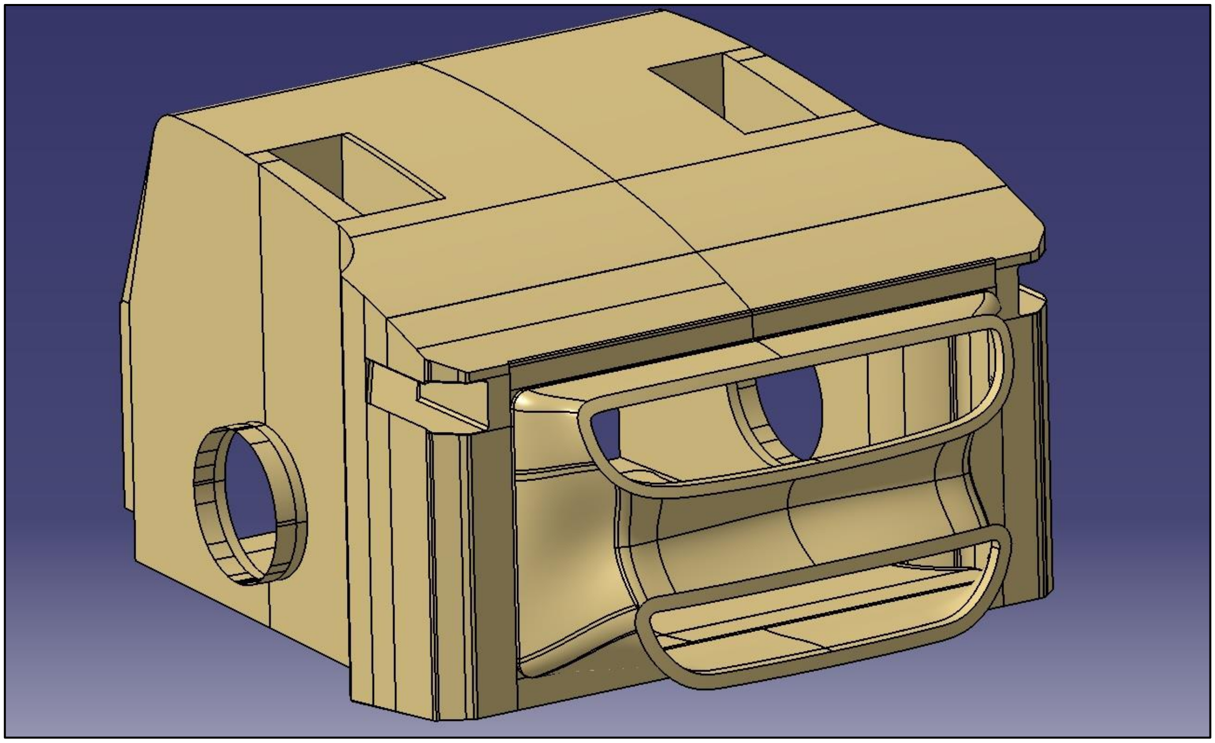

Figure 3.2 Engine bay flow design for DrivAer model (TUM, 2011)

The engine bay flow design is under the hood where the engine is held (Fig. 3.2). This design houses a simplified version of a 4-cylinder engine (Fig. 3.3), which then connects to the transmission and is then directed underneath the body of the DrivAer and out from the rear end as the exhaust.

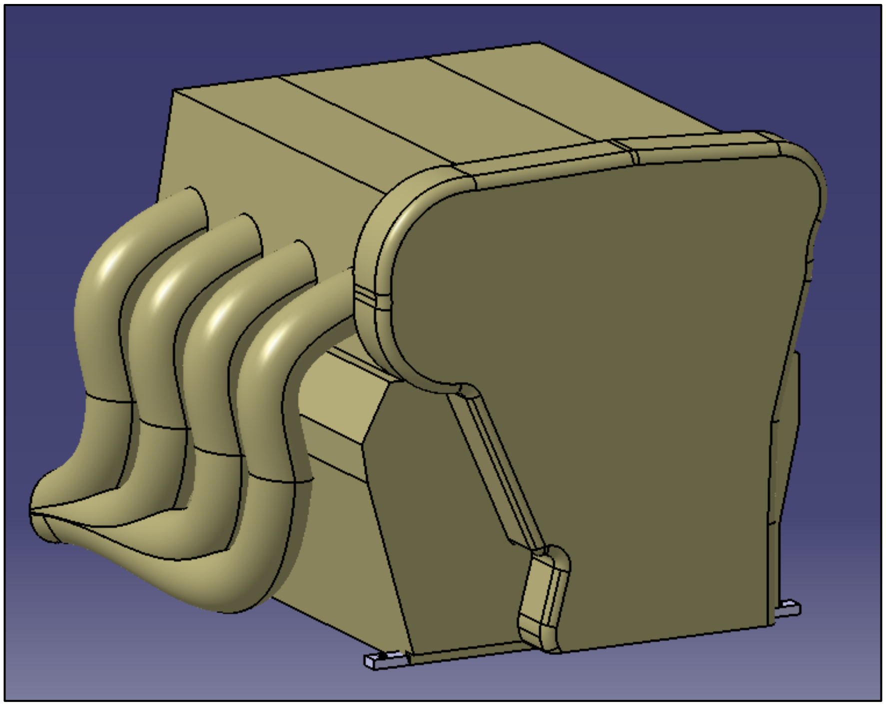

Figure 3.3 Simplified 4 cylinder engine for DrivAer model (TUM, 2011)

3.2 Testbench Design

Since the design of this testbench derives inspiration from the DrivAer model, the dimensions, shape, and size of the design should be in close approximation of the DrivAer. The intake design on the testbench and the width of the frontal area should be the same DrivAer model, as should be the ground clearance. The dimensions of the testbench should approximately be the same as the engine bay flow for the DrivAer so that it can provide similarity and acceptability to the design. The engine that would be fitted behind the radiator should also be exactly the same as the one simplified for the DrivAer model to provide an almost exact replication of the back pressure that the engine produces. Finally, the measuring equipment should be as least intrusive as possible, so as to keep the flow of air through the testbench as natural and uninterrupted as possible.

This experimental testing endeavor aims to test the performance characteristics of an AGS by using a testbench that recreates the conditions inside and outside the engine bay of an actual vehicle. The engine bay flow design has a very complex geometry with a lot of curves and crevices, which was almost impossible to manufacture without incurring an astronomical cost. So, this design from the DrivAer Model was simplified by using its projected area in two dimensions. This projected area was then used to draw a simple design that has flat faces on each side and can be easily machined. This simplification is done such that the size and shape, inside and out, are the same, and it can be easily put together using aluminum panels and an internal structure to support it (Fig. 3.4). Also, if another facility wishes to replicate this design for their purposes, it can be done, as the structure and design are uniform and repeatable.

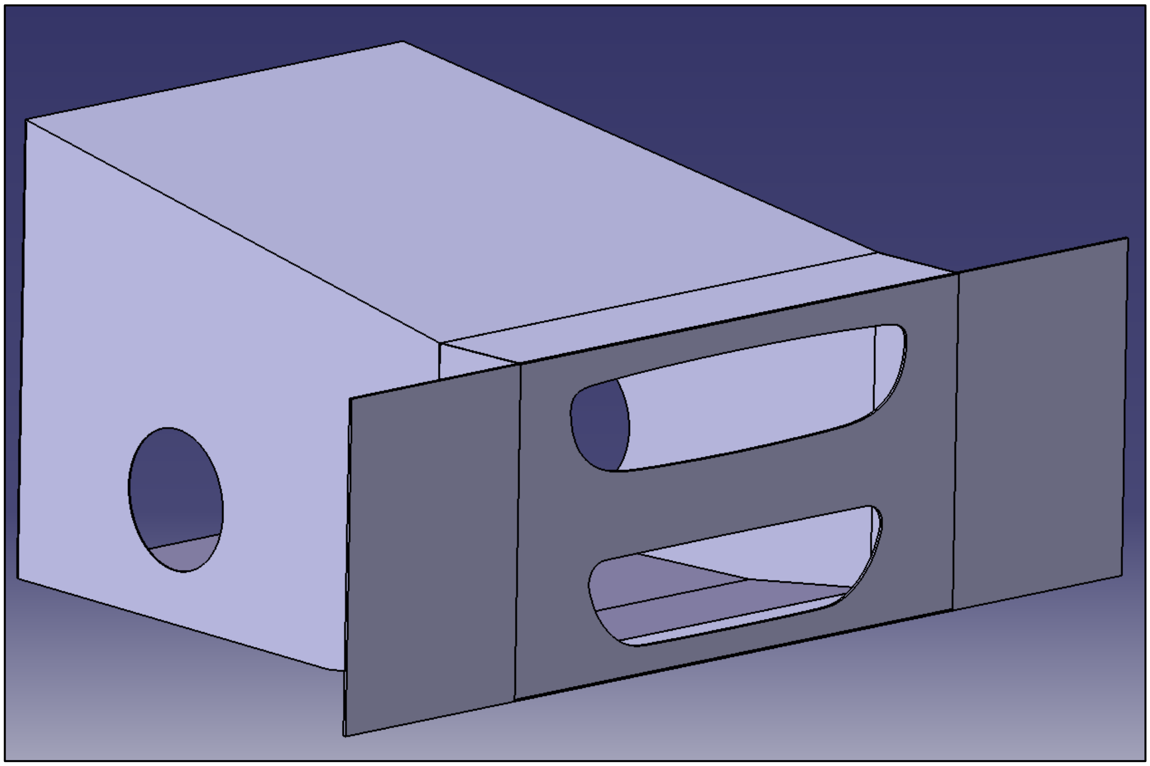

Figure 3.4 Simplified design

The entry of the ram air into the engine bay flow box is through the front intake of the model which has two small openings which are representative of the top and bottom intake in a vehicle. The plate in front of the engine bay flow box is designed to attach to it in such a way that if an OEM wants to test their specific design of the front grille, it can be water-jet cut from an aluminum plate and be attached to the testbench. This will ensure flexibility as is required by any testbench and will make it extremely useful. But for the current test, the front plate intake design is made to be the same as the one in the DrivAer model to ensure uniformity and acceptability.

Panels are attached on either side of the front plate which results in the same width as that of the frontal projected area of the DrivAer model so that it can provide an exact representation of the frontal stagnation pressure. The joint between the front plate and the rest of the testbench is made airtight so that the ram air can enter only through the designated intake area and there is no leakage into or out from the testbench. This makes the testing procedure as realistic as possible.

The AGS will be installed just behind the front plate where it will control the flow of air into the box behind by opening or closing its fins. The radiator will then be installed behind the AGS as is the case in a real vehicle. The dimensions of the intake and the distance between the front plate, AGS, and the radiator are kept exactly as they are in the DrivAer model for consistency.

A 4-cylinder engine has been simplified to be used in the DrivAer model. This simplified design of the engine is behind the radiator and the circulation fan plate in the original DrivAer model.

3.3 Testbench Fabrication

After a careful weighing of pros and cons for the prospective material to be used for the internal structure of the testbench, Aluminum T-slotted rods from 80/20 Inc. were selected as they offer the easiest machinability, rigidity, and flexibility in design as was required. Table 3.1 shows the bill of materials that were ordered for the fabrication of the internal structure of the testbench. It includes all materials ranging from the 12ft. Aluminum T-slotted heavy rods to the flanged button head socket cap screws and slide in economy T-nuts.

Table 3.1 Bill of materials for the internal structure of testbench

Number	Material ordered	Quantity
1.	1.5"×1.5" T-slotted heavy extended × 145"	8
2.	40 series M8 × 1.25 end fastener with screw	60
3.	15 series 4 hole inside corner bracket	16
4.	5-hole tee joining plate 15 series	10
5.	15 series 0 degree pivot, pivots 180 degree	4
6.	5/16-18 × 5/8" flanged button head socket cap screw and slide in economy T-nut	162
7.	15 series black adjustable hinge	6
8.	Bolt assembly for 2080 black plastic hinge	12
9.	5/16-18 × 3/4" button head socket cap screw, washer, hex nut	12

Each T-slotted rod was cut into the required length using a cutting machine that uses a revolving blade. After this, the pieces which required holes to be drilled into them for attaching them to each other, as well as access holes for the Allen key were drilled using a milling machine. All the T-slotted rods were to be joined at the ends with the help of end connectors and they were hand tapped using an M8 tap. After joining these pieces together according to the previously designed structure, the following structure was fabricated (Fig. 3.5):

Figure 3.5 Internal structure to support testbench

The next step was to get the external panels and the front plates which will serve as the intake for the design cut to dimensions. This job was given to a water jet cutting establishment that specializes in such precision jobs. The thickness of the side panels was selected to be 0.090 inches while the front plates were to be 0.187 inches, as they will face the major brunt of the wind force when kept in the wind tunnel at high speeds. After receiving the panels from the supplier, they were bolted to the frame according to their designated position (Fig. 3.6).

Figure 3.6 Front view of the testbench

The side plates were reinforced with a slant member joined at the rear surface, to prevent buffeting while the testbench is in the wind stream (Fig. 3.7).

Figure 3.7 Rear view of the testbench

The engine was 3D printed in parts, joined together using epoxy and the surface was treated to create a polished look. The material used for printing was PLA (Polylactic Acid) from AMZ3D and 5mm was used as the pigment thickness. The engine was then bolted to the floor of the testbench with the help of 4 × 3/8th inch bolts, one at each corner of the square base of the engine (Fig. 3.8).

Figure 3.8 3D printed simplified engine

To validate this testbench that is based on the design of the DrivAer model, a vehicle had to be chosen which uses an AGS and a radiator that can be easily sourced, so that the performance of the testbench can be compared against it. Also, the shape of the front intake should be similar to the DrivAer model. The vehicle hence chosen for this experimental testing was Ford Fusion 2016, because the shape of its front intake is similar to the DrivAer model, and the manufacturer for both the AGS and the radiator for this car is the same (Spectra Premium) and many suppliers stock these products. Also, during the validation phase, Ford Fusion is readily available for rental purposes making it the most viable option. Active Grille Shutter (Fig. 3.10) and the radiator (Fig. 3.9) for this vehicle were then ordered from a parts shop located in Montreal. The radiator had two pegs at the bottom, made up of plastic, which needed to be trimmed so that it could fit inside the testbench. The AGS had a protruding plastic end that extended from the structure that needed to be trimmed. The operating area of neither of the products was altered in this process to ensure reliability and acceptance.

Figure 3.9 Radiator used for testing

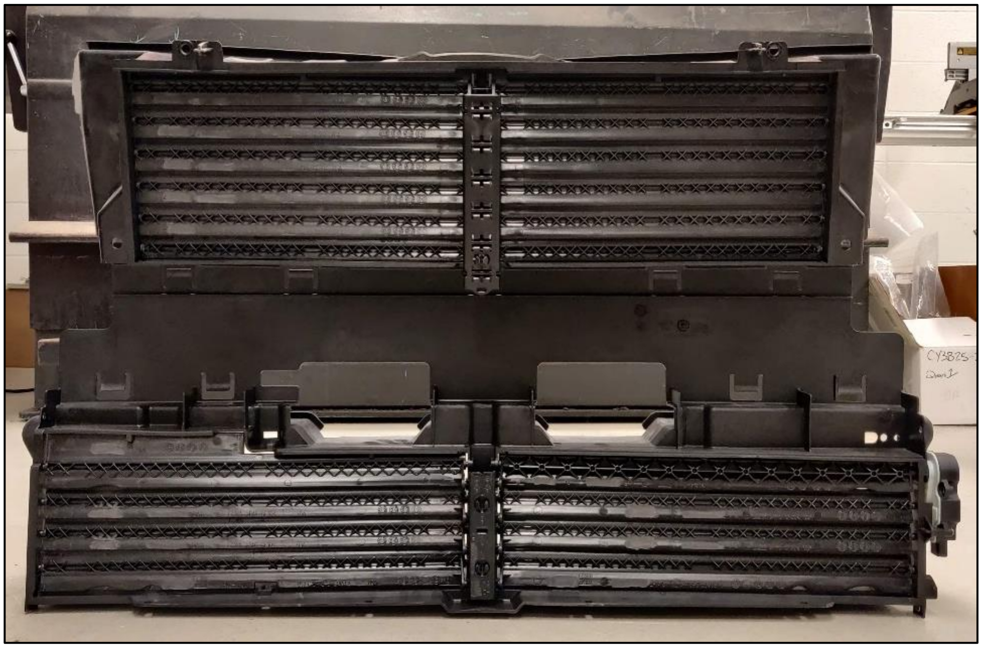

Figure 3.10 Active Grille Shutter (AGS) used for testing

The radiator was fitted in the designated area in front of the pressure probe rack (section 4.1.4) and bolted in place with the help of triangle supports from the top and bottom t-slotted rods. The sides of the radiator were then sealed with the help of cardboard and gorilla tape. This was done to make the arrangement as airtight as possible so that the air passes through the radiator face only and not from the gap at the sides, top, or bottom. Eight pressure tubing were inserted into the radiator from behind, to measure the dynamic pressure at the radiators' front face. This would help in measuring the dynamic pressure of the air that passes through the AGS vanes and reaches the radiator face in different fin positions (Fig. 3.11).

The black points indicate the positioning of the pressure tubing which were inserted from the back of the radiator and lie flush with its front surface.

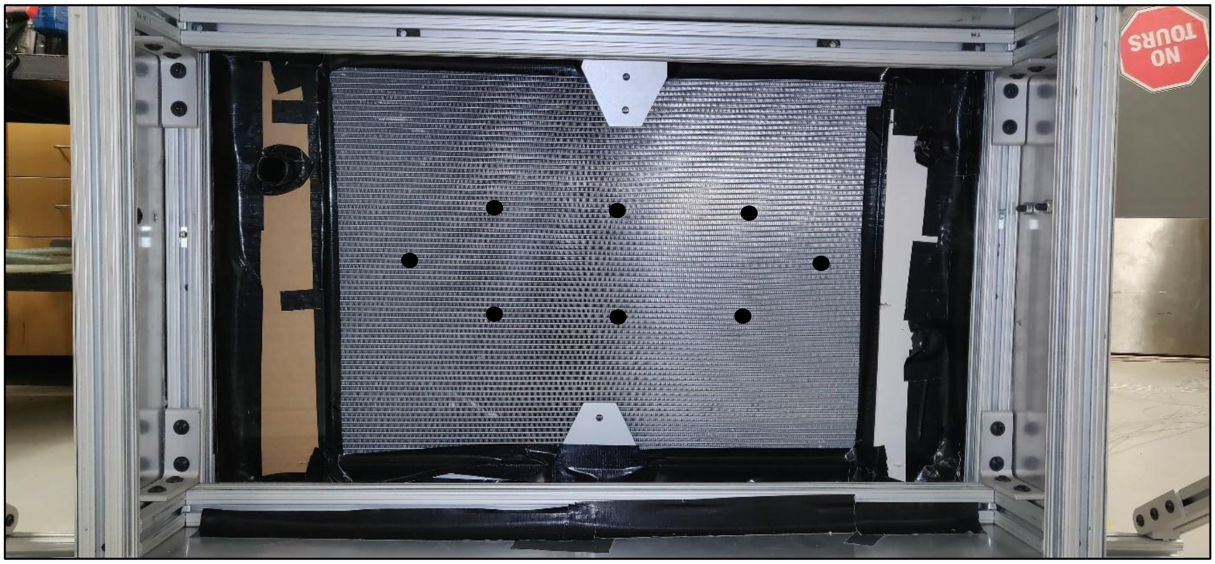

Figure 3.11 Radiator installed in testbench and sealed

The AGS was then installed in the testbench and bolted at the top but not at the bottom since it was supported against a T-slotted rod at the back and the intake plate in front of it which made the AGS immovable. The sides of the AGS were sealed and made as airtight as possible in a similar way as the radiator, by using cardboard and gorilla tape (Fig. 3.12) as this was the most effective material available at hand.

Figure 3.12 AGS installed in testbench and sealed

The front plate, with two side plates bolted to it on either side, was then installed in front of the AGS. All the joints between the aluminum panels in the structure were then sealed with an all-weather sealant using a caulking gun to make the air leakage as minimal as possible and allow the air to flow only through the designated pathways (Fig. 3.13).

Figure 3.13 Front fascia installed on testbench

To get the unsealed configuration for the AGS, all the seals on the sides, top, and bottom were removed such that the gap on either side of the AGS is open, which allows more air to flow through and reach the radiator face behind the AGS, which houses the pressure tubing.

3.4 Pressure Plate Design

The idea behind designing a pressure plate is to eliminate the source of error which may arise from the use of different radiator configurations as the porosity for each radiator varies ever so slightly because of different fin design and density. If the pressure drop across a radiator from a sedan can be replicated onto a pressure plate, it can then be used instead of the radiator in the AGS testbench and this will eliminate a big source of uncertainty and errors in measurement as this plate can be used as a benchmark. The process for designing this pressure plate is as described below.

3.4.1 Theoretical formulation

The first step is to measure the pressure loss across the radiator inside the testbench with a minimal amount of air leakage. The pressure values at the front and back of the radiator are averaged to find a mean value of pressure at the front and back respectively. Subtracting the back pressure from the front pressure gives the value of pressure drop across the radiator (*Δp*). This pressure drop was then used to calculate the coefficient of hydraulic resistance for the radiator according to the following formula:

$$\zeta_{radiator} = \frac{\Delta p}{\rho . w_1^2 / 2} \tag{3.1}$$

Where,

Δp = Pressure drop across the radiator

ρ = Density of air (1.179kg/m^3)

w_1= Wind speed (m/s)

$\zeta_{radiator}$= coefficient of hydraulic resistance for the radiator, which is calculated to be 0.6415 at the speed of 3.33m/s

The formulas used to determine the dimensions of the holes in the pressure plate to yield the same pressure drop as the radiator are as follows:

Coefficient of hydraulic resistance, $\zeta = \left(\zeta_o + \lambda . \frac{l}{d_h}\right) . \frac{1}{\bar{f}^2}$ (3.2)

Where, $\zeta_o = \left(0.5 + \tau\sqrt{1-\bar{f}}\right).\left(1-\bar{f}\right) + \left(1-\overline{f}\right)^2$ (3.3)

λ = Friction coefficient

$\tau = \mathrm{f}(\frac{l}{d_h})$

l = Length of the flow segment

d_h= hydraulic/equivalent diameter

f = Area ratio of a grid, orifice, or perforated plate = $\Sigma \frac{f_{or}}{F_1}$

f_{or} = area of one orifice in the plate

F_1 = Clear area of the grid

It was found that designing orifices in the shape of a square resulted in better utilization of the area of the pressure plate with less blockage. The length of the square was determined as, $\mathbf{a} = \sqrt{\frac{d_h^2}{2}}$. In addition, square holes are easier to cut as compared to circular holes when pressure jet cutting is used. This is because the pressure jet method cuts in small straight-line segments. These small segments are cut in a sequence to give a circle. When observed closely, it is seen that this cut is not perfectly circular as it has been formed by joining small but straight lines. On the other hand, when cutting a square, it is cut perfectly as it has straight sides. This is the reason why square holes were preferred over circular ones.

The values for λ and τ were obtained from the tables that were published by Idelchik (1989):

Table 3.2 Values of coefficient of hydraulic resistance, ζ (Idelchik, 1989)

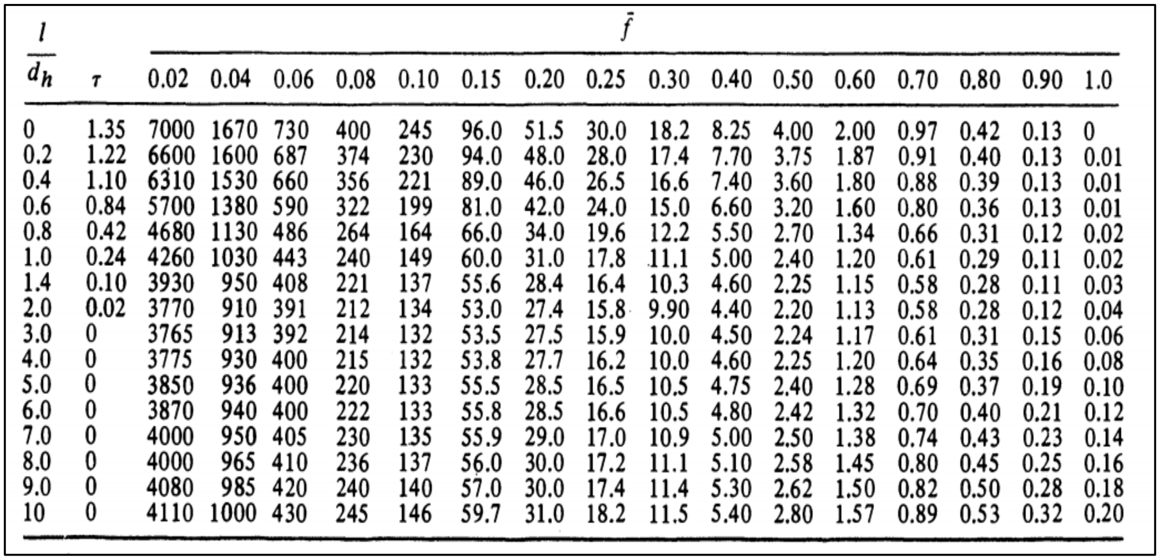

$\frac{l}{d_h}$	τ	$\bar{f}$															
		0.02	0.04	0.06	0.08	0.10	0.15	0.20	0.25	0.30	0.40	0.50	0.60	0.70	0.80	0.90	1.0
0	1.35	7000	1670	730	400	245	96.0	51.5	30.0	18.2	8.25	4.00	2.00	0.97	0.42	0.13	0
0.2	1.22	6600	1600	687	374	230	94.0	48.0	28.0	17.4	7.70	3.75	1.87	0.91	0.40	0.13	0.01
0.4	1.10	6310	1530	660	356	221	89.0	46.0	26.5	16.6	7.40	3.60	1.80	0.88	0.39	0.13	0.01
0.6	0.84	5700	1380	590	322	199	81.0	42.0	24.0	15.0	6.60	3.20	1.60	0.80	0.36	0.13	0.01
0.8	0.42	4680	1130	486	264	164	66.0	34.0	19.6	12.2	5.50	2.70	1.34	0.66	0.31	0.12	0.02
1.0	0.24	4260	1030	443	240	149	60.0	31.0	17.8	11.1	5.00	2.40	1.20	0.61	0.29	0.11	0.02
1.4	0.10	3930	950	408	221	137	55.6	28.4	16.4	10.3	4.60	2.25	1.15	0.58	0.28	0.11	0.03
2.0	0.02	3770	910	391	212	134	53.0	27.4	15.8	9.90	4.40	2.20	1.13	0.58	0.28	0.12	0.04
3.0	0	3765	913	392	214	132	53.5	27.5	15.9	10.0	4.50	2.24	1.17	0.61	0.31	0.15	0.06
4.0	0	3775	930	400	215	132	53.8	27.7	16.2	10.0	4.60	2.25	1.20	0.64	0.35	0.16	0.08
5.0	0	3850	936	400	220	133	55.5	28.5	16.5	10.5	4.75	2.40	1.28	0.69	0.37	0.19	0.10
6.0	0	3870	940	400	222	133	55.8	28.5	16.6	10.5	4.80	2.42	1.32	0.70	0.40	0.21	0.12
7.0	0	4000	950	405	230	135	55.9	29.0	17.0	10.9	5.00	2.50	1.38	0.74	0.43	0.23	0.14
8.0	0	4000	965	410	236	137	56.0	30.0	17.2	11.1	5.10	2.58	1.45	0.80	0.45	0.25	0.16
9.0	0	4080	985	420	240	140	57.0	30.0	17.4	11.4	5.30	2.62	1.50	0.82	0.50	0.28	0.18
10	0	4110	1000	430	245	146	59.7	31.0	18.2	11.5	5.40	2.80	1.57	0.89	0.53	0.32	0.20

The Reynolds number, based on the thickness of the pressure plate, varies from 5,000 to 50,000. The Reynolds number for the pressure plate is calculated as follows:

$$\mathrm{Re} = \frac{\rho.w.l}{\sigma}$$

Where, ρ = density of air

w = wind speed (m/s)

l = linear dimension (thickness of the pressure plate)

σ = viscosity (kg/m/s)

For turbulent regime ($4000 < \mathrm{Re} < 10^5$), the friction coefficient, $\lambda = \frac{0.3164}{Re^{0.25}}$; See graph c in Fig. 3.14 (Idelchik, 1989):

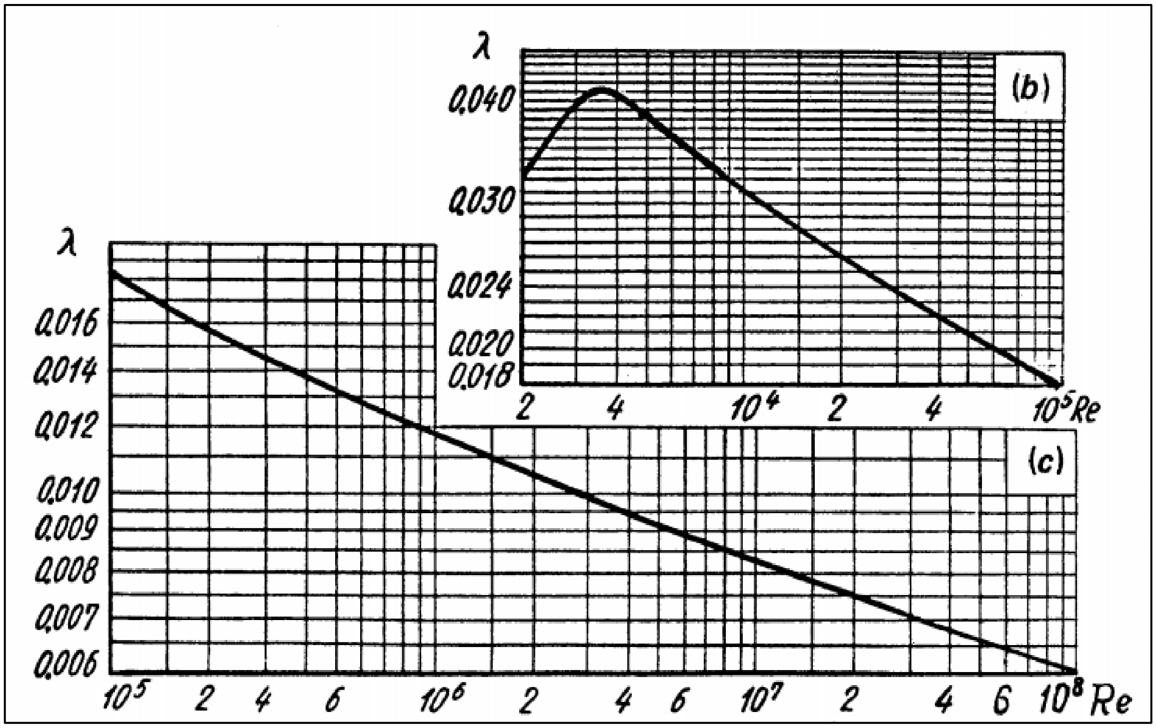

Figure 3.14 Friction coefficient, λ vs Reynolds number (Idelchik, 1989)

Using all the aforementioned formulas, the following calculations are shown for one configuration (thickness of plate, l = 0.0254m) that yielded a value of the coefficient of resistance close to that of the radiator:

Height of plate, h = 0.475m

Width of plate, w = 0.850m

Length, l = 0.0127m

Length to diameter ratio, l/d = 0.2

So, $d = 0.0127/0.2 = \mathbf{0.0635m}$

$$a = \sqrt{\frac{d_h^2}{2}} = \mathbf{0.0449m}$$

Assume the number of holes to be φ = 144, then

$$f = \Sigma \frac{f_{or}}{F_1}$$

f_{or} = Area of one orifice = $a \times a = 0.0449 \times 0.0449$;

$F_1 = h \times w = 0.475 \times 0.850$

So, $$f = 144\left(\frac{0.0449 \times 0.0449}{0.475 \times 0.850}\right)$$

$$f = \mathbf{0.7107}$$

Now, $\zeta_o = \left(0.5 + 1.1\sqrt{1 - 0.7107}\right) \times (1 - 0.7107) + (1 - 0.7107)^2 = \mathbf{0.3748}$

And, hence, $\zeta_{plate} = (0.3748 + 0.028 \times 0.4) \times \left(\frac{1}{0.7107^2}\right) = \mathbf{0.781}$

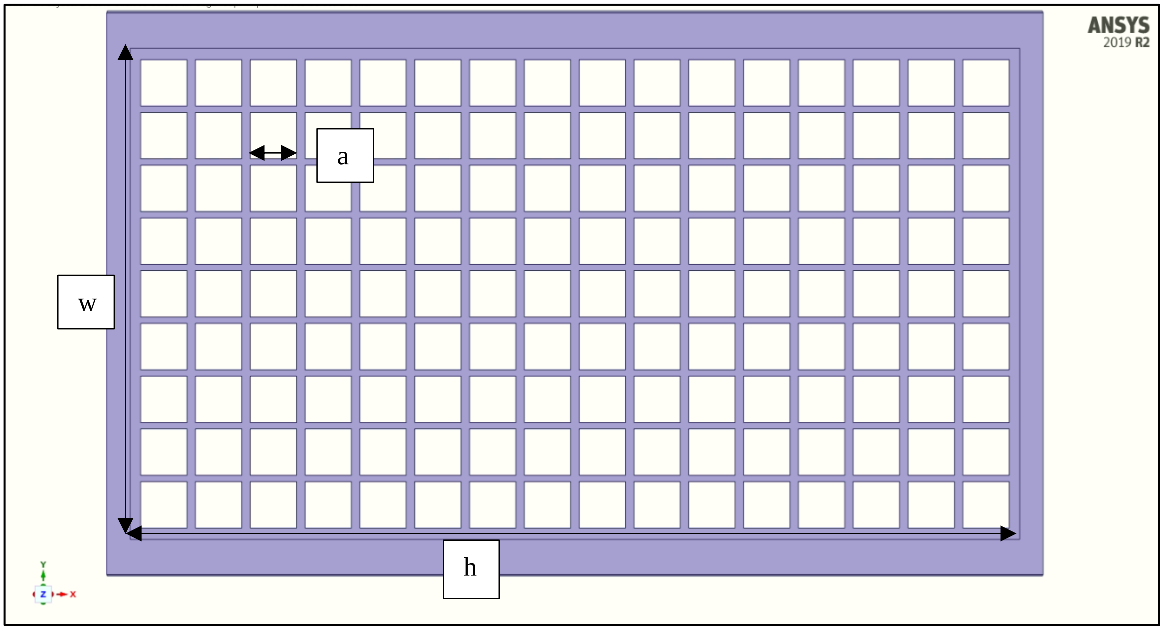

Figure 3.15 Design of preliminary pressure plate

Since the value of *l/d* and τ are limited to the ones that were available in the graph and the table, it was necessary to design the orifices in such a way so as to obtain the respective values from the published set. The idea behind setting up the values in the table was to use the number of holes, φ, in such a way that the porosity, *f*, would stay under 0.75 so that the plate can be manufactured to be sturdy and at the same time have the required number of holes in the design. It was calculated that the coefficient of hydraulic resistance for the radiator, $\zeta_{radiator}$ was 0.64. Keeping a balance between the number of holes and the porosity of the pressure plate, it was found that according to the dimensions of the plate, the maximum number of square holes of side 0.0449m was 144, i.e. 16 holes across and 9 holes in the top down direction, which gave ζ_{plate} as 0.781. Since the plate is to be installed inside the testbench, its blockage should be slightly more than the radiator, so that the blockage effect offered by the testbench can be negated. Using the same hydraulic diameter as the previous plate, a plate with circular holes was also designed, which resulted in ζ_{plate} = 0.703, which is closer to the radiator. But this plate would have been almost impossible to fabricate due to the extremely small distance between adjacent holes in the vertical direction (Fig. 3.16).

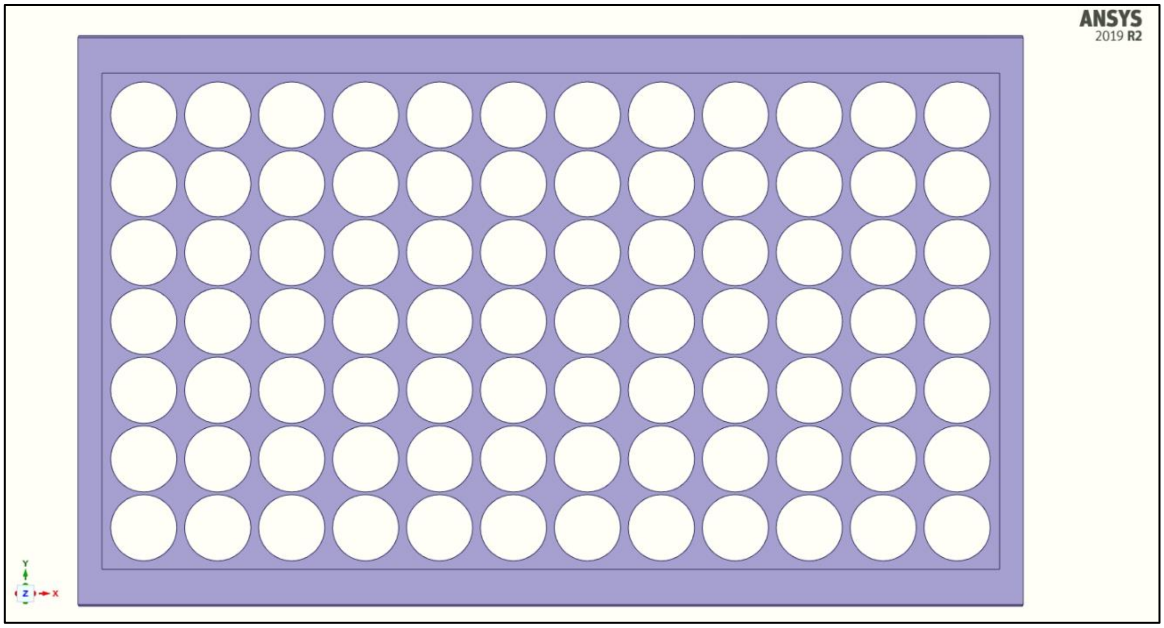

Figure 3.16 Plate with circular holes φ = 84 and 0.5 inches thick

Hence, the plate with φ = 144 and thickness 0.5 inches was selected for preliminary simulations and later fabricated for validation purposes.

3.4.2 Final pressure plate design

The results from the preliminary simulations were not as they were expected to be (see Appendix F). This plate resulted in a positive pressure drop which indicates that the flow gets decelerated as it passes through the plate. For vena contracta to occur, as is the case in the radiator, the hole size should be small enough for the airflow to contract and accelerate through. Therefore, a new pressure plate with numerous smaller circular holes was selected for simulations after simulating several other hole configurations. This plate has φ = 943 (an array of 41 × 23) and is 0.5 inches thick. Using the same formulas as before, we get:

Height, h = 0.475m; Width, w = 0.850m; Length, l = 0.0127m l/d = 0.7

So, $d = \mathbf{0.01814}\boldsymbol{m}$

Number of holes, φ = 943, then $f = \Sigma \frac{f_{or}}{F_1}$

f_{or} = Area of one orifice = $A = \pi r^2$or $\frac{\pi d^2}{4} = \frac{\pi \times 0.01814^2}{4}$;

$F_1 = h \times w = 0.475 \times 0.850$

So, $f = 943 \times \frac{f_{or}}{F_1} = \mathbf{0.7759}$

Now, $\zeta_o = \left(0.5 + 0.63\sqrt{1 - 0.7759}\right) \times (1 - 0.7759) + (1 - 0.7759)^2 = \mathbf{0.5659}$

And, hence, $\zeta_{plate} = (0.5659 + 0.0283 \times 0.7) \times \left(\frac{1}{0.7759^2}\right) = \mathbf{0.943}$

The final pressure plate design is shown in Fig 3.17:

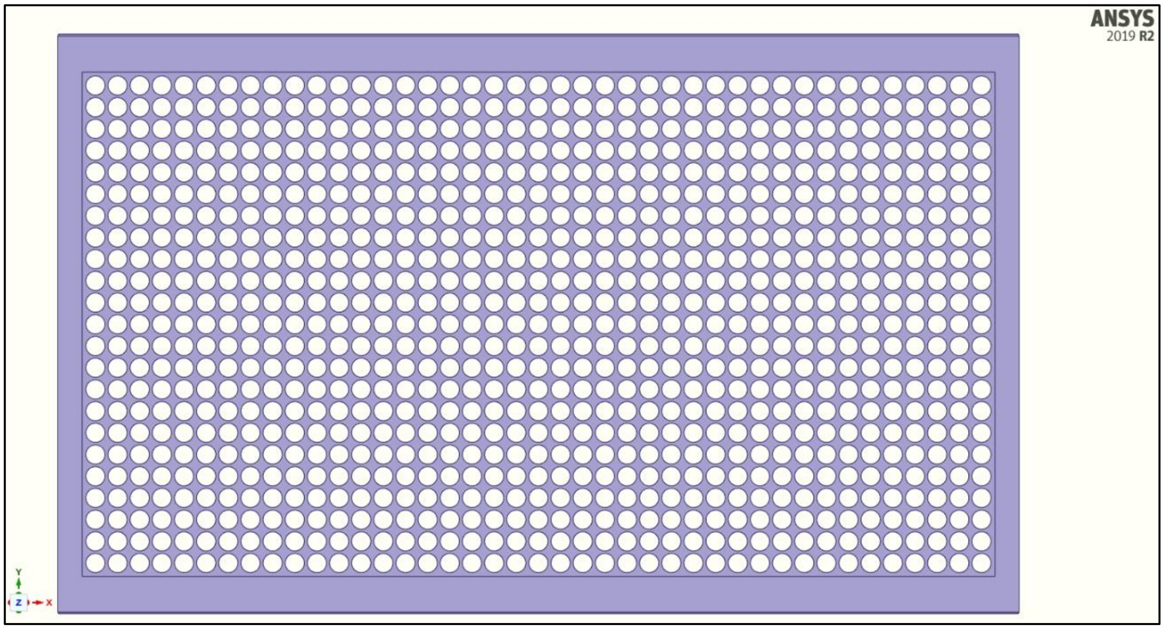

Figure 3.17 Final pressure plate design φ = 943 and 0.5 inches thick

Chapter 4: Wind Tunnel and Numerical Experiments

This chapter discusses the experimental setup for the testbench and the test vehicle at ACE. The instrumentation used for measuring the dynamic pressure in the testbench and the vehicle has been explained in detail. Background knowledge for numerical simulations has been provided and the setup for simulating the pressure plate in ANSYS Fluent has been elucidated methodically.

4.1 Wind Tunnel Experiments

4.1.1 Test facility

The tests were conducted at the Automotive Centre of Excellence, better known as ACE, at Ontario Tech University. This facility has 5 testing chambers available, namely, the Climatic Wind Tunnel (CWT), Small Climatic Chamber, Large Climatic Chamber, Four post climatic chamber, and the Multi-Axis Shaker Table (MAST) in the Hemi-Anechoic Chamber.

The CWT is a world-class, full-scale climatic wind tunnel, and more upgrades are being installed to it in the upcoming year. It is capable of producing wind speeds up to 290kmph. The temperature ranges from -40 to 60^{o}C and the relative humidity can be varied from 5 to 95%. The variable nozzle can adjust its size from 7m^2 to 13m^2 which is enough to accommodate all kinds of vehicles, ranging from a small vehicle to an articulated bus in the wind tunnel. The large chassis dynamometer is incorporated into an 11.5m turntable, so vehicles can be rotated, and test properties measured at any angle from 0^{o} to 180^{o} for crosswind development. The dynamometer can run at a max speed of 250kmph. The overhead solar array can replicate any condition of the sun, from sunrise to sunset. The wind tunnel is capable of producing snow, rain, mist, clouds, and freezing rain. Its overall dimensions are 20.1m in length, 13.5m in width, and 7.5m in height, which gives it an overall volume of 2035.125m^3.

4.1.2 Experimental setup for testbench

The testbench was prepared for the test beforehand by routing the pressure tubing from the Kiel probes through the hole in the left side panel. The AGS was sealed initially so that the sealed conditions could be tested before the unsealed conditions to save time. The testbench was then brought into the wind tunnel with the help of a forklift. It was positioned in the same longitudinal position as if it were a test vehicle, for uniformity and to avoid any discrepancies when validating the results with an actual vehicle. It was secured to the floor with the help of torqueing chains at both ends to hold it in position when the wind speed increases. The back legs of the testbench were secured in place with the help of magnetic stops behind them. Pressure tubing were then taped to the floor to prevent disfiguration due to the high wind speed and then connected to the DSA which is outside the wind stream near the control room wall of the wind tunnel (Fig. 4.1- 4.4).

Figure 4.1 Testbench setup in the wind tunnel

4.1.3 Test conditions and measurement procedure

4.1.3.1 AGS testing

The AGS in the testbench is controlled manually by turning them to each respective position. AGS on the testbench was tested for 6 different conditions, Open (sealed and unsealed) (Fig. 4.2), partially open (sealed and unsealed) (Fig. 4.3), and closed (sealed and unsealed) (Fig. 4.4), at speeds of 12, 14.4, 21.6, 28.8, 36, 43.2, 50.4, 57.6, 64.8, 72, 79.2, 86.4, 93.2, 100.8 and 108kmph. Only three AGS configurations (open, partially open, and closed) which are consistent with operating positions of the real AGS in the test vehicle used for validation. This would enable us to measure the effect of sealing the sides of the AGS and help get an idea of how much air actually leaks in from the open gaps on either side of the AGS and the radiator. Eight pressure tubing at the front face of the radiator and 7 Kiel probes at its rear face were used to measure the dynamic pressure at the radiators' front and back surfaces, respectively. These probes were also used to measure the pressure drop of air as it passes through the radiator, by subtracting back pressure from the front. The unsealed configuration of the testbench was measured for dynamic pressure twice to ensure the repeatability of data.

Figure 4.2 AGS fully open

Figure 4.3 AGS partially open

Figure 4.4 AGS closed

4.1.3.2 Radiator testing

After measuring the data for all the 6 conditions, the AGS was removed from testbench to test for the pressure drop characteristics across the radiator (Fig. 4.6). This was done to clearly define the operating characteristics of the testbench in terms of leakages. Seals at the top, bottom, and sides were removed individually in a sequence (Fig. 4.5). The pressure drop was tested for each arrangement to give us a clear idea of how the removal of each seal affects the pressure drop across the radiator. This was done to set a benchmark for pressure drop such that if an OEM requires a specified amount of air leakage, it can be replicated. The pressure drop characteristics for the radiator were tested only for 5 wind velocities, i.e. 20, 40, 60, 80, and 100kmph, to get a data trendline of the leakage that occurs with each arrangement.

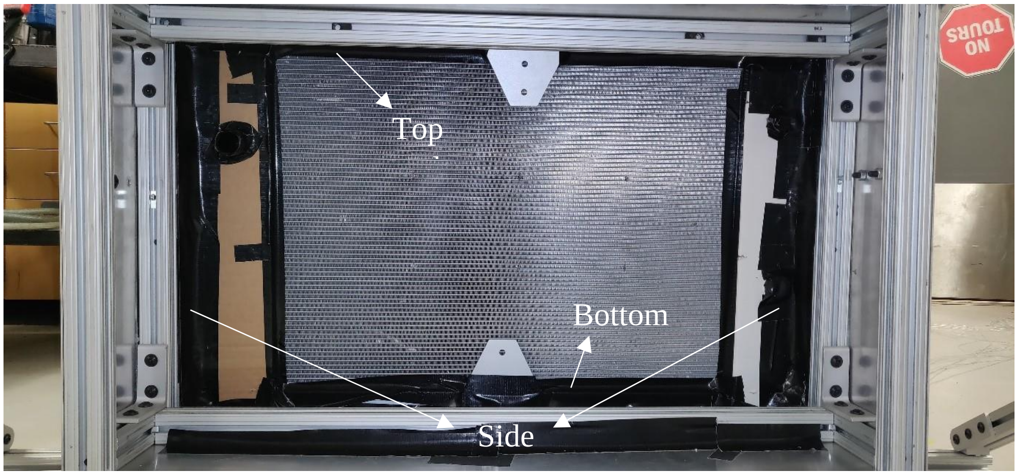

Figure 4.5 Seal terminology

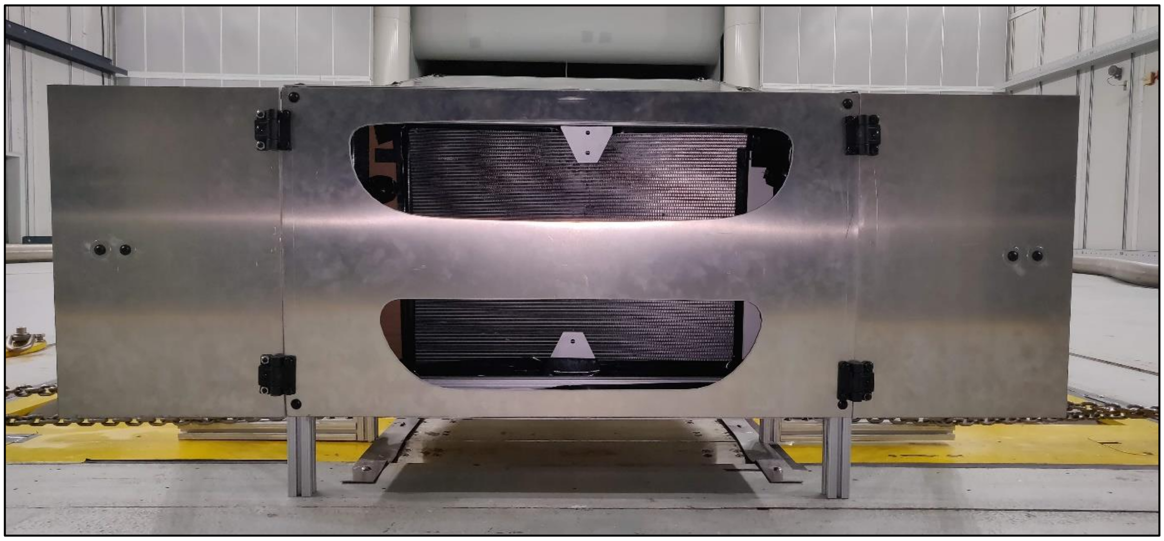

Figure 4.6 Testbench with AGS removed

The data from the testing was obtained and processed using Microsoft Excel. Each arrangement for the vehicle and the testbench had about 5500 points of dynamic pressure data measurements, and the software, specially designed by React Technologies, takes a mean of 300 points for each speed once it stabilizes. This single-shot average data is then analyzed. From this, the AGS opening conditions are analyzed.

4.1.4 Instrumentation for measurement

The most important part of this study is to measure the dynamic pressure at the front and the rear face of the radiator when it is installed inside the testbench. The radiator is the first component behind the AGS, and dynamic pressure measurement is the only reading considered in this research. If the dynamic pressure at the front face of the radiator can be measured while the AGS is installed, it gives a measurement of the velocity of air passing through the AGS vanes when they are in their different positions. This can then be extended to measure the pressure loss across the radiator also, by measuring dynamic pressure behind the radiator, which will thus define the testbench characteristics of pressure, wind speed, and leakage.

The pressure on the front face of the radiator (windward side) was to be measured using pressure tubing inserted in the radiator from behind. For the rear face (leeward side), an adjustable rack was designed and fabricated which can be hooked on to the top of the radiator or bolted to the aluminum t-slot structure behind it. This houses the pressure probes. Instead of using normal pressure probes, *Kiel Probes* were used which were supplied by *United Sensors Corporation, USA*. A Kiel Probe is a specially manufactured pressure measuring probe in which the measuring end is shrouded, which reduces the probe's sensitivity to yaw angle changes. It is used to measure the pressure values with a high level of accuracy. The adjustable rack, made up of rails with uniformly spaced holes, serves the purpose of increasing or decreasing the height and width of the rig. The pressure probes are housed in the holes in the rail with the help of collar sleeves and plastic inserts. They are then held in place with the help of gorilla epoxy (Fig. 4.7).

Figure 4.7 Kiel probe rack

This adjustable rack was then configured according to the dimensions of the vehicle radiator and bolted to the frame with the help of two corner brackets (Fig. 4.8). The rack is bolted behind the radiator to measure the value of the dynamic pressure behind it. This would measure the dynamic pressure of the air that passes through the radiator which can be related to wind speed. 7 out of the 15 available Kiel probes were used to measure the dynamic pressure behind the radiator.

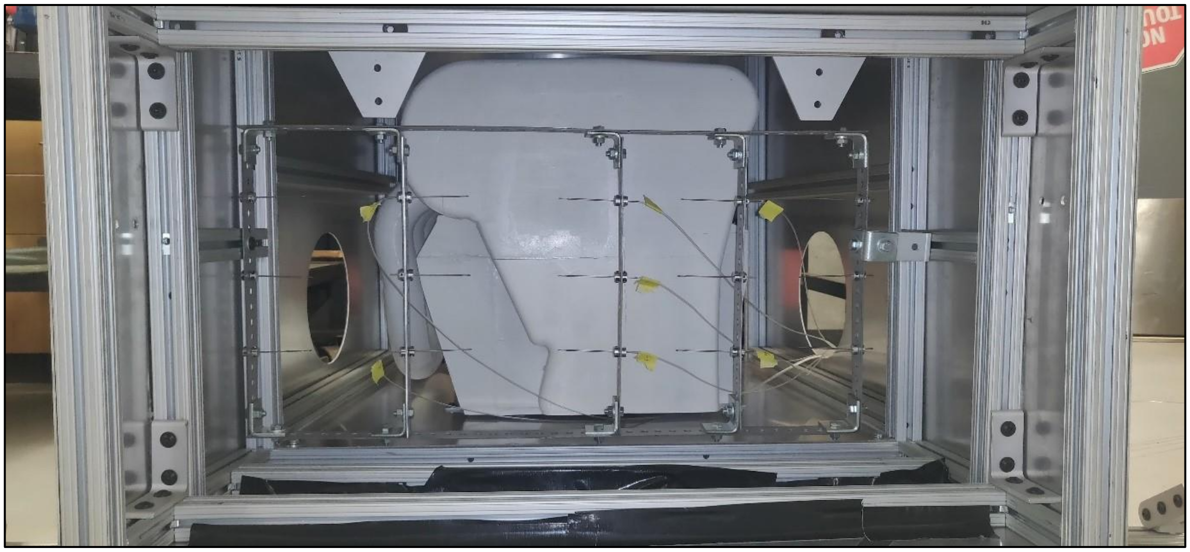

Figure 4.8 Positioning of Kiel probes behind the radiator

The output from the pressure probes was taken into the Digital Sensor Array or DSA for short, also known as the Scanivalve (Fig. 4.9). A reference line was also connected to the Scanivalve for getting a reference value for pressure. This measures the reference dynamic pressure right at the nozzle of the wind tunnel and the software then subtracts the value of dynamic pressure measured at each point where the tubing are inserted to give a value of change in dynamic pressure (ΔQ) which is nothing but a measurement of change in wind speed at that point. The DSA measures change in dynamic pressure and records data for 30seconds at 10Hz when the wind speed in the tunnel stabilizes. The pressure tubing was taped to the ground before being connected to the DSA to prevent it from being blown away when the wind picks up speed.

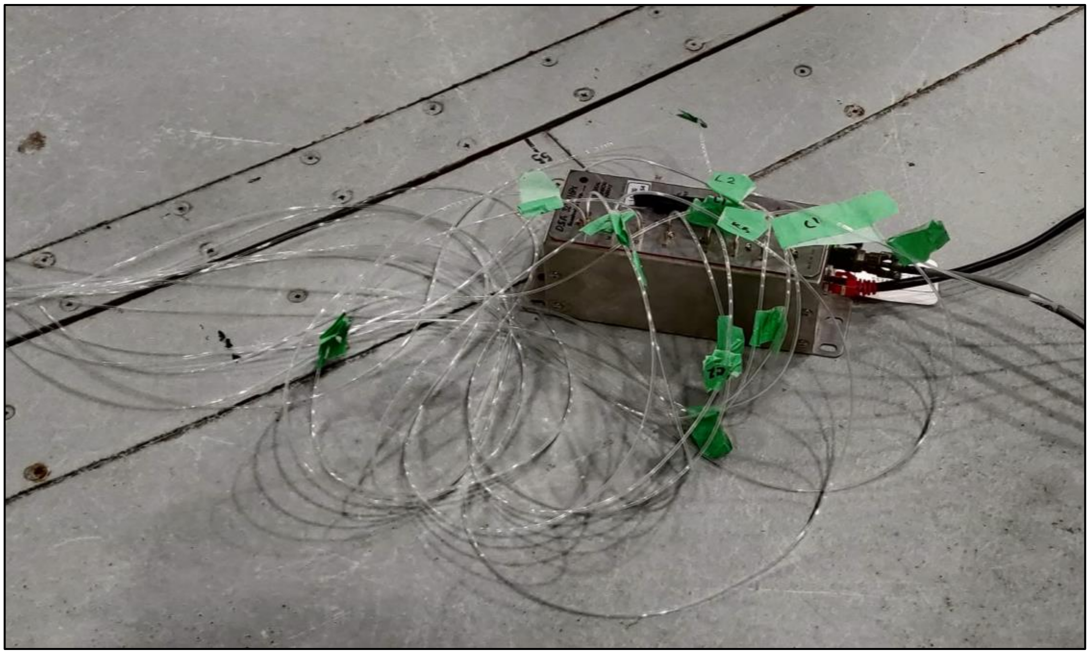

Figure 4.9 Digital sensor array (Scanivalve)

4.1.4.1 Error estimation

For estimating the error associated with the Kiel probes and pressure tubing, the manufacturer's website was consulted, and they are affected only by turbulence, boundary effect, and the time constant. Other possible sources of error include alignment, human, repeatability, and zero balance errors. Kiel probes used in this study have a yaw range of ±52° and a pitch range of +47° and -40°. Since the airflow in the wind tunnel has very low turbulence (~0.1%), and the probes are aligned perfectly with the airflow direction, turbulence error is negligible. The probe is affected by the boundary effect only when there is a steep pressure gradient. The total pressure gradient between the nozzle dynamic pressure and the dynamic pressure measured at the testbench does not vary steeply in this test, and hence this source of error is inconsequential. The time constant comes into effect when the distance between the measuring probe and the data acquisition unit is within 20 ft and the diameter of the hose used is 1/8 of an inch. In this case, the time constant is 2.4*t*, where *t* is the time taken for the probe to reach equilibrium in terms of the measured pressure value. This was determined to be approximately 15 seconds. The hose used in this setup was 1/16 of an inch, and the DSA starts measuring data only after 30 seconds of constant wind speed. So, the time constant has a negligible effect.

Alignment error and human error go hand in hand because the latter causes the former. This source of error can also creep into the measured values as the pressure tubing in front of the radiator might get slightly misaligned due to the airflow. The errors from these two sources can lead to some discrepancies between the measured and actual dynamic pressure values. But this is within the acceptable error range, as the tubing is almost flush with the front surface of the radiator, so the effect of misalignment is almost undetectable.

The main concern for this study is repeatability, as numerous cases have been tested and compared. The repeatability of test results ensures consistency of test conditions. Identical runs were performed during testing under the same conditions to confirm repeatability and the results are depicted in Fig. 5.1 and 5.3. It was seen that these results were within ±3 Pa of each other. These values are averaged over a sample set of over 11,000 measured values and checked for repeatability. Hence, the dynamic pressure measurements in this study are considered repeatable.

The zero-balance error is a term that manufacturers usually include in their specifications. It exists when the probe shows a pressure reading in a no-load condition. These probes were calibrated beforehand to avoid this error.

For estimating the uncertainty associated with the digital sensor array, the following general equations were used (Taylor, 1939):

$$C_1 = \text{Reference value} \tag{4.1}$$

$$C_2 = \text{Accuracy}^1 \times C_1 = 0.0005 \times C_1 \tag{4.2}$$

$$C_3 = \frac{C_2}{C_1} \tag{4.3}$$

$$C_4 = \frac{std.\ dev.}{avg.} \tag{4.4}$$

$$C_5 = \sqrt{C_3^2 + C_4^2} \tag{4.5}$$

Table 4.1 Uncertainty associated with the digital sensor array

Device	**Quantity measured**	**Reference value (C_1)**	**Absolute uncertainty (C_2)**	**Relative uncertainty (C_3)**	**Relative precision error (C_4)**	**Total uncertainty (C_5)**
DSA	ΔQ (AGS open)	238 Pa	0.119	0.0005	0.0054	0.005423
DSA	ΔQ (partially open)	240 Pa	0.12	0.0005	0.0023	0.002353

From Table 4.1, the estimated total uncertainty in the measurement is less 1%, which is within the acceptable range.

4.1.5 Test vehicle setup for validation

A Ford Fusion 2016 Model was rented and instrumented (Fig. 4.10). The underbody panels of the car were removed followed by the AGS. It was observed that the condenser

---

[1] ±0.05% full-scale long-term accuracy obtained from Scanivalve Inc.

is installed in front of the radiator. Since it would be facing the brunt of the wind force when the AGS vanes open, it was decided that the pressure probes would be inserted into the condenser itself instead of the radiator as proposed earlier. A pressure probe grid of 3×5, i.e. 15 probes, was set up (Fig. 4.11).

Figure 4.10 Test vehicle

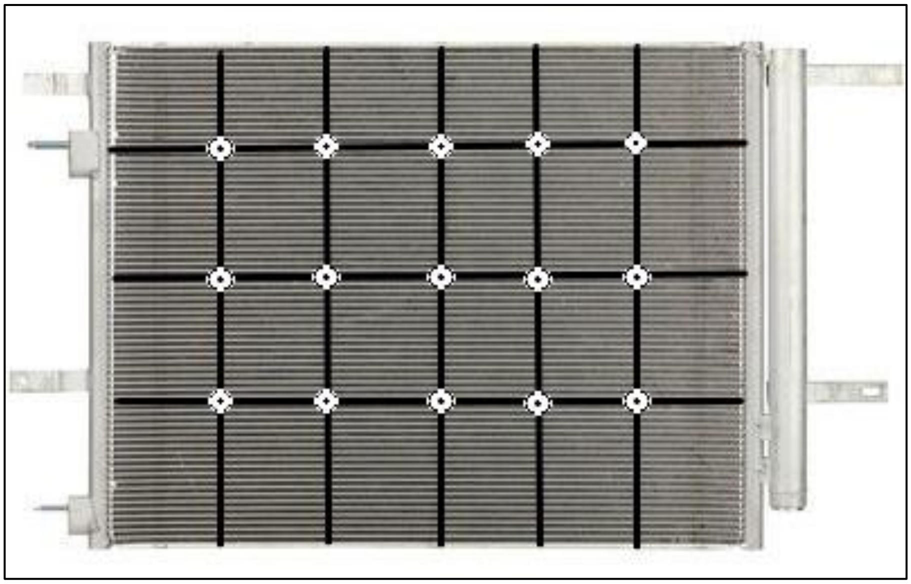

Figure 4.11 Pressure tube positioning in the condenser

After inserting the pressure tubing, the condenser was put back into the vehicle and every component was installed in its original place. Then the car was moved into the tunnel, and the tubing was routed through the underside of the vehicle, into and out of the left wheel well of the car, from where the output was taken and connected to the Scanivalve (Fig. 4.12).

Figure 4.12 Test vehicle in CWT at ACE

4.1.5.1 Test procedure for vehicle

The vehicle was tested for 3 different conditions, i.e. *AGS closed*, *AGS partially open*, and *AGS open*, at the same 15 speeds the Testbench was tested at. The AGS vanes on the vehicle are controlled by the onboard ECU, so it was not possible to operate it manually. The vanes close when the AC is switched off or when the vehicle is cruising at speeds of more than 70kmph. They stay partially open when the vehicle is turned off, so that air from the surroundings can enter the engine bay and cool the parts faster than if the vanes were completed. The AGS vanes open completely when the radiator needs to be cooled or when the user places an air conditioning demand on the cooling system of the vehicle. For this test, the vehicle was stationed on the dyno rollers but not driven, because the AGS vanes can be operated without actually driving the vehicle and just by controlling the onboard AC controls. For keeping the vanes closed, the car was kept idling in park mode with the air conditioner off. For keeping the AGS partially open, the car was switched off and the vanes automatically came to the desired position, as the vanes need to be open slightly when the car is switched off to enable cooldown of the radiator and other engine bay components. For the final case, keeping the vanes open, the AC was turned on, which brings in more air into the condenser that allows for better heat exchange which leads to better cooling. Three sets of data were recorded, at 10Hz for 30seconds, which gives about 5300 values for every case.

Pressure data from the pressure tubing in the test vehicle is averaged out over the 15 data points and a mean value of change in dynamic pressure is obtained. This is plotted along with the averaged value of 8 data points from the testbench, where the pressure tubing is inserted into the radiator from behind, on a graph of change in dynamic pressure (ΔQ) (Pa) vs wind speed (kmph).

4.1.6 Test matrix

The following is the test matrix according to which the experimental testing was carried out on the test vehicle (Table 4.2) and the testbench (Table 4.3 and 4.4):

Table 4.2 Test matrix for validation using test vehicle

Test No.	Vehicle AGS Configuration	Wind Speeds Tested (kmph)
1	Vehicle AGS closed (vehicle idling without A/C)	12, 14.4, 21.6, 28.8, 36, 43.2, 50.4, 57.6, 64.8, 72, 79.2, 86.4, 93.6, 100.8 and 108
2	Vehicle AGS partially open (vehicle turned off)	
3	Vehicle AGS open (Vehicle idling with A/C running)	

Table 4.3 Test matrix for testbench

Test No.	**Testbench Configuration**	**Wind Speeds Tested (kmph)**
1	Testbench sealed AGS closed	12 14.4 21.6 28.8 36 43.2 50.4 57.6 64.8 72 79.2 86.4 93.6 100.8 108
2	Testbench sealed AGS partially open	
3	Testbench sealed AGS open	
	Seals removed	
4	Testbench unsealed AGS open	
5	Testbench unsealed AGS partially open	
6	Testbench unsealed AGS closed	
	AGS removed	
7	Radiator completely sealed	

Table 4.4 Test matrix for leakage characterization

Test No.	**Seal configuration**	**Wind Speeds tested (kmph)**
1	Top unsealed	20 40 60 80 100
2	Bottom unsealed	
3	Top and bottom unsealed	
4	Only sides unsealed	
5	Fully unsealed	

4.1.7 AGS testing procedure

Based upon the knowledge and experience gained from conducting the aforementioned experimental testing, a testing procedure was developed to guide AGS testing in a wind tunnel. This procedure dictates the order in which the different experimental configurations are to be set up and tested to ensure consistency and accuracy. The procedure for testing an AGS in the wind tunnel using the aforementioned testbench is described below:

4.1.7.1 Setting up pressure probes

1. A pressure probe rack is setup with the probes installed inside the holes in the rack (as shown in Fig. 4.7). Based on this testing experience, 24 pressure probes are suggested for the rack to get the best resolution.
2. Pressure tubing are joined and sealed to the connecting end of the probes, routed from the side of the testbench, and inserted in their respective positions in the Scanivalve.

3. Pressure tubing is inserted into the pressure plate from the back such that their front end lies flush with the plate’s front face (as shown in Fig. 3.11). Based on this testing experience, 24 pressure tubing are suggested for the front face to get a good resolution.
4. This pressure plate is then installed in the testbench.
5. The pressure tubing from the plate is routed through the side of the testbench, same as before, and inserted in their respective positions in the Scanivalve.
6. The sides of the pressure plate are then sealed to make it airtight by using a material suitable for sealing (cardboard, plastic, tape, etc.) (Fig. 3.11).

4.1.7.2 Setting up the AGS

1. The AGS to be tested is then installed in the testbench, secured with the help of bolts at the top and bottom as shown in Fig. 3.12.
2. The open gaps around the AGS can be sealed to make it airtight in the same way as before (Fig, 3.12) or unsealed, as is dictated by the test conditions.
3. The front panel of the testbench is installed. The side panels are swiveled to flip them open and are joined with the supports from behind. (Fig. 3.13).

4.1.7.3 Wind tunnel testing procedure

1. Secure the testbench in the wind tunnel and ensure it is centrally placed in the same lateral position as if it were a vehicle. Use magnetic stops and/or torqueing chains to secure the testbench in place.
2. Once secured, begin testing the AGS for full open (Fig. 4.2), partially open (Fig. 4.3), and closed (Fig. 4.4) conditions in any suitable order, at speeds of 20, 40, 60,

80, 100, and 120 kmph. The speeds simulate city, country, highway driving, and stopping conditions.

3. Testing can be repeated to ensure repeatability, stability, and consistency.

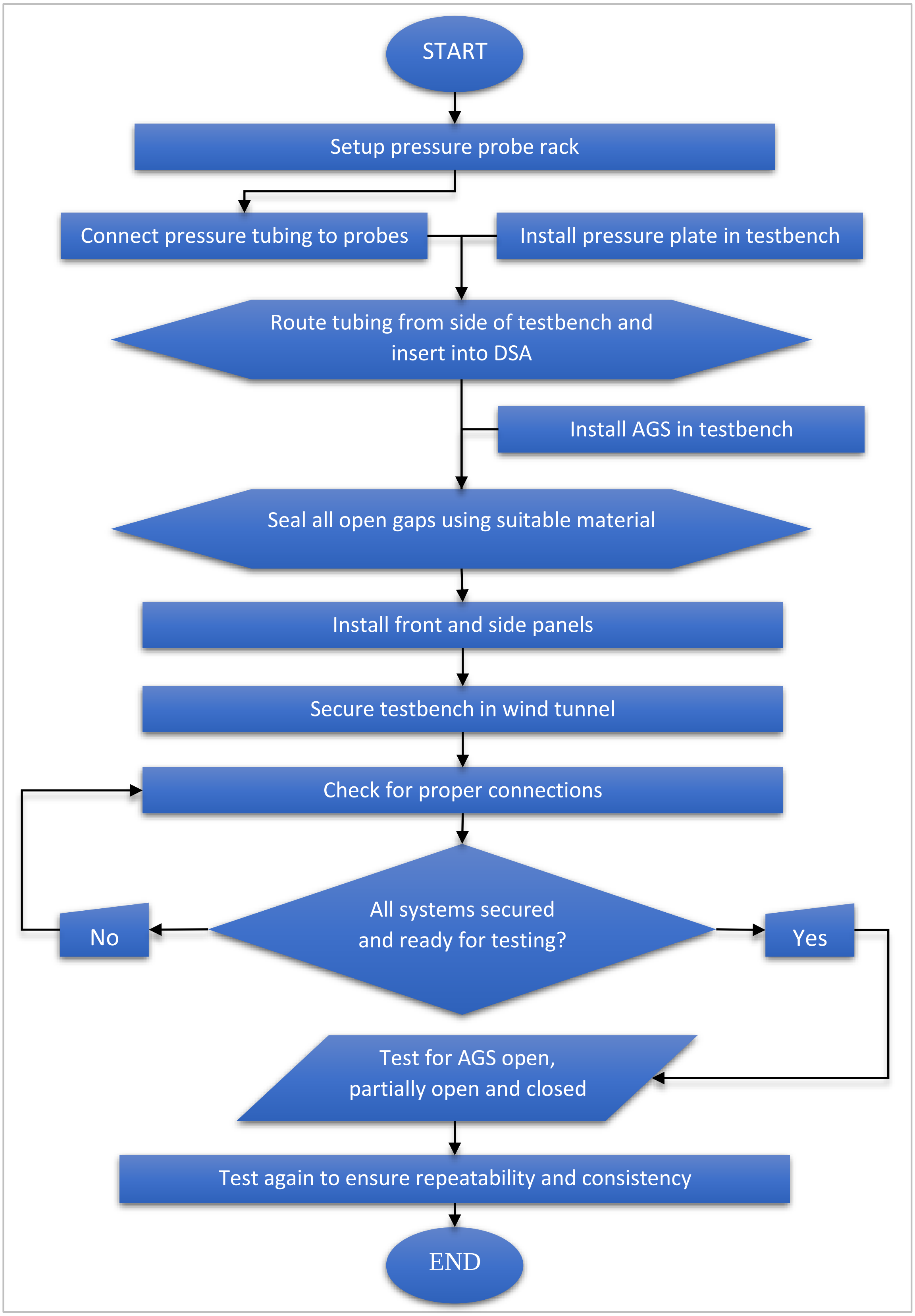

Figure 4.13 AGS testing procedure

4.2 Numerical Experiments

4.2.1 Numerical background

A numerical study was performed on the pressure plates to verify their design in Section 3.4.1 which was based on the theoretical correlations. A commercially accessible Computational Fluid Dynamics (CFD) software called ANSYS Fluent was utilized for this purpose. The three governing equations of continuity, momentum, and energy, which are the basis for CFD analysis are as shown below (refer Nomenclature for symbol definitions):

Continuity equation

$$\nabla \vec{v} = 0 \tag{4.6}$$

Momentum conservation equation

$$\frac{\partial \vec{v}}{\partial t} + (\vec{v}\nabla)\vec{v} = -\frac{\nabla p}{\rho} + \frac{\mu}{\rho}\nabla^2 \vec{v} \tag{4.7}$$

Energy conservation equation

$$\rho c_p \left(\frac{\partial E}{\partial t} + v_x \frac{\partial E}{\partial x} + v_y \frac{\partial E}{\partial y} + v_z \frac{\partial E}{\partial z}\right) = k_T \left(\frac{\partial^2 E}{\partial x^2} + \frac{\partial^2 E}{\partial y^2} + \frac{\partial^2 E}{\partial z^2}\right) \tag{4.8}$$

Upon analyzing all the models available in ANSYS for solving fluid dynamics problems, the Shear Stress Transport (SST) k-ω model was selected for this study. The SST version of this model was preferred over the standard model, which is suggested by ANSYS as a default because this model has been designed to avoid freestream sensitivity as opposed to its counterpart (Wilcox 1993). It combines the standard k-ω model and the high Reynolds number form of the k-ε model (Menter 1994). The high Reynolds number form of k-ε is used in the external region of the boundary layer whereas the standard k-ω model is used in the inner area of the boundary layer. This SST k-ω model has also been widely used for aerodynamic numerical simulations worldwide because of its low error rate (0.8%) when equated to other turbulence models in forecasting the value of the drag coefficient (Pointer 2004). The transport equations for the SST k-ω model are as follows:

$$\frac{\partial}{\partial t}(\rho k) + \frac{\partial}{\partial x_i}(\rho k u_i) = \frac{\partial}{\partial x_j}\left(\Gamma_k \frac{\partial k}{\partial x_j}\right) + G_k - Y_k + S_k \tag{4.9}$$

$$\frac{\partial}{\partial t}(\rho \omega) + \frac{\partial}{\partial x_j}(\rho \omega u_j) = \frac{\partial}{\partial x_j}\left(\Gamma_\omega \frac{\partial \omega}{\partial x_j}\right) + G_\omega - Y_\omega + D_\omega + S_k \tag{4.10}$$

Where G_k is the turbulence kinetic energy production, G_ω is the ω generation, τ_k and τ_ω are the diffusivities of k and ω effectively, Y_k and Y_ω are used to indicate the dissipation due to turbulence of k and ω, D_ω is the cross-diffusion and lastly, S_k and S_ω are the terms defined by the user. The SST k-ω model has thus been established to be uniform and numerically robust and it has the ability to provide consistent and accurate results.

4.2.2 Fluent setup

4.2.2.1 Mesh setup

The CAD file of the external design of the testbench was uploaded to ANSYS, and this was done without the supporting internal structure, to simplify the mesh design. The space and dimensions inside and outside the testbench were kept the same to avoid any discrepancies. The dimensions of the plate that would fit in the testbench were determined. The enclosure setup was done to keep as much air flowing through the plate within the testbench as possible. Three testbench lengths in front (4065mm) and five testbench lengths at the back (6775mm) of the testbench were used as the enclosure dimensions, while the sides, top, and bottom were kept at a minimum distance of 1mm from the surface (Fig. 4.14). This was done to prevent air from taking the path of least resistance and flowing around the testbench. The projected area of the 3D engine in two dimensions was determined and a solid of the same measurements was designed and put just behind the pressure plate in the testbench at the same distance as in the original testbench to maintain similar conditions of back pressure and blockage. The mesh sizing was kept fairly small to get a precise measurement of pressure at the front and back of the plate. The element size in the enclosure was kept at 150mm, with the maximum size being 300mm. The face sizing on the testbench was set to be 10mm, while the face sizing for the front and back of the pressure plate was set to be 1.5mm (Fig. 4.15). A body of influence was also created around the testbench to get a higher resolution of mesh around the testbench with an element size of 20mm. The total number of elements was 15,578,277 which provides a high level of accuracy in measurement but trades it in with long processing times (Fig. 4.14 - 4.16). The average skewness was at 0.229 which is well below the suggested average skewness number of 0.337. The mesh solver was set to capture curvature and proximity to ensure a good resolution for the mesh.

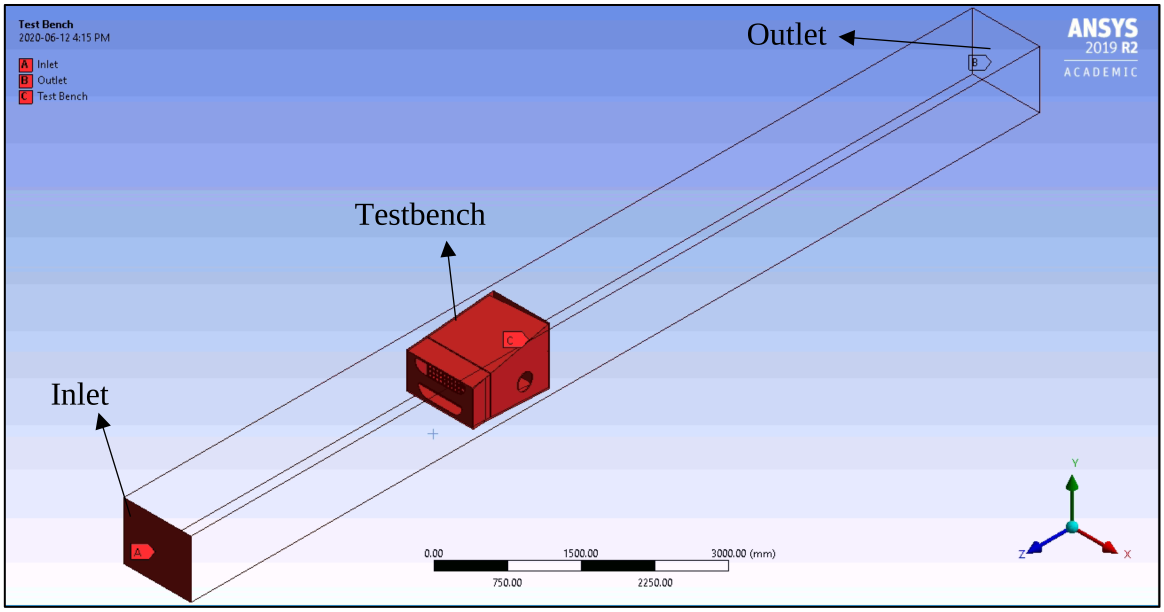

Figure 4.14 Domain description of the enclosure

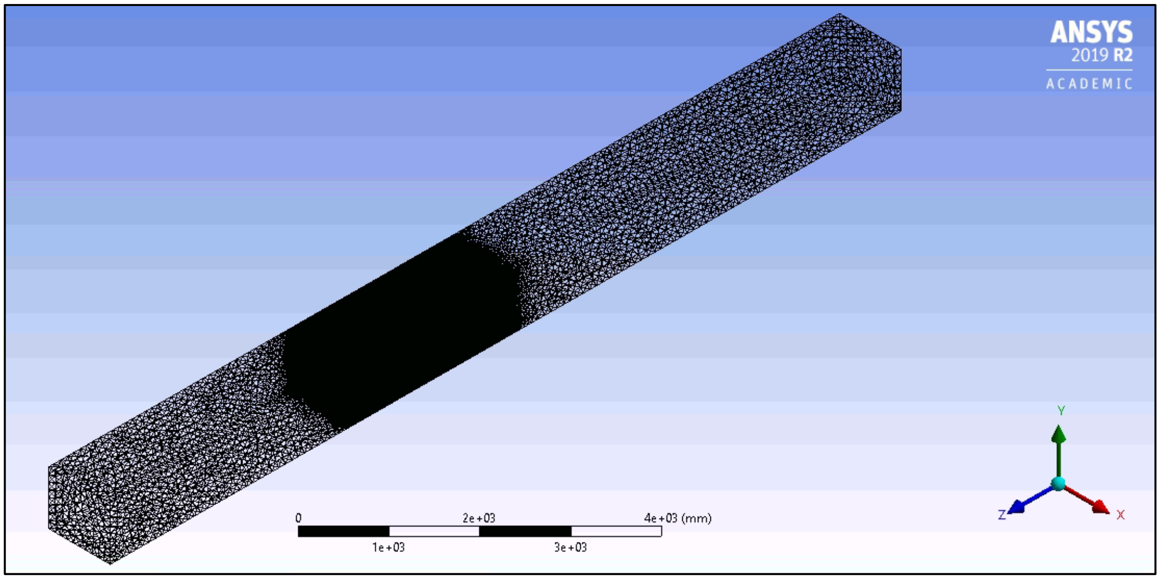

Figure 4.15 Mesh setup for enclosure

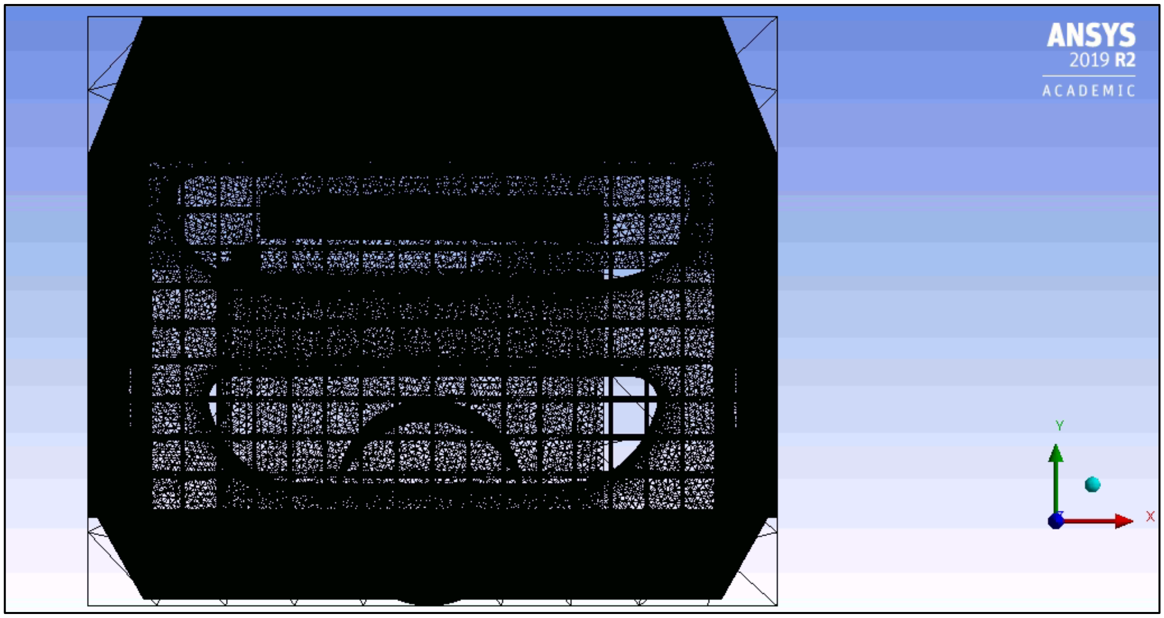

Figure 4.16 Mesh setup for testbench

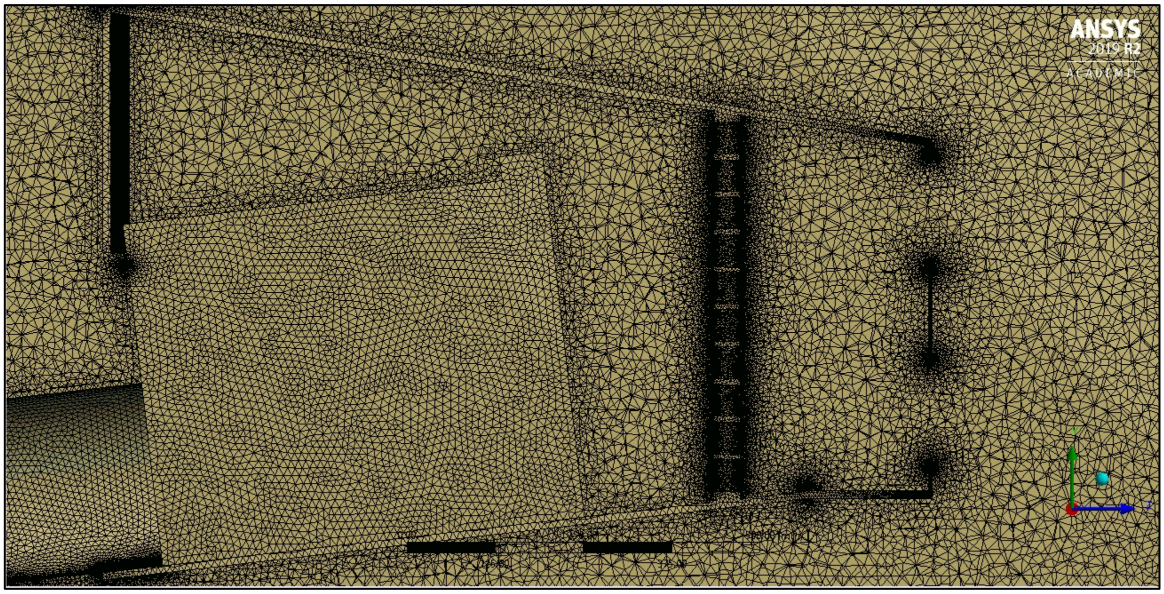

Figure 4.17 Section plane through enclosure

After preliminary simulations, this Fluent setup was further refined to better match the experimental results, and details of these refinements can be found in Appendix G.

4.2.2.2 Mesh independence study

A mesh independence study was performed to make sure the mesh size used for this simulation has enough resolution to provide accurate results. The mesh size used in this study was kept as the base, a coarser mesh and a finer mesh was developed. The coarse mesh consisted of 11.46 million elements, the median mesh had 15.57 million elements as mentioned before, and the fine mesh had 19.78 million mesh elements in the enclosure. Area weighted average (Fig. 4.18) and Facet average (Fig. 4.19) values were compared for all the three mesh configurations for the speeds of 10, 20, and 30m/s, to give us a trendline of the dynamic pressure values over the range of speeds tested in this simulation. The results are shown below.

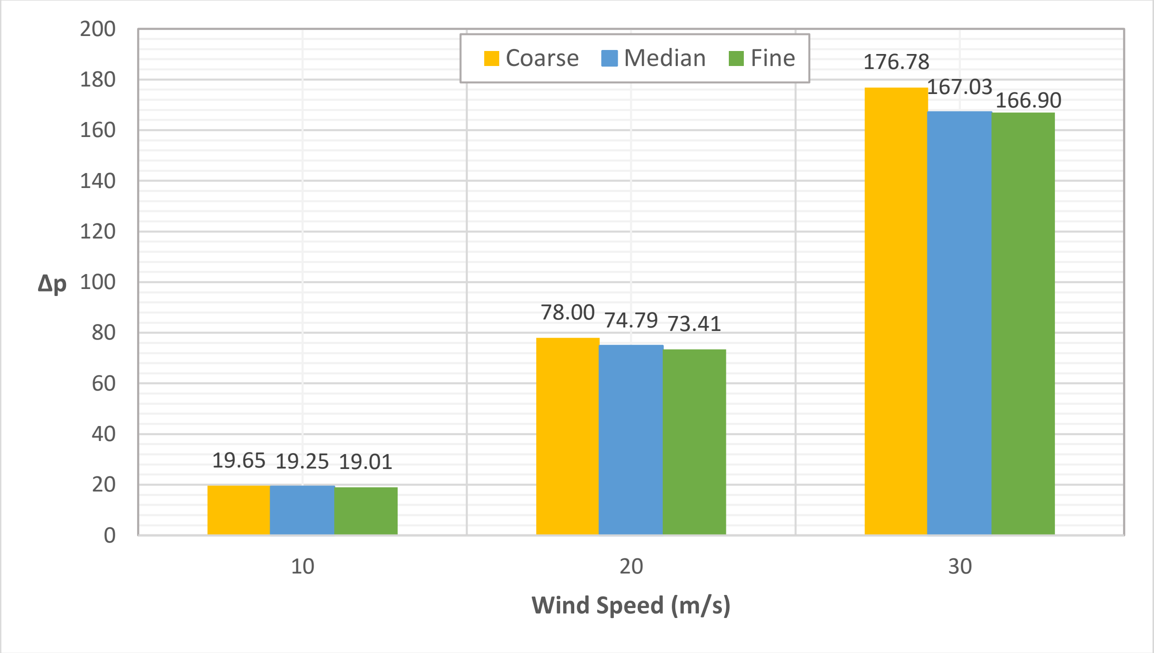

Figure 4.18 Area weighted average comparison

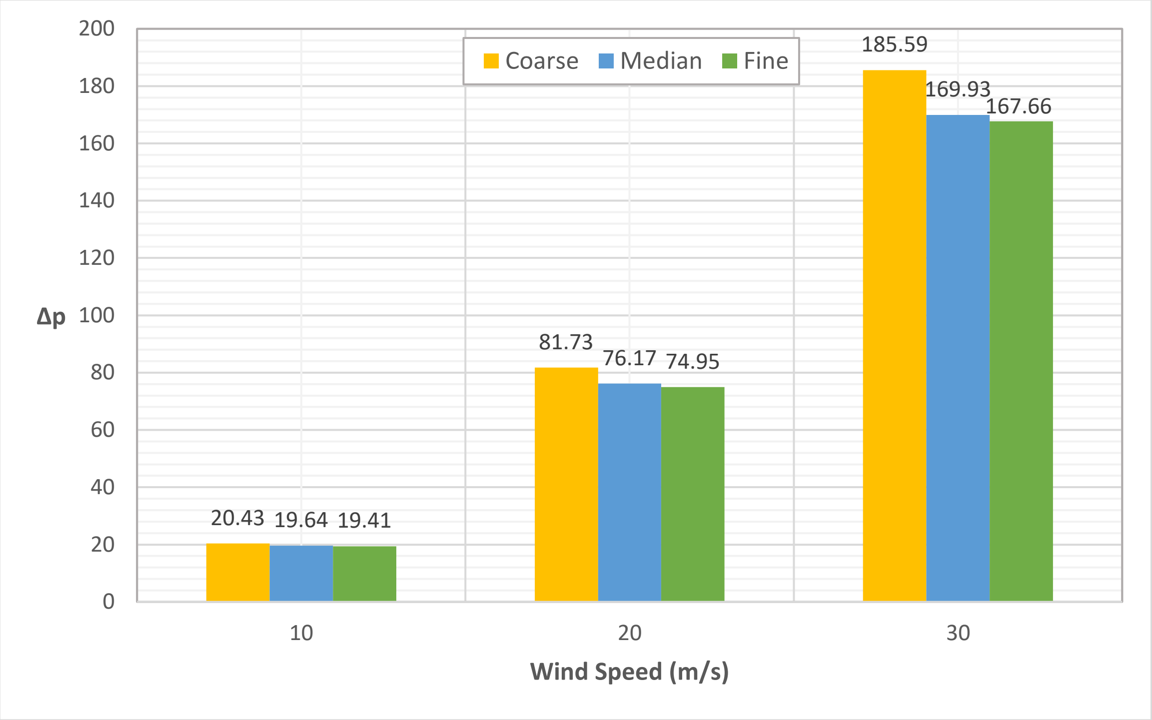

Figure 4.19 Facet average comparison

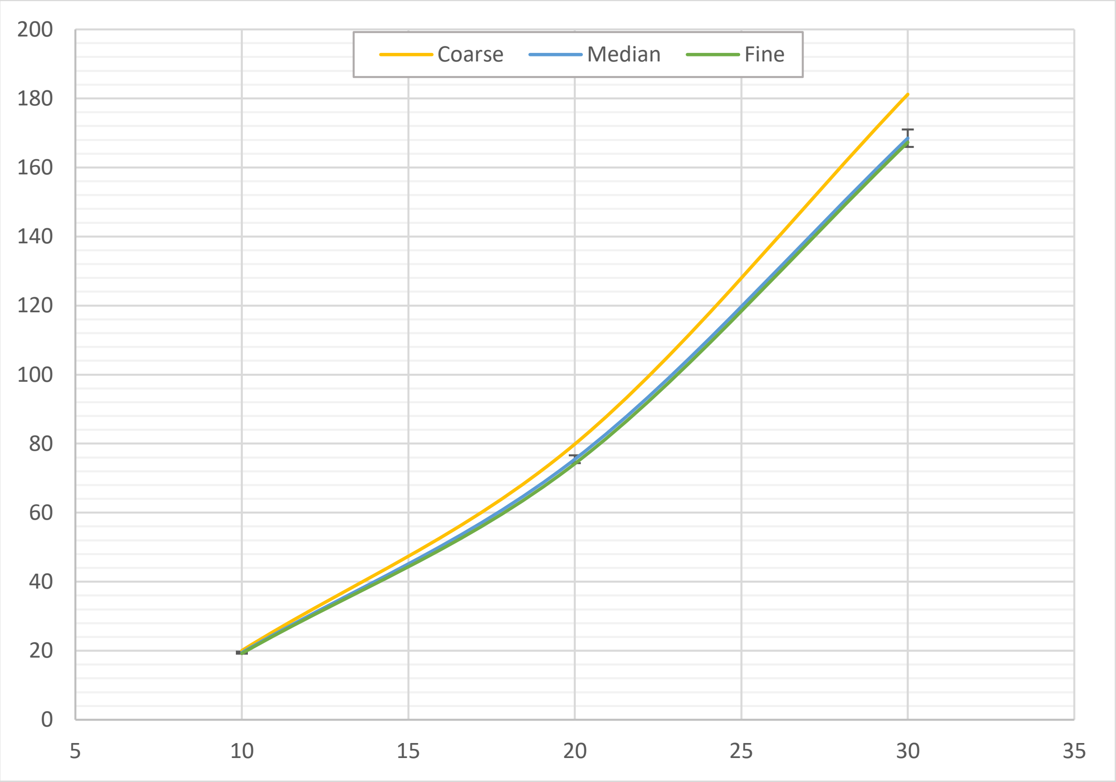

Figure 4.20 Overall average comparison

As seen from the bar chart of the area weighted and facet average comparison, the difference between the base mesh chosen for this study and the finer mesh is minuscule, almost identical, whereas upon reducing the resolution of the mesh, the difference in the dynamic pressure values between the coarse and median mesh is more noticeable. In Fig. 4.20, the overall averages of the median and the fine mesh are almost superimposable. The vertical error bars in this figure denote a maximum error percentage of ±1.5%, and the values of the median and the fine mesh lie within this range. Therefore, to save computational costs and time, the median mesh was used for the rest of the simulations.

4.2.2.3 Boundary conditions

Different speeds were set at the inlet of the enclosure as was the case in the experimental testing. The temperature was kept at 23^{o}C, the same as in the experimental setup in the tunnel. For the air density, 1.17 was used as this is the density of air in the wind tunnel. The turbulent intensity (%) and turbulent viscosity ratio at the inlet of the enclosure was kept at 0.1 and 1 respectively, as these values were obtained from turbulence measurements that were performed in the wind tunnel at an earlier time. A no-slip condition was set at the 4 walls of the enclosure. The turbulence intensity at the outlet was limited to 5% (ANSYS, 2013, 2017). The convergence criteria for the residuals of all the simulation variables, namely, continuity, x, y, and z velocities, turbulence kinetic energy (k), specific dissipation rate (ω), and the energy equations were kept at 10^{-4}.

4.2.2.4 Solver setup

As mentioned earlier, the SST k-ω equation was used for this simulation because of its robustness and acceptability in literature. Since the maximum skewness for the mesh was 0.999, the COUPLE scheme (see Appendix C) was used instead of the SIMPLE scheme, as suggested by ANSYS. The Under Relaxation factors were reduced from the default values to 0.2, 0.5, 0.5, and 0.5 for Pressure (P), Momentum (p), Turbulence Kinetic Energy (k), and Specific Dissipation Rate (ω) respectively, to get uniform results and improve the stability of the solution as recommended by ANSYS. The pressure was calculated using the standard solver as was the default value, while momentum, turbulence kinetic energy, and specific dissipation rate were calculated using first-order upwind, as this study focuses on the pressure differences on the pressure plate surface, and the mesh is of sufficiently high resolution to give accurate results while using the first-order scheme.

4.2.2.5 Area weighted average

Area weighted average (Mohanta, 2019; Saheby, 2019; Bonser, 2020) is calculated as follows:

$$\frac{1}{A}\int \aleph dA = \frac{1}{A}\sum_{i=1}^{n} \aleph_i |A_i| \tag{4.11}$$

which is nothing but the summation of the product of the selected field ($\aleph_i$) and facet area (A_i) divided by the total surface area. This function was used to get the dynamic pressure value over 1000 iterations for the front and back surface of the pressure plate.

4.2.2.6 Facet average

The facet average (Jiang, 2015; Yu, 2011; Krayenhoff, 2007) is computed as follows:

$$\frac{1}{n}\sum_{i=1}^{n} \aleph_i \tag{4.12}$$

which is the summation of the facet values of the selected field ($\aleph_i$) divided by the total number of facets (n). The facet average for dynamic pressure at the front and back surface of the pressure plate was calculated for 1000 iterations in this study.

4.2.2.7 Vertex average

This function calculates the specified field variable as follows:

$$\frac{\sum_{i=1}^{n} \aleph_i}{n} \tag{4.13}$$

which is calculated by dividing the sum of the vertex values of the variable in question ($\aleph i$) by the total number of vertices (n). This function is used to calculate the value of dynamic pressure for the final simulations. This was done to ensure that there is a similarity in the way dynamic pressure is measured between the experiments and the numerical study.

Chapter 5 Results and Discussion

Both experimental and numerical results will be discussed in this chapter. The experimental results will be discussed first, followed by the numerical results. Lastly, the testing procedure will be presented.

5.1 Wind Tunnel Results

5.1.1 AGS open

The AGS vanes are kept completely open in this case and change in dynamic pressure is measured for the 15 aforementioned wind speeds.

Fig. 5.1 compares the change in dynamic pressure (ΔQ) behind the AGS versus the wind speed for four cases: the test vehicle, sealed testbench, and unsealed testbench for two runs to check repeatability (described in detail in Section 4.1.3 and 4.1.5). The results shown in Fig. 5.1 follow the expected trend of dynamic pressure being directly proportional to the square of wind speed (Kuthada et. al 2014, 2016).

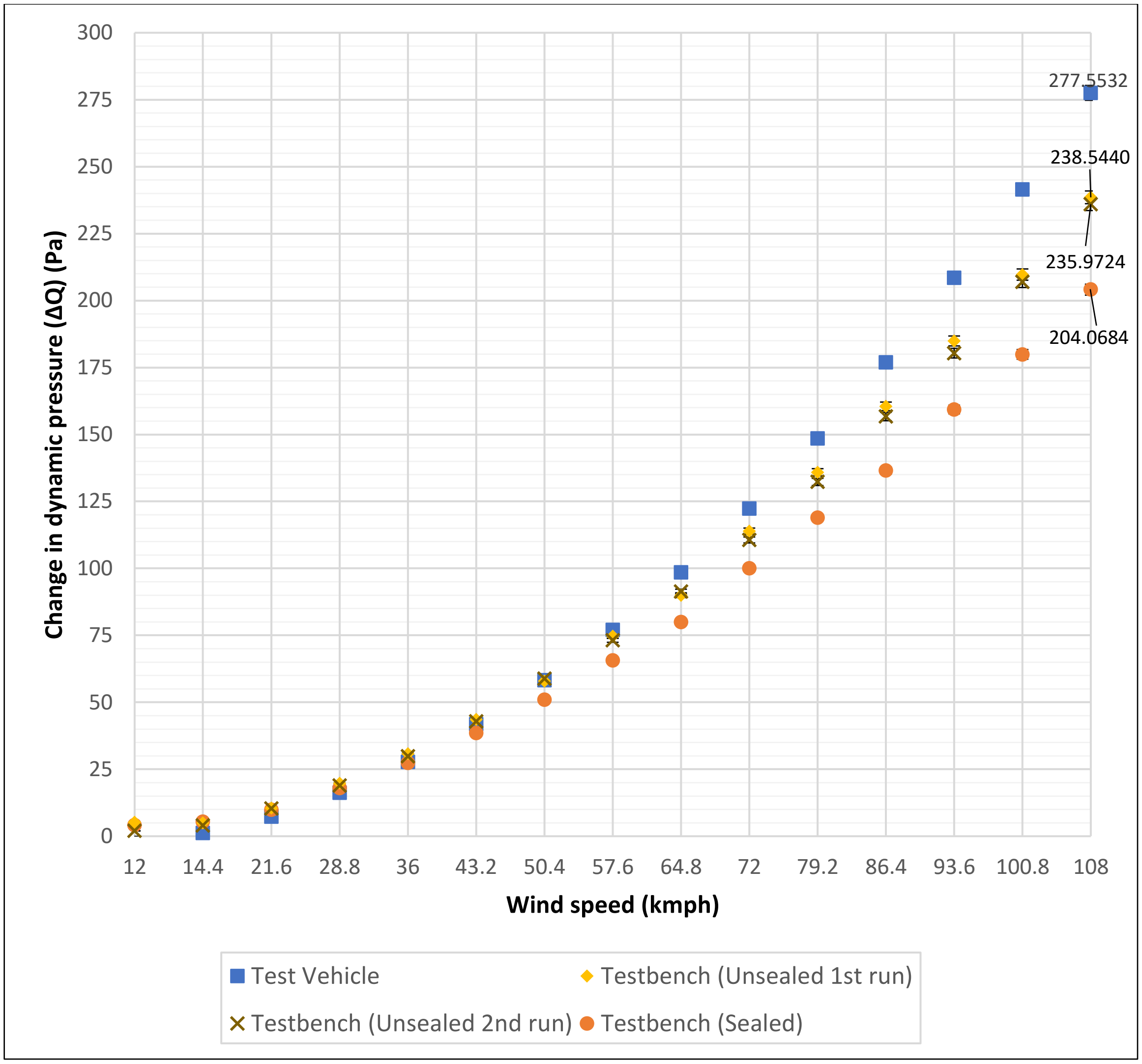

Figure 5.1 Change in dynamic pressure behind the AGS vs wind speed (AGS open)

As is evident from the figure, there is no significant difference in the dynamic pressure up to 50 kmph. Beyond that, the ΔQ for the test vehicle diverged and became consistently higher than the testbench results. The sealed test result shows the lowest value, whereas the test vehicle shows the highest ΔQ value This can be attributed to the fact that the vehicle’s front grille has horizontal cross members which increase the blockage. As the wind speed increases, the blockage effect also increases, and as shown the test vehicle value rises higher than the testbench (see Appendix D for overlay comparison).

The difference in the ΔQ values between the sealed testbench and the test vehicle is 18% at 65 kmph and increases up to 26% at 108 kmph. These significant differences are observed because the airflow through the front grille of the test vehicle encounters more resistance because of the cross members as opposed to the testbench, which has an open top and bottom intake.

The test for the unsealed testbench was conducted twice to check repeatability. As shown in the figure, trendlines are identical, indicating that the results are repeatable and consistent. The ΔQ values for the unsealed testbench test are higher than those of the sealed. This is because sealing the testbench simply directs all the airflow through the designated area of the AGS and prevents leakages. However, the unsealed condition increases the instrument sensitivity as this creates an area of separation between the AGS and the radiator. This leads to an increase in the ΔQ value. The airflow recirculation increases with speed and hence the difference between sealed and unsealed values also increases. Sealing the gaps allows the pressure measurement system to work as intended but increases the gap between the sealed testbench and the test vehicle values.

Thus, from the smaller difference between the unsealed testbench and the test vehicle compared to the sealed testbench, it can be concluded that the unsealed testbench better represents the test vehicle conditions than the sealed testbench.

When the distribution of ΔQ on the front face of the radiator is plotted for three speeds, 36, 72, and 108 kmph as shown in Fig. 5.2. For the legend, the first words indicate a sealed or unsealed case, and the numbers denote the wind speed. The objective of this figure is to illustrate the effect of the seal to buttress the explanation given for Fig. 5.1. The figure shows that the unsealed configuration consistently gives higher ΔQ values. It can be attributed to the fact that the unsealed gaps allow more air leakage as explained earlier and confirms that the differences observed in Fig. 5.1.

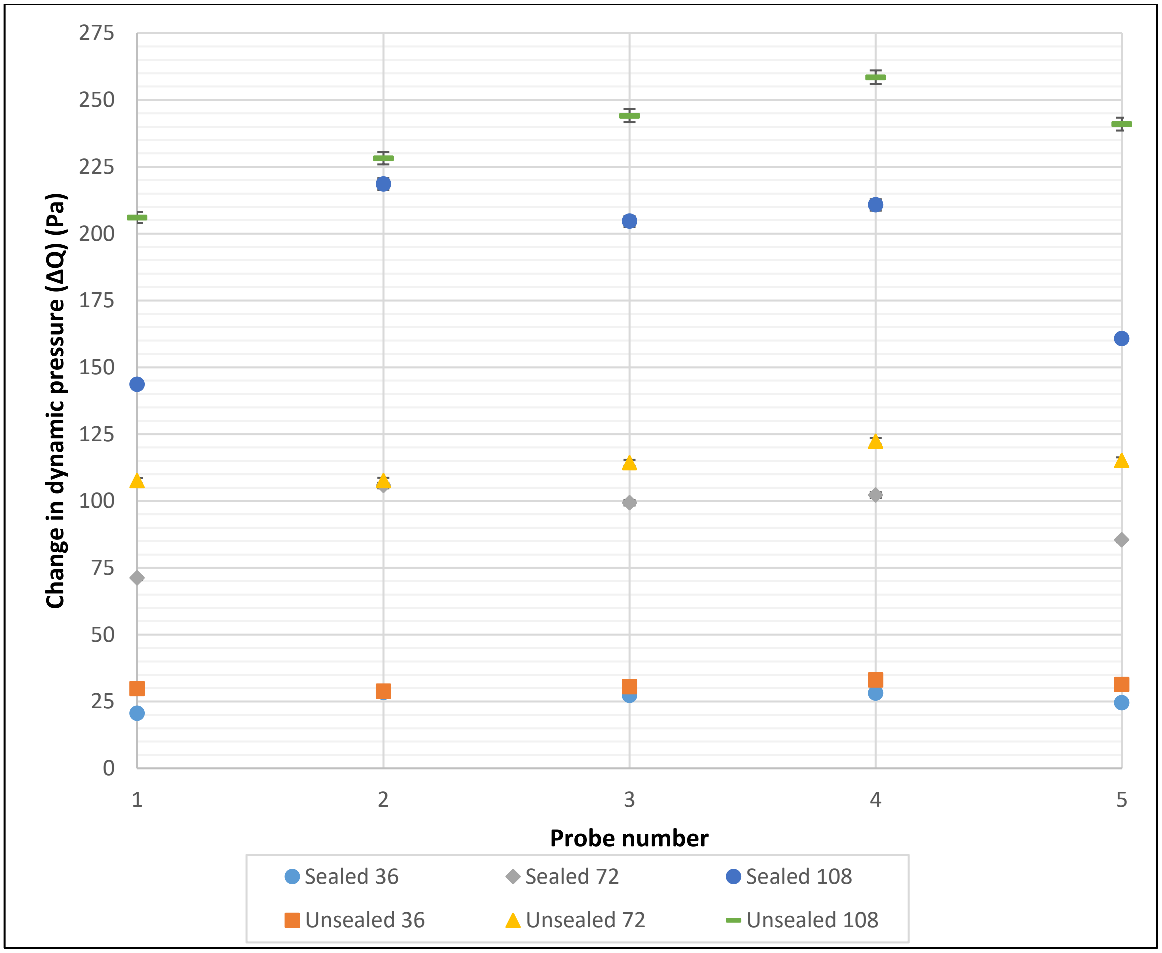

Figure 5.2 Distribution of change in dynamic pressure for sealed and unsealed AGS (open)

5.1.2 AGS partially open

In this case, the AGS vanes on the testbench were turned at an angle so that they are only partially open. Fig. 5.3 shows plots of ΔQ data for the test vehicle and testbench.

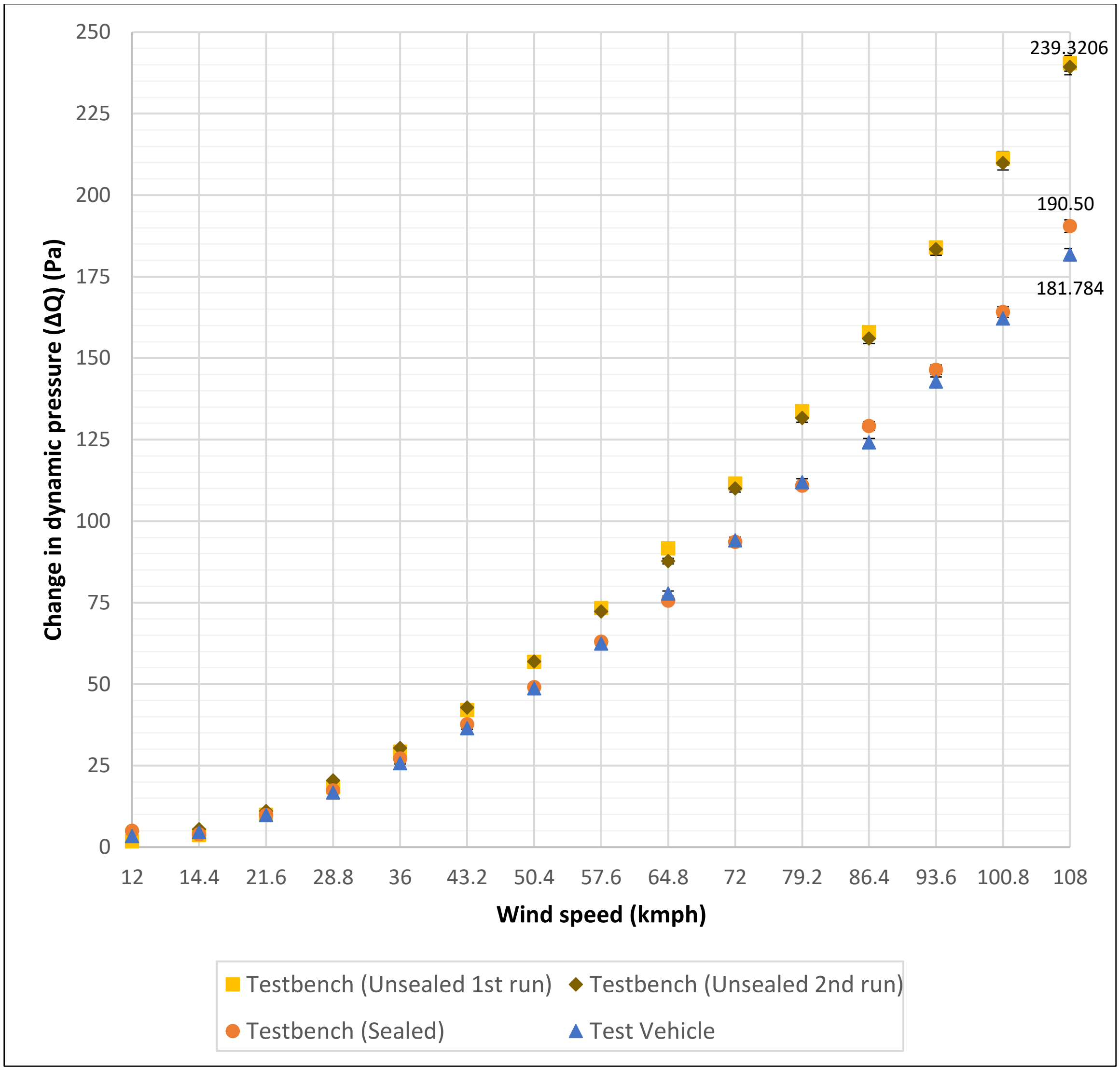

Figure 5.3 Change in dynamic pressure behind the AGS vs wind speed (AGS partially open)

Two distinctly different pairs of trendlines can be observed in Fig. 5.3 for the unsealed testbench and sealed testbench test results. The latter is also nearly identical to the test vehicle trendline, as opposed to the fully open AGS scenario. The sealed testbench and the test vehicle present similar airflow conditions, as they both have a sealed airflow path and have the AGS fins turned at the same angle. Thus, they both produce a nearly identical ΔQ, which is seen in the graph. The unsealed testbench shows a higher trend for both runs when compared to the sealed testbench because of air leak in from the open gaps. This result shows that unlike the 100% open case, the sealed case is a better representation of the real vehicle conditions than the unsealed for the partially open case. It is clear from the above that sealing the open gaps around the AGS is of extremely important for the testbench to produce results that are a good representation of an actual vehicle. The ΔQ values for the partially open case are slightly lower than the fully open case in Fig. 5.1 as expected and the difference between them increases with speed. For instance, the ΔQ values for the sealed testbench is almost the same at 50 kmph for both cases and 11% higher in the fully open case than in the partially open case at a wind speed of 100 kmph.

The distribution of ΔQ on the radiator face is plotted in fashion and for reasons similar to Fig. 5.2 for 36, 72, and 108 kmph to compare the sealed and unsealed testbench as shown in Fig. 5.4. It is observed that the ΔQ values for the unsealed testbench are higher than the sealed values at all three speeds. Similar to the partially open case, there are no significant differences at low speed, but they become much more apparent at higher wind speeds.

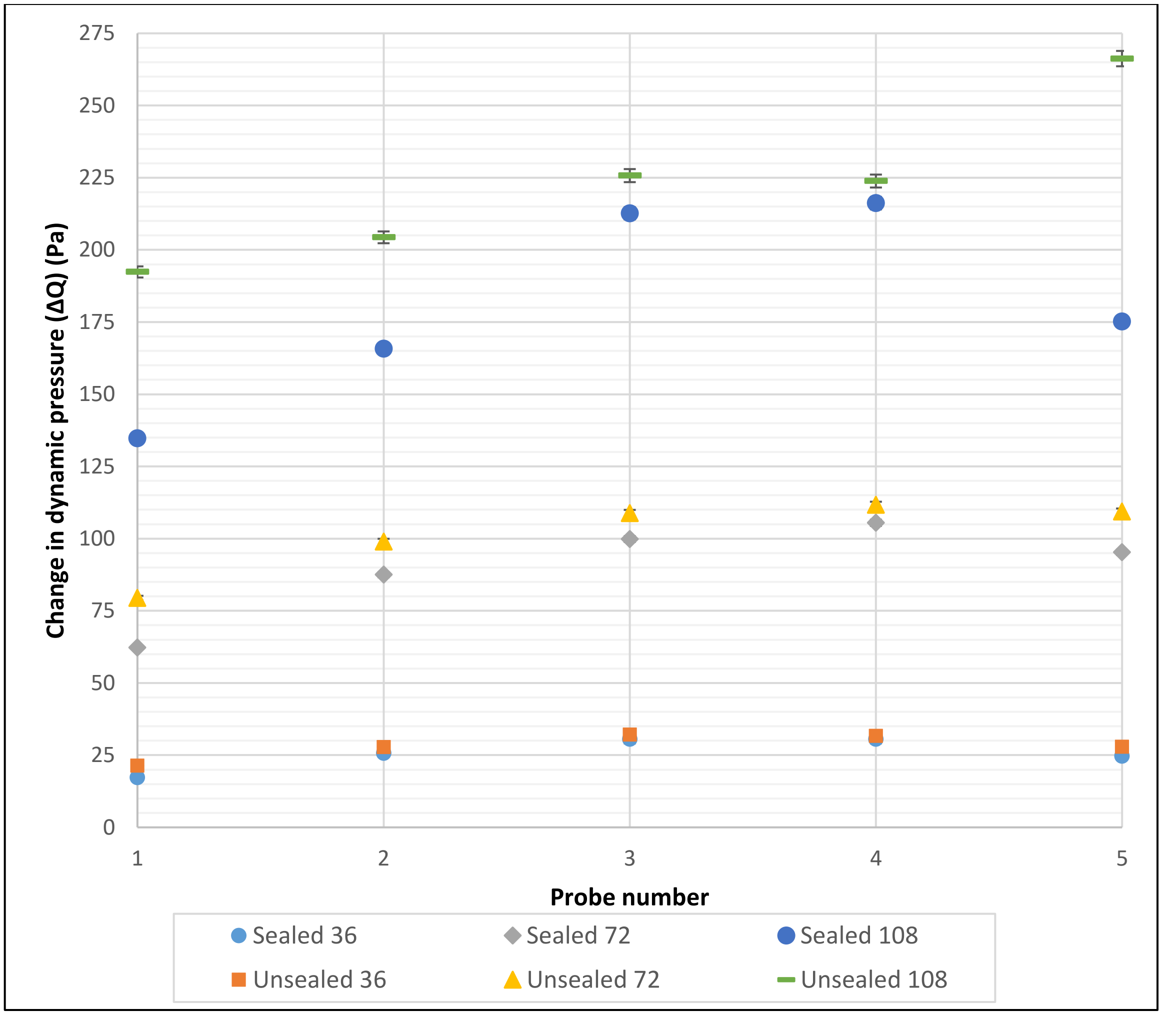

Figure 5.4 Distribution of dynamic pressure change for sealed and unsealed AGS (partially open)

The figure reaffirms that sealing decreases the ΔQ values. Unlike Fig. 5.2, only probe #3 and #4 do not show significant differences in the dynamic pressure values. This is because the probes are directly in front of the AGS fins when they are partially open. This implies that whether the AGS is sealed or unsealed, these probes face an almost identical wind speed, and hence their values are close to each other. Similar to Fig. 5.2, the probes on either end show a wide gap between sealed and unsealed dynamic pressure values, which makes the effect of sealing the gaps further evident.

5.1.3 AGS closed

In this case, the AGS vanes on the testbench are shut completely. Once the ΔQ measurements are made for the sealed testbench, the seals are removed completely to gauge the effect of sealing the open gaps on the measured ΔQ. The averaged values for the test vehicle and the testbench (sealed and unsealed) are then plotted on the graph as shown below (Fig. 5.5):

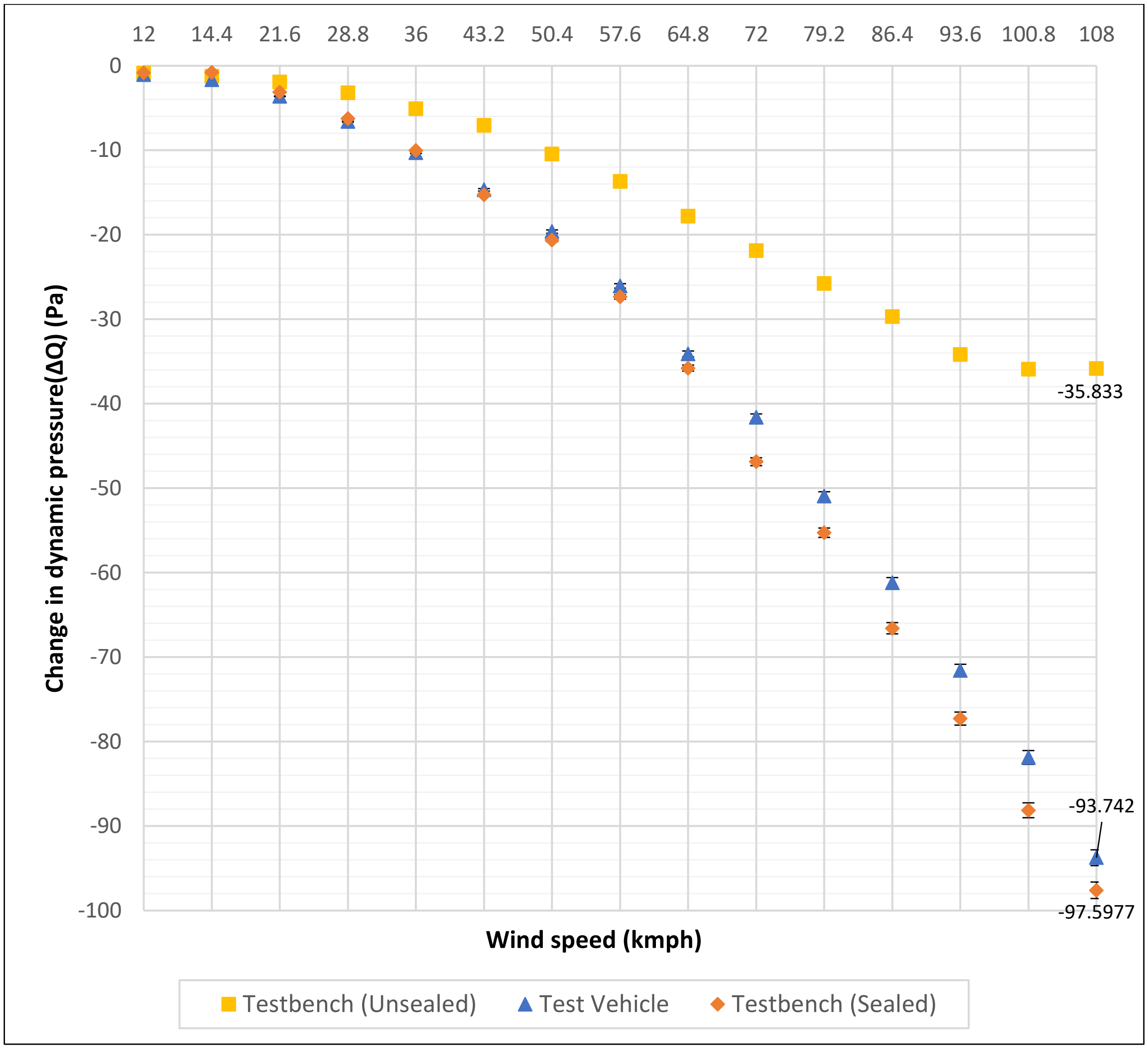

Figure 5.5 Change in dynamic pressure behind the AGS vs wind speed (AGS closed)

We can see from Fig. 5.5, the dynamic pressure values of the sealed testbench and the test vehicle are nearly overlapping whereas the unsealed testbench shows a much higher trend. The trends in the figure above show negative ΔQ values. Since the fins of the AGS are closed, the tubing in both the cases, test vehicle, and the testbench, measures the pressure that is created inside the cavity formed between the AGS and the radiator. This pressure presents itself as a negative cavity pressure with respect to the pressure outside, as they are properly sealed with minimal air leakage. As the wind speed is increased, the magnitude of this negative cavity pressure also increases.

For the unsealed case, some air leaks in from the open gaps with increasing wind speed and we see that negative cavity pressure does not fall as rapidly as the sealed case.

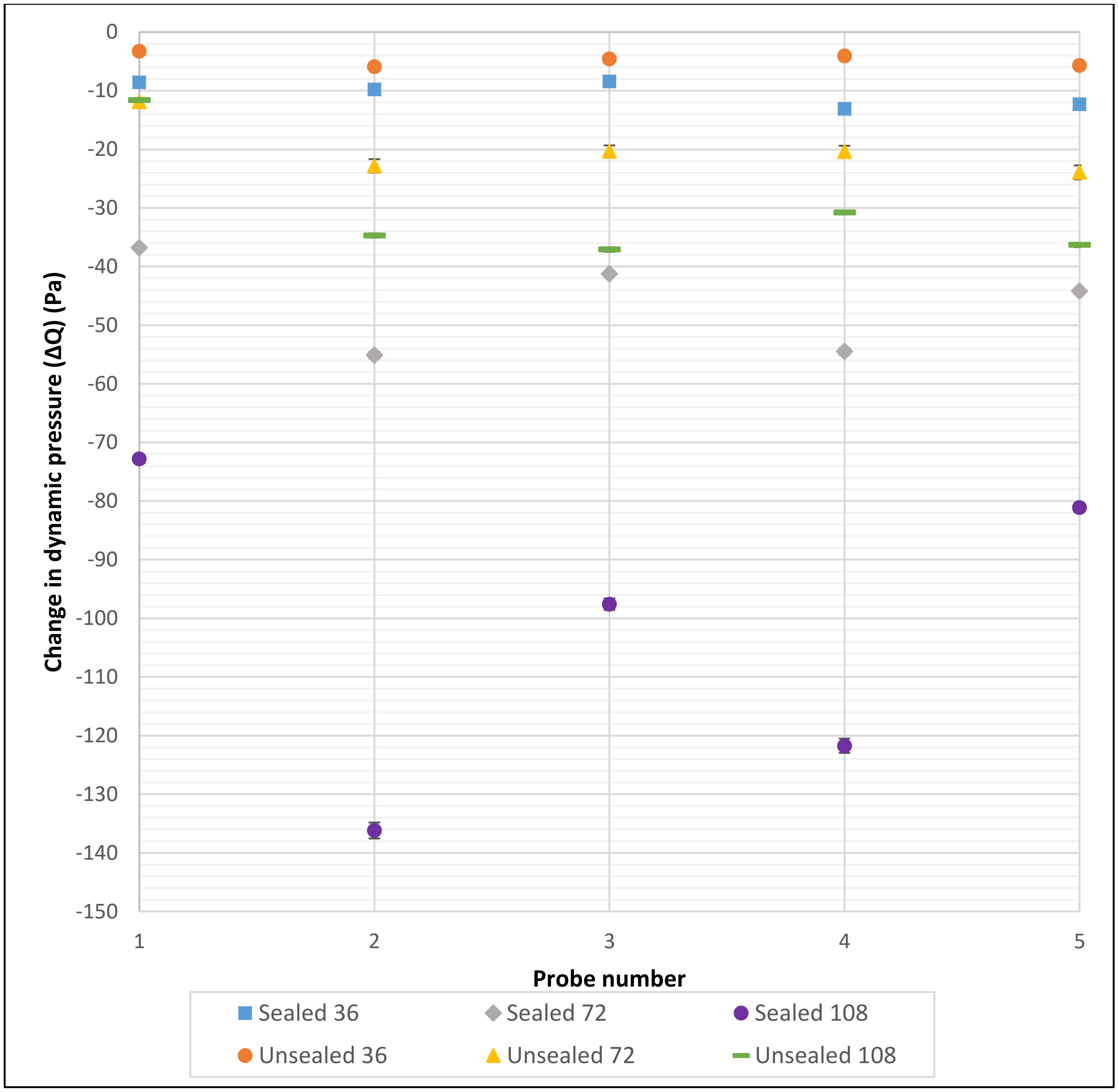

Figure 5.6 Distribution of dynamic pressure change for sealed and unsealed AGS (closed)

The distribution of ΔQ on the radiator face is plotted for the sealed and unsealed testbench at 36, 72, and 108kmph (Fig. 5.6) to gauge the effect of sealing the testbench on the dynamic pressure values when the AGS is closed shut. It is clearly seen that there is a noticeable difference in the sealed and unsealed ΔQ distribution values which increases as the speed is increased. This is because although the AGS vanes are closed shut in both the cases, the presence of open gaps in the unsealed testbench, however, allows air to leak in and hit the front surface of the radiator. This increases the value of the negative cavity pressure as described above and prevents it from dropping down to the sealed testbench level.

This proves the fact that sealing the AGS and making it air-tight produces results that are in close proximation to the test vehicle as opposed to the unsealed condition.

Thus, keeping in mind the three conditions tested earlier (AGS open, partially open, and closed), it can be stated that the testbench performance characteristics at AGS partially open and closed scenarios produce near identical results as an actual vehicle when sealed. However, for the AGS open case, keeping the gaps unsealed produces comparatively better results. The change in dynamic pressure values were further converted into terms of the coefficient of pressure (C_p), and are plotted and shown in Appendix H. Hence, this successfully validates the functionality and effectiveness of the testbench for AGS testing.

5.1.4 Pressure drop across the radiator

Once the AGS testing was complete, the AGS was removed from the testbench, leaving only the radiator in place (as discussed in Section 4.1.3.2). The ΔQ was measured at the front and rear faces of the radiator. The ΔQ values from the 8 probes at the front and 7 at the rear face are averaged to give a single value of ΔQ at each face. From these values, the pressure drop across the radiator is estimated as shown in Fig. 5.7. It also shows the existence of a 3rd-degree polynomial relationship between pressure drop and wind speed in the form:

$$y = 7E - 05x^3 - 0.019x^2 - 0.1452x + 0.0964 \tag{5.1}$$

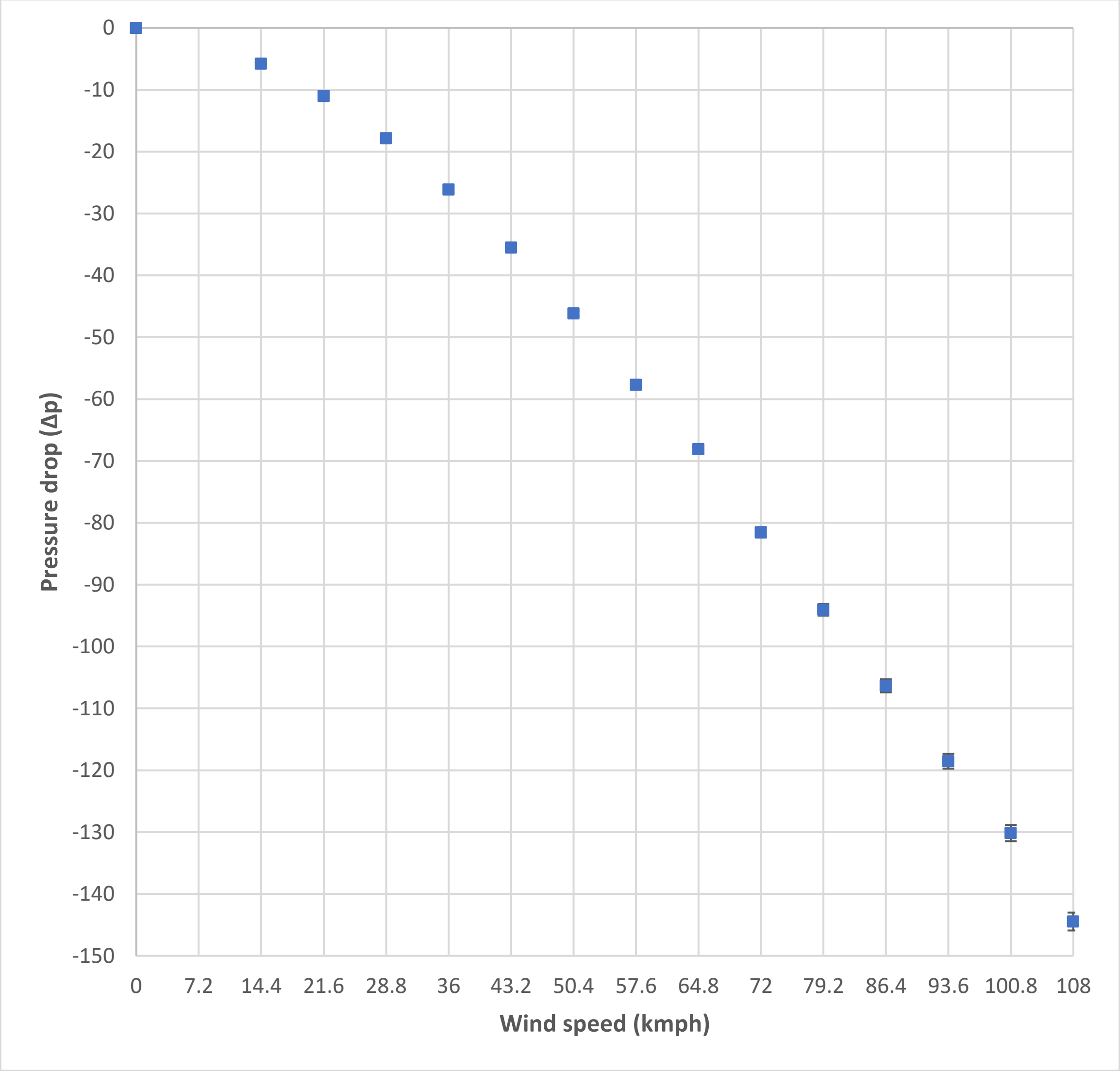

Figure 5.7 Pressure drop (ΔP) across the radiator

This trendline shows that the magnitude of the pressure drop across the radiator increases with the wind speed, due to the fact that dynamic pressure is directly proportional to the square of wind speed, as explained previously. When the airflow reaches the front surface of the radiator, this airflow is accelerated through the radiator openings (like vena contracta) so that higher values of dynamic pressure are obtained at the rear face of the radiator relative to the front. This results in a negative pressure drop across the radiator.

Kuthada et. al (2016) of FKFS also tested the pressure loss across the entire cooling system of the 2001 Ford Mondeo, including the condenser, radiator, and cooling fan, representing more blockage. They measured static pressure instead of dynamic pressure in the present study. However, his values also increase with wind speed as expected and are much higher due to the higher blockage (see Appendix C).

5.1.5 Effect of sealing on the pressure drop across the radiator

After measuring the above pressure drop data, the seals on the sides, top, and bottom (Fig. 5.8) were sequentially removed to test the effect of each seal on the pressure drop. Their effect on the pressure drop is recorded for 5 wind speeds to get a trendline for each case as shown in Fig. 5.8.

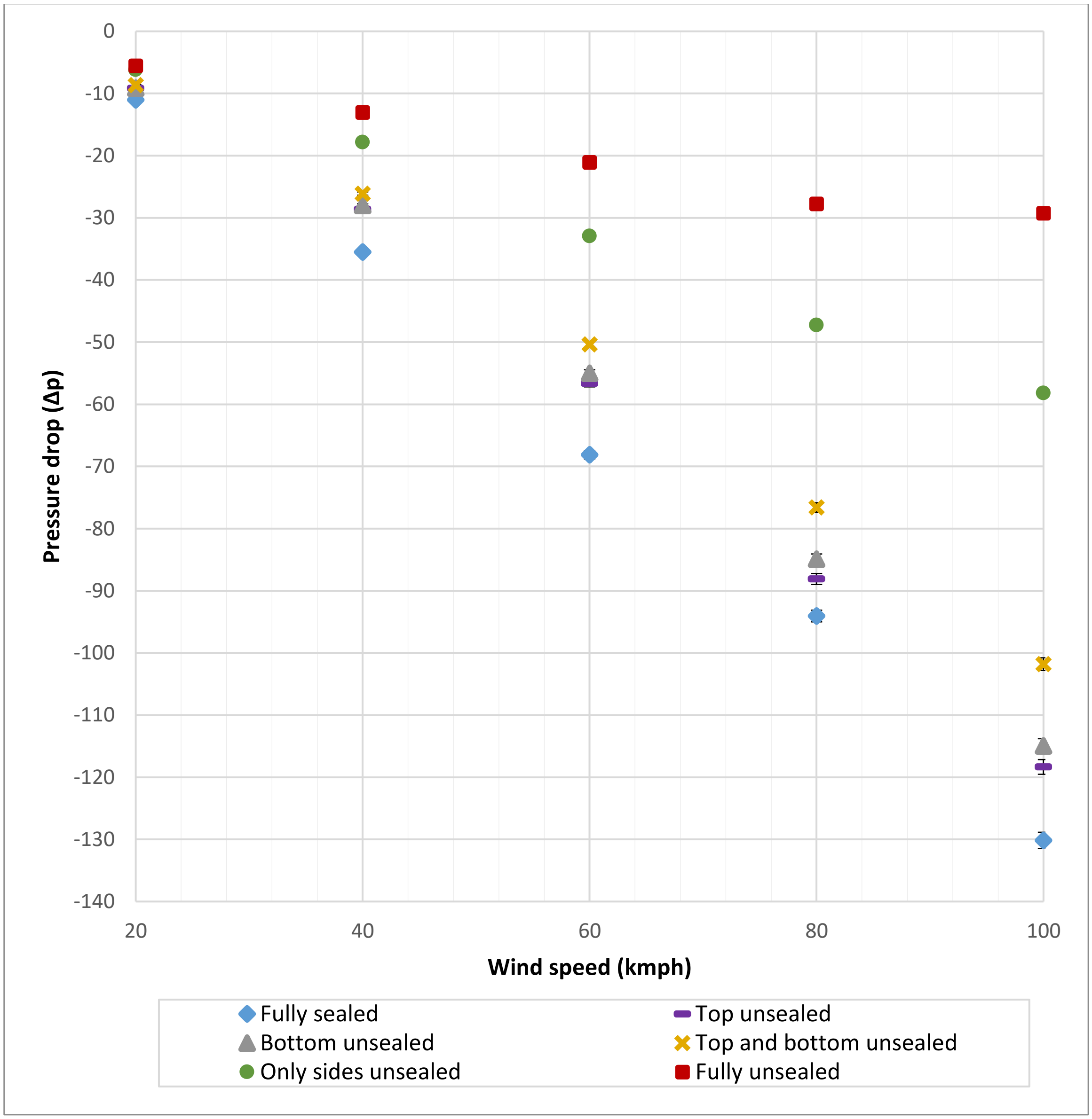

Figure 5.8 Effect of sealing on pressure drop across the radiator

The figure reveals the effect of sealing on the pressure drop values. There is a huge gap between the fully sealed and fully unsealed conditions. It is seen that the top seal has the least effect on the pressure drop while the side seals affect the pressure drop the most. This is because the gaps at the top and bottom are extremely small, which leads to a small effect on the pressure drop across the radiator. The size of the gaps on either side of the radiator is much greater than those at the top and bottom. This explains why the trendline for sides unsealed case is only smaller than the fully unsealed case.

This figure, thus, helps to clearly define the leakage characteristics of the testbench and how sealing different gaps in the testbench affects the pressure drop across the radiator. This information can be used to introduce a certain amount of leakage into the testbench depending on the test objectives.

5.2 Numerical Results

5.2.1 Preliminary pressure plate results

As discussed in Section 3.4, pressure plates were designed based on correlations developed by Idelchik (1989), and computational fluid dynamics (CFD) was used to verify the designs. The CFD was performed using a commercial software called ANSYS Fluent. The procedure is outlined in Section 4.2. Based on the calculations, the pressure plate developed for the preliminary simulation study was 0.5 inches thick and had a grid of φ = 144, which is an array of 16×9 holes (see Section 3.4.1). This plate had the closest coefficient of hydraulic resistance to the radiator (which was determined experimentally). It was also easiest to manufacture because of the large size of square holes and enough plate material separating adjacent holes (see Appendix E for preliminary simulation results). Hence, the plate was fabricated and tested in the wind tunnel for validation of the numerical simulations.

However, it was observed that the pressure drop across the preliminary square hole pressure plate in the simulation was greater than that from experiments, especially at high wind speeds. Therefore, the results from the experimental testing were used to further refine the numerical model so that it replicates the wind tunnel conditions better (see Appendix G for refined Fluent setup). The pressure drop results of the preliminary and refined simulations are compared with the plate tested in the wind tunnel as shown in Fig. 5.9. It is evident from the figure that the preliminary and refined results are similar up to speeds of 16 m/s, beyond which the former diverges from the experimental results. The refined simulation more accurately agrees with the experimental results for all speeds tested. However, it was observed the pressure drop created by this plate is much less than that of the radiator.

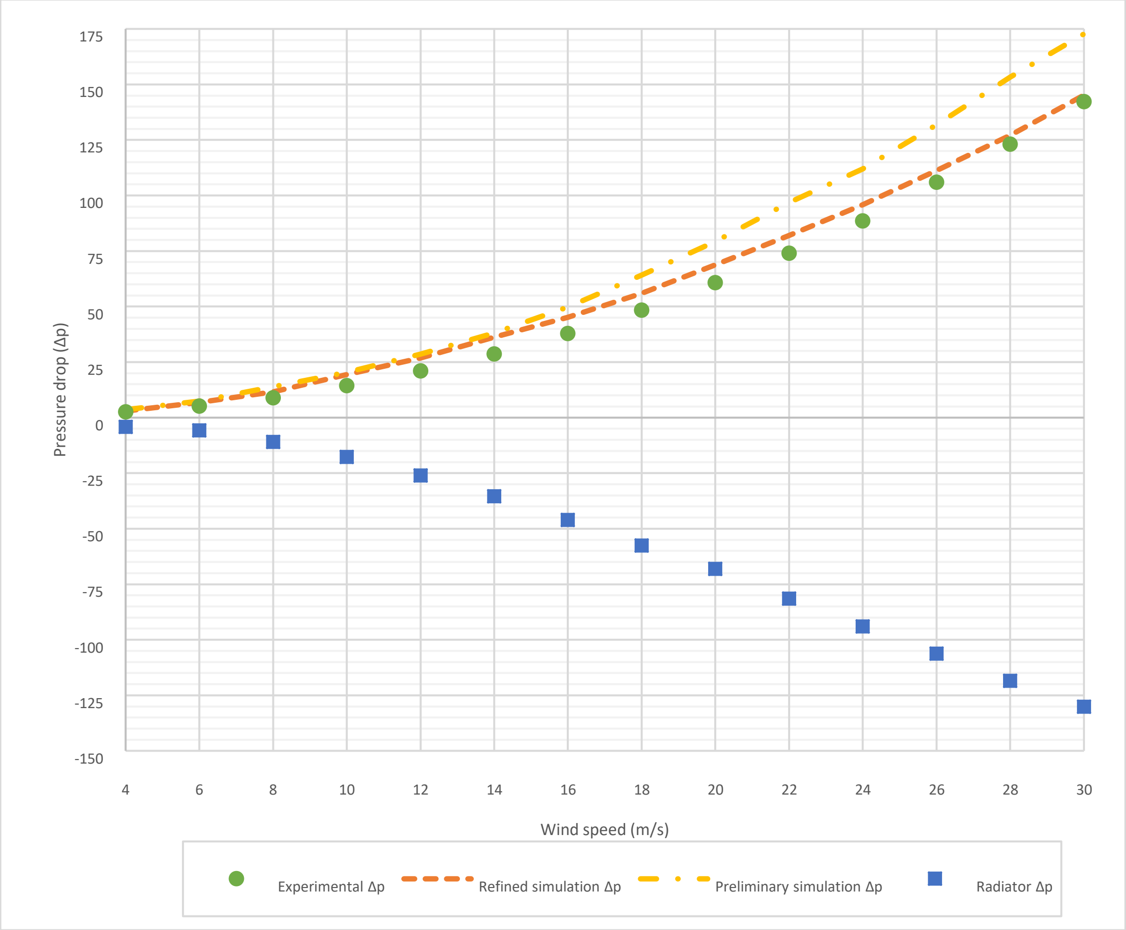

Figure 5.9 Pressure drop comparison between preliminary square hole pressure plate and radiator

This sign change between the pressure drop across the plate and the radiator can be explained by the fact that the blockage offered by the plate is not enough for the airflow to display vena contracta, as is the case for the radiator. The airflow that reaches the pressure plate only experiences a slight obstruction as the holes are too large while the plate material separating adjacent holes is very less. Instead of being accelerated after passing through the plate, the airflow gets decelerated and hence, showing a positive pressure drop. Therefore, further simulations were performed on the final pressure plate designed in Section 3.4.2.

5.2.2 Final pressure plate design results

Using the validated simulation setup mentioned above, numerous pressure plate designs were simulated again and compared with the pressure drop across the radiator, which was measured in the wind tunnel as described earlier. Figure 5.10 shows the numerical results of the final plate design and experimental results across the radiator. It is evident there is a good agreement between the results. In fact, the difference between the results is within 10% up to a speed of 22 m/s (79.2kph). The final plate design has $\varphi = 943$ circular holes (or an array of 41×23), each having a diameter of 18.14mm, resulting in a coefficient of hydraulic resistance of 0.943.

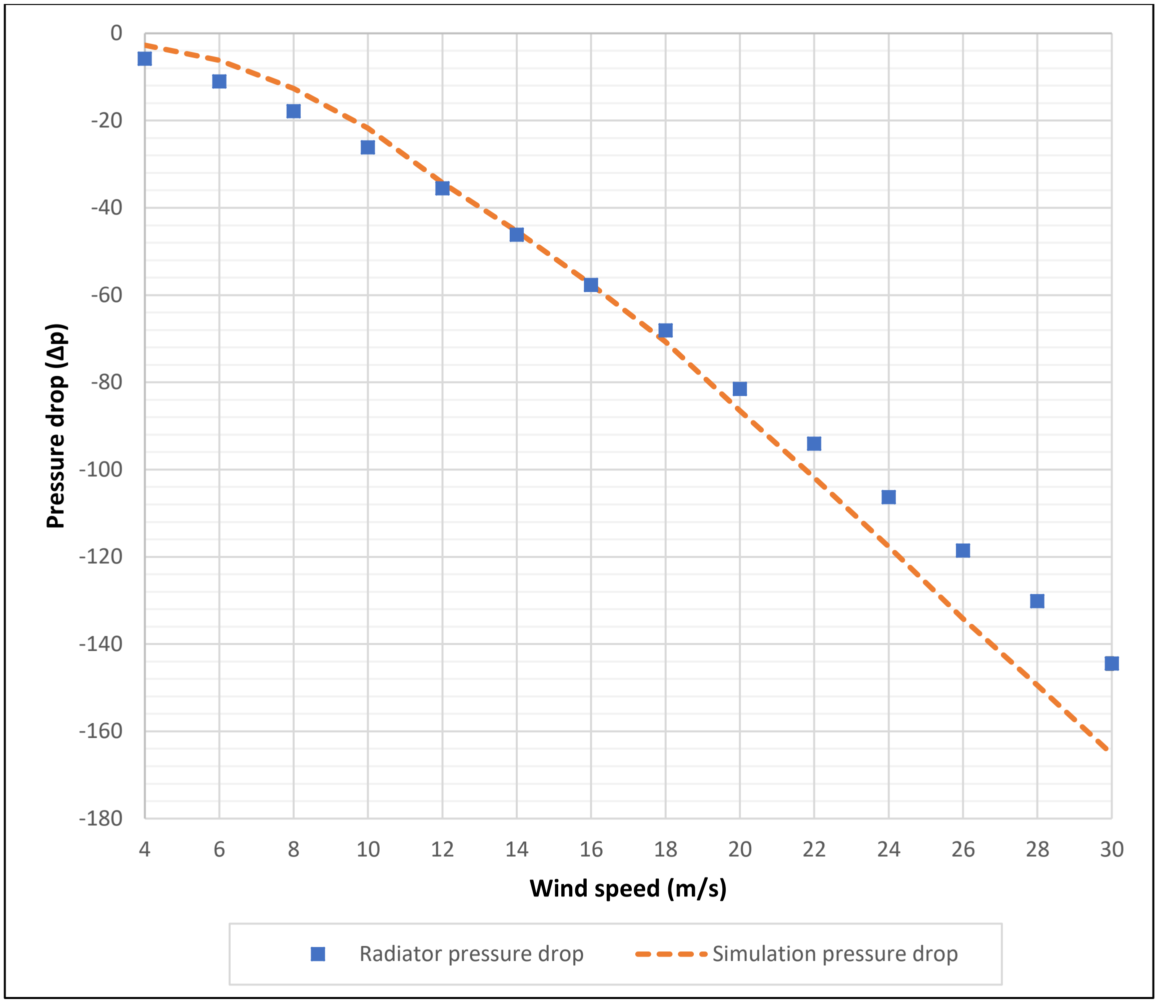

Figure 5.10 Pressure drop comparison between the radiator and final pressure plate

The presence of numerous small holes spread uniformly across the surface of the plate resulted in a consistent pressure drop across the entire plate. Since the simulation setup has been validated with the wind tunnel results, it can be concluded that the results are corroborated.

To show the uniformity of the pressure distribution across the final plate design, the dynamic pressure contour on the rear face of the plate is depicted in Fig. 5.11. It shows that the entire plate displays a consistently uniform dynamic pressure.

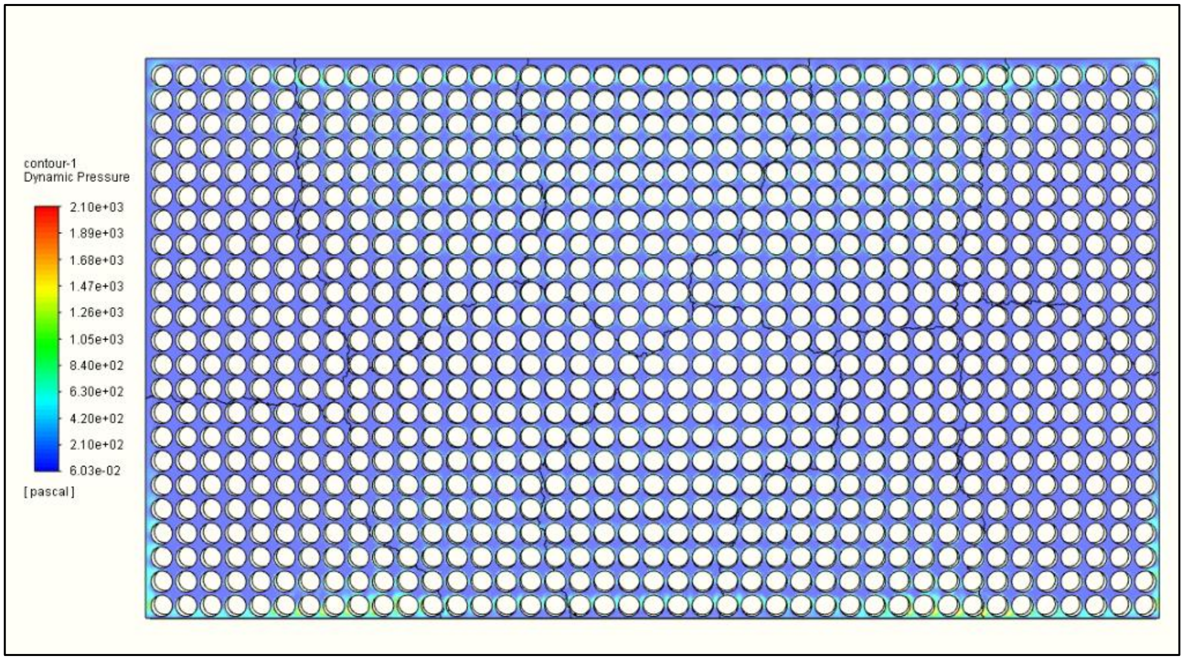

Figure 5.11 Dynamic pressure contour on rear surface of final pressure plate

5.2.3 Modification of the correlation

It was observed from this study that the correlation reported by Idelchik (1989) for calculating the coefficient of hydraulic resistance could not predict it accurately for the pressure plate due to the testbench structure and the resulting blockage. Therefore, it was decided to introduce a testbench factor (T_f) into the correlation to account for the effect of the testbench structure and the resulting blockage.

The coefficient of hydraulic resistance (ζ) from the correlation is therefore modified as follows:

$$\zeta = \left[\left(\zeta_o + \lambda . \frac{l}{d_h}\right) . \frac{1}{\bar{f}^2}\right] - \boldsymbol{T_f} \qquad (5.2)$$

where all the symbols are as defined in Eq 3.2 except $\boldsymbol{T_f} = (2.25 \times 10^{-4}) \times \frac{d_h}{l} \times \varphi$

For example, the final plate design has a ζ = 0.943, however, the target hydraulic resistance (for the radiator) was 0.64. Applying the modified correlation in Eq. 5.2 with a plate thickness, l, of 12.7mm, hole diameter, d_h, of 18.14mm, and the number of holes, φ, as 943, gives the following:

$$\zeta = 0.943 - \left[2.25 \times 10^{-4} \times \frac{18.14}{12.7} \times 943\right]$$

$$\zeta = 0.943 - 0.303$$

$$\zeta = 0.64$$

Chapter 6 Conclusions and Recommendations

6.1 Conclusions

The testbench designed in this research endeavor filled a critical void in the field of Active Grille Shutter testing. This testbench is capable of testing the functionality of AGS, and the pressure drop across a radiator with or without the other. Additionally, a pressure plate is also designed to replicate the radiator. Together, the testbench, the pressure plate as well as the testing procedure provide the platform for AGS testing in a wind tunnel for the first time. This thesis had six main objectives that have been achieved. The results and conclusions are summarized as follows:

I. A testbench that measures the functions and operating characteristics of AGS is designed, fabricated, and tested in the CWT at ACE at Ontario Tech University.

II. This testbench is capable of testing an AGS with or without the radiator as might be required by the OEM or the customer. This equips the testbench to test AGS systems even for electric and other hybrid vehicles, which may or may not use a radiator.

III. The dynamic pressure behind the AGS was measured by inserting the pressure tubing in and through the radiator from behind at 8 laterally and longitudinally different positions. This gives us an average value of dynamic pressure distribution across the radiator face, which in turn provides an estimate of the speed of air that passes through the AGS fins at different positions.

IV. The leakage effect of each seal on the pressure drop across the radiator is ascertained. This defines and quantifies the leakage characteristics of the testbench such that it can be altered to fit any OEM’s requirements as needed. OEMs and automotive companies that manufacture AGS can henceforth use this testbench for the design and implementation of various Active Grille Shutter configurations.

V. The dynamic pressure comparison between the test vehicle and the sealed testbench for AGS partially open, and close, and the test vehicle and unsealed testbench for the AGS open condition show that the testbench has a good agreement with the actual dynamic pressure values measured in the test vehicle. This also shows that sealing the area around the AGS and the radiator has detrimental effects on dynamic pressure values. This proves the accuracy and consistency of the testbench in measuring the operating characteristics of the testbench, validates its functionality, and proves its effectiveness in testing flow and leakage parameters related to AGS operation

VI. A pressure plate design has been numerically simulated using ANSYS Fluent and the pressure drop across the radiator was replicated onto the plate. This pressure plate is capable of replicating the radiator pressure drop and can effectively replace the radiator in the testbench. It can help set a benchmark parameter for the testbench as the only variable that would affect the results from an AGS testing scenario would be the AGS itself, which will substantially increase the uniformity of the testing process. This pressure plate is based on a commercially available crossflow plastic aluminum radiator and thus its application is limited to only those automobiles that use such kind of a radiator. However, this is the most common radiator in the market.

VII. A Testbench factor (T_f) has been introduced that predicts the coefficient of hydraulic resistance for the pressure plate when it is inside the testbench. This provides a more accurate value for hydraulic resistance for the testbench than the generic correlation reported.

VIII. This research is the first step towards standardizing AGS testing in a wind tunnel and further improvement down the suggested lines should lead to the formulation of an SAE Testing Standard.

IX. The limitation of the testbench is that it is only capable of testing AGS used in small vehicles such as sedans and hatchbacks, but cannot test AGS that are used in larger vehicles such as SUVs, trucks, etc.

6.2 Recommendations

The following recommendations can also be considered to further improve the performance of the testbench:

- The final pressure plate should be fabricated and tested in the testbench. This will establish a benchmark against which future AGS can be tested and compared.

- Install static pressure measurement rings in the walls of the testbench to measure the static pressure of the first cavity between the AGS and the plate and the second cavity behind the plate that contains the 3D printed engine. This will help to measure the static pressure inside these cavities for different AGS configurations. This will provide a better understanding of the flow physics which can later be quantified.

References

ANSYS. 2013. “ANSYS Fluent Theory Guide.” ANSYS Inc.

ANSYS. 2017a. “ANSYS Fluent.” http://www.ansys.com/Products/Fluids/ANSYSFluent.

ANSYS. 2017b. “ANSYS Fluent User’s Guide.” ANSYS Inc.

B. Hupertz., L. Kruger, K. Chalupa, N. Lewington, B. Luneman, P. Costa, T. Kuthada, C. Collin, *“Introduction of a new full-scale open cooling version of the DrivAer generic car model.”*, Progress in vehicle aerodynamics and thermal management (2018)

Badgujar Pankaj R., Rangarajan S, Nagaraja S. R., “*Analytical Performance Analysis of Cross Flow Louvered Fin Automobile Radiator”* MATEC Web of Conferences 172, 02003 (2018).

Berneburg, H. and Cogotti, A., *“Development and Use of LDV and Other Airflow Measurement Techniques as a Basis for the Improvement of Numerical Simulation of Engine Compartment Air Flows,”* SAE Technical Paper 930294, 1993, https://doi.org/10.4271/930294.

Cho, J., Park, J., Yee, K., and Kim, H.L., *“Comparison of Various Drag Reduction Devices and Their Aerodynamic Effects on the DrivAer Model,” SAE Int. J. Passeng. Cars – Mech. Syst.* 11(3):225-237, 2018, doi:10.4271/06-11-03-0019.

Cho, Y., Chang, C., Shestopalov, A., and Tate, E., "Optimization of Active Grille Shutters Operation for Improved Fuel Economy," SAE Int. J. Passeng. Cars - Mech. Syst. 10(2):2017, doi:10.4271/2017-01-1513.

Chunhui Zhang, *"Numerical simulation based analysis of road aerodynamic flows"* dissertation for Doctor of Philosophy in Mechanical Engineering, The University of North Carolina at Charlotte, 2018.

Collin, C., Mack, S., Indinger, T., and Mueller, J., *"A Numerical and Experimental Evaluation of Open Jet Wind Tunnel Interferences using the DrivAer Reference Model,"* SAE Int. J. Passeng. Cars – Mech. Syst. 9(2):2016, doi:10.4271/2016-01-1597

E Y Ng, S Watkins, and P W Johnson, *"New pressure based methods for quantifying radiator airflow"* Proceedings of the Institution of Mechanical Engineers, Part D: Journal of Automobile Engineering 2004.

Eton Y. Ng, Simon Watkins, Peter W. Johnson, and Lindsay Mole, *"Measuring Local Time-Averaged Airflow Velocity through an Automotive Heat Exchanger"* 14th Australian Fluid Mechanics Conference, December 2001.

Eton Yat-Tuen Ng, "*Vehicle engine cooling systems: assessment and improvement of wind-tunnel based evaluation methods"* RMIT University, Melbourne, Australia, August 2004.

Ford Motor Company of Australia Limited, 2020. *https://www.ford.com.au/technology/active-grill-shutter/#:~:text=Electronically%20controlled%20by%20an%20engine,closes%20when%20it%20doesn't*

Heft, A., Indinger, T., Adams, N., *"Experimental and numerical investigation of the DrivAer Model",* ASME 2012 Fluids Engineering Summer Meeting FEDSM2012.

Idel'chik, I.E. *"Flow Resistance: A design guide for engineers"* published in 1989.

Ibrahim, Mohamed et al. *"Design and Analysis of an Active Underbody Aerodynamic Device for Tractor Trailers."* ProQuest Dissertations Publishing, 2018. Web.

Jiang, Bin, et al. *"Numerical Investigation of Flow and Heat Transfer in a Novel Configuration Multi-Tubular Fixed Bed Reactor for Propylene to Acrolein Process."* Heat and Mass Transfer 51.1 (2015): 67–84. Web.

Team Ford, Canada, 2018, Keeping your cool: Active Grille Shutters on the Ford Focus. *https://www.teamford.ca/2018/03/27/active-grille-shutters/*

Kheirallah, Mike et al. *"Aero-Acoustic Optimization of a Cooling Fan Using Mesh Morphing Technique in Minimizing the Acoustic Surface Power."* ProQuest Dissertations Publishing, 2017. Web.

Kiel, G., *"Total head meter with small sensitivity to yaw, Technical Memorandum 775"* Washington DC, National Advisory Committee for Aeronautics, May 1935.

Krayenhoff, E.S., Voogt, J.A, *"A microscale three-dimensional urban energy balance model for studying surface temperatures."* Boundary-Layer Meteorol 123, 433–461 (2007). https://doi.org/10.1007/s10546-006-9153-6

Kuthada, T., Wittmeier, F., Bock, B., Schoenleber, C. et al., *"The Effects of Cooling Air on the Flow Field around a Vehicle,"* SAE Int. J. Passeng. Cars - Mech. Syst. 9(2):2016, doi:10.4271/2016-01-1603.

Li, JiaCheng; Deng, YaDong; Wang, YiPing; Su, Chuqi; Liu, Xun; *"CFD-Based research on control strategy of the opening of Active Grille Shutter on automobile"*, Case studies in Thermal Engineering 12 (2018) 390-395.

Lokanath Mohanta, Arindom Joardar, Jack L. Esformes, Brian Videto & Tobias H. Sienel (2019), "*Numerical Analysis of Fluid Flow and Heat Transfer in Wavy and Hybrid-Slit-Wavy Fin-and-Tube Heat Exchangers*", Science and Technology for the Built Environment, 25:6, 767-775, DOI: 10.1080/23744731.2019.1600333

Menter, F. 1993 "*Zonal Two Equation K-W Turbulence Models For Aerodynamic Flows.*" In 23rd Fluid Dynamics, Plasmadynamics, and Lasers Conference. doi:10.2514/6.1993-2906.

Pfeifer, C., "*Evolution of Active Grille Shutters,*" SAE Technical Paper 2014-01-0633, 2014, doi:10.4271/2014- 01-0633.

Pointer, W. 2004. "*Evaluation of Commercial CFD Code Capabilities for Prediction of Heavy Vehicle Drag Coefficients.*" 34th AIAA Fluid Dynamics Conference and Exhibit, no. July: 1–10. doi:10.2514/6.2004-2254.

Prof. A.R. Khot and Prof. D.G. Thombare, "*An overview of radiator performance evaluation and testing*." IOSR Journal of Mechanical and Civil Engineering (IOSR-JMCE) (2014).

R.M. Manglik and A. E. Bergles, "*Heat transfer and pressure drop correlations for the rectangular offset strip fin compact heat exchanger*." *Experimental Thermal and Fluid Science* 1995.

Ruijsink, R., The Use of the MicroProbe System in Cooling System Development. MIRA, 3th Int. Conference of Vehicle Aerodynamics, Warwick (UK), 2000.

SAE International J1994, *“Laboratory Testing of Vehicle and Industrial Heat Exchangers for Heat Transfer and Pressure Drop Performance”,* September 2015.

SAE International Surface Vehicle Information Report J2082 *“(R) Cooling Flow Measurement Techniques”,* Issued 1992-06, Revised 2018-09.

Saheby, E. B., Guoping, H., & Hays, A. (2019), “*Design of hypersonic forebody with submerged bump*”, Proceedings of the Institution of Mechanical Engineers Part G: Journal of Aerospace Engineering, 233(9), 3153–3169. https://doi.org/10.1177/0954410018793288

Sam Bonser, Ben Richard Hughes & John Kaiser Calautit (2020), “*Investigation of the impact of roof configurations on the wind and thermal environment in football stadiums in hot climates*”, International Journal of Ventilation, 19:4, 260-279, DOI: 10.1080/14733315.2019.1665861

Shahid, Seham, and Martin Agelin-Chaab. “*Development and Analysis of Techniques to Improve Air-Cooling and Temperature Uniformity in Battery Packs*.” ProQuest Dissertations Publishing, 2017. Web.

Spectra Premium Inc., Cooling system training manual

https://www.spectrapremium.com/ressources/televerser/[422]

Taylor, John R. (John Robert), 1939 –

An introduction to error analysis / John R. Taylor. – 2nd ed.

Technical University of Munich (TUM), 2011. *https://www.mw.tum.de/en/aer/research-groups/automotive/drivaer/*

United Sensor Corporation, © 2015.

https://www.unitedsensorcorp.com/kiel.html

Wilcox, D.C. 1993, “*Turbulence Modeling for CFD*”. DCW Industries, Inc. La Canada, California. doi:0963605151.

Wittmeier, F. and Kuthada, T., "*Open Grille DrivAer Model - First Results*", *SAE Int. J. Passeng. Cars - Mech. Syst.* 8(1):2015, doi:10.4271/2015-01-1553.

Yu, Kuahai, and Xi Yang. “*Aerodynamic and Heat Transfer Design Optimization of Internally Cooling Turbine Blade Based Different Surrogate Models.*” Structural and Multidisciplinary Optimization 44.1 (2011): 75–83. Web.

Appendices

Appendix A - DrivAer Model

Before the development of the DrivAer Model (TUM, 2011) by the Technical University of Munich in Germany, most of the automotive aerodynamic research was based upon the generic Ahmed body design or the SAE body. These models help to gain a basic understanding of a simple flow over the vehicle but fail to predict anything with an acceptable level of accuracy. However, production vehicles are much more complex and many times what design shows favorable results when used with the generic models, these designs may display results which are not as expected. One fix to this problem is to use a CAD model of the vehicle that is to be tested, but this introduces a great degree of uncertainty as each manufacturer has different specifications and dimensions for a vehicle of the same class, which involve complex body structures, like the A-pillars, the high degree of curvature in the rear end or the wheel housing region, and this makes automotive aerodynamic testing highly complex and subjective. This was the reason behind the development of the DrivAer Model.

The idea behind the development of the DrivAer model is to bridge the gap between the simplicities of the Ahmed and the SAE body and the complexities of a production vehicle. The design of the DrivAer model consists of almost all the external features that are present on a production passenger vehicle, such as the headlights, front grille, side mirrors, wheels, and wheel wells, and rear lights to name a few. The basic dimension of this model is based on a combined design of two production passenger sedans, the Audi A4 and the BMW 3 Series. This model has three basic types of rear-end configuration, namely, fastback, estate back, and notchback, which can be used interchangeably to test the impact of various designs on the aerodynamics of the vehicle.

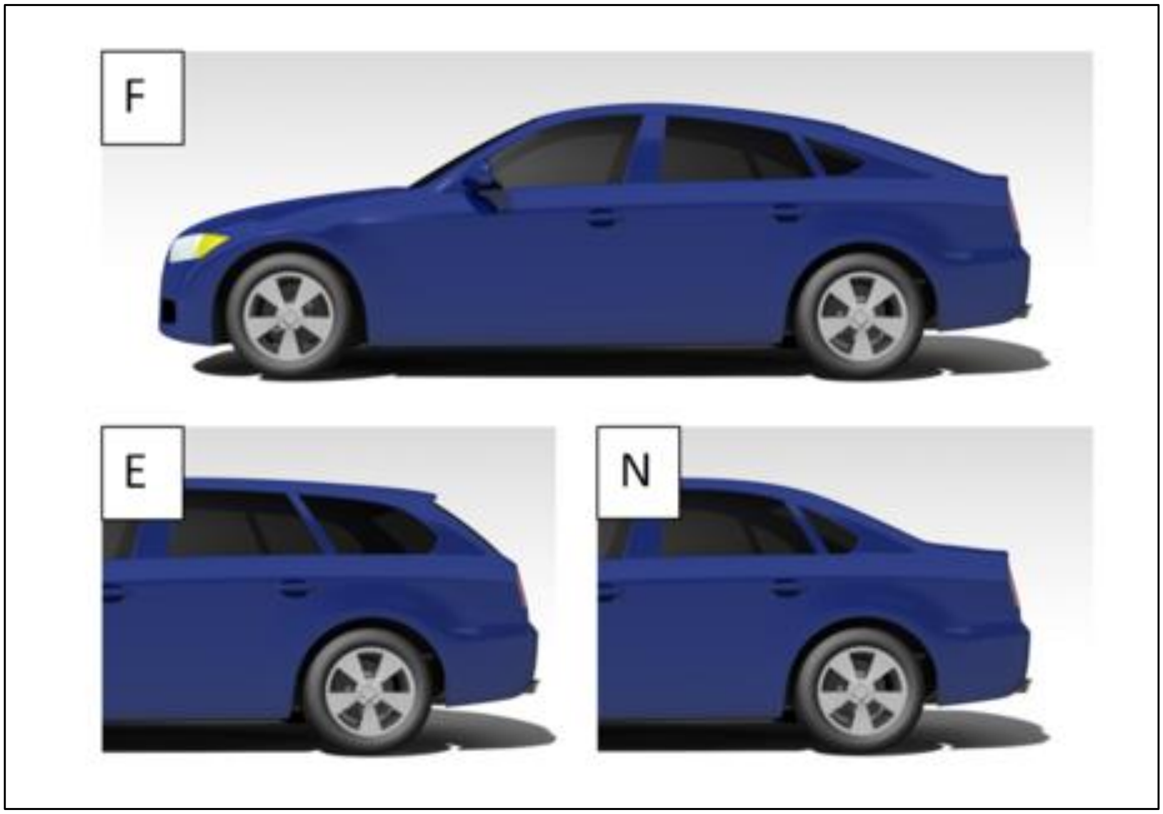

Figure A.1 DrivAer model with different rear end configurations (TUM, 2011)

The design of the internal components of the vehicle influences the aerodynamics of the vehicle considerably, and this possibility of improved flow through the engine bay region and the underbody of the vehicle has led to the development of a simplified version of the engine bay geometry which has been recently added to the DrivAer Model.

To allow a wide variety of investigations, the DrivAer Model has been developed with 18 different mock-up configurations. These include detailed, simple, and smooth underbody, simplified designs of the 4-cylinder engine, gearbox, and transmission, radiator, cooling air duct, and the front grille.

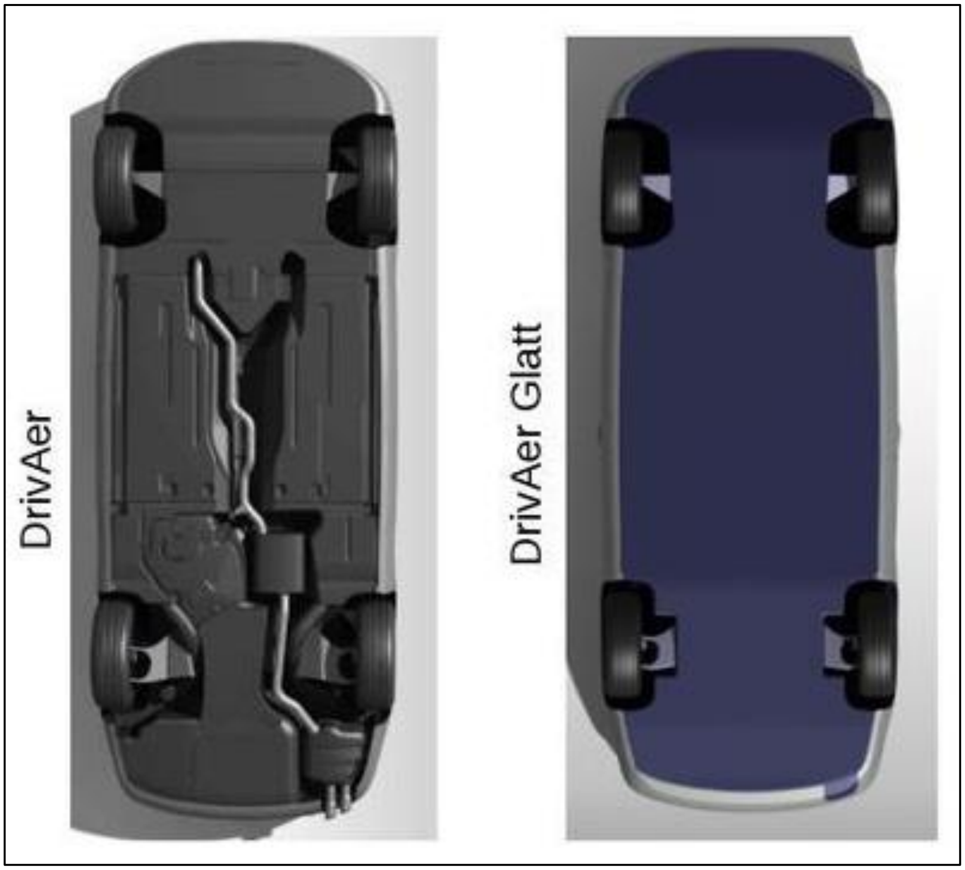

Figure A.2 Different underbody configurations (TUM, 2011)

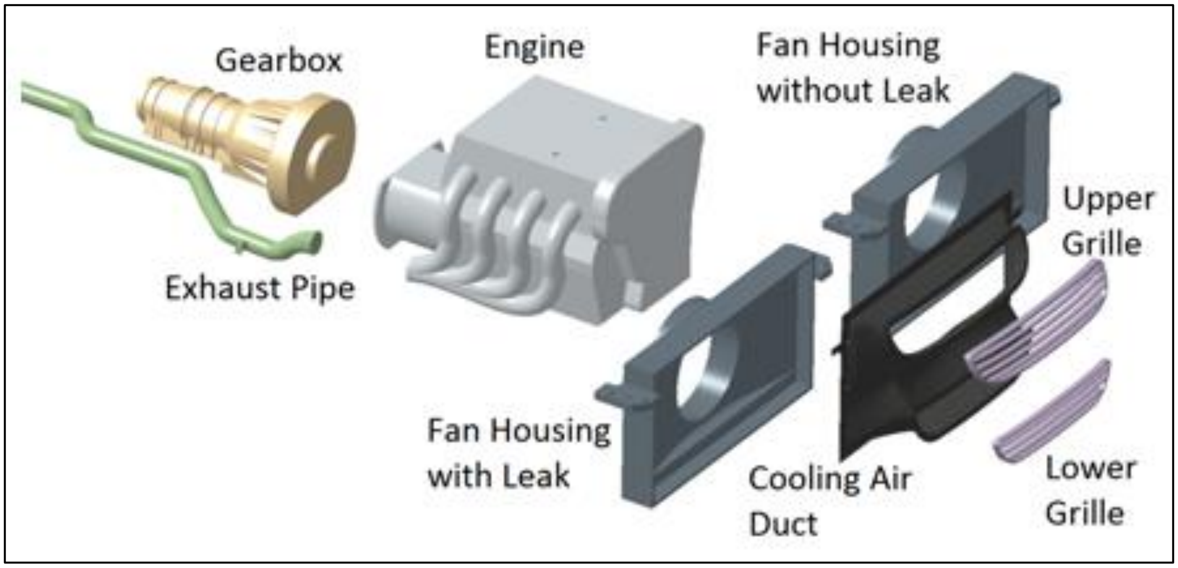

Figure A.3 Exploded view of the engine bay flow parts (TUM, 2011)

Different configurations of the DrivAer are available to be tested for aerodynamic purposes. The nomenclature for the configurations has been derived that lends a better understanding of this system:

1. The first letter in the abbreviation describes the geometry of the rear end
    a. **F** for fastback
    b. **E** for estate back
    c. **N** for notchback
2. The second group of letters describes the underbody details
    a. **D** for detailed underbody
    b. **S** for smooth underbody
    c. **EB** for engine bay flow
3. The third group of letters describes the mirror configuration
    a. **wM** with mirrors
    b. **woM** without mirrors
4. The fourth group of letters describes the wheel configuration
    a. **wW** with wheels
    b. **woW** without wheels
5. The fifth is an optional group of letters which describes the radiator configuration
    a. **wL** with leakage around the cooler
    b. **woL** without leakage around the cooler

So according to this nomenclature, the abbreviation **F_EB_wM_wW_woL** refers to a fastback rear end configuration with engine bay flow, mirrors, and wheels and without leakage.

Appendix B - COUPLE Scheme

This study employs the use of a pressure-based solver that allows us to solve the flow equations in a single or a coupled manner. The COUPLE scheme has certain advantages over the single or non-coupled approaches. This scheme offers an improved performance and provides an efficient and robust solution as compared to the single counterparts.

The pressure-based SIMPLE or SIMPLEC scheme solves the momentum and pressure correction equations separately. This is essentially problematic for a system that is unsteady and has some transient properties, leading to a very slow convergence after a large number of iterations. The COUPLE algorithm, however, solves these equations together. Although this makes each iteration take a longer time, the solution stabilizes much earlier and reduces the number of iterations required for convergence by a huge margin.

Appendix C – Pressure drop comparison

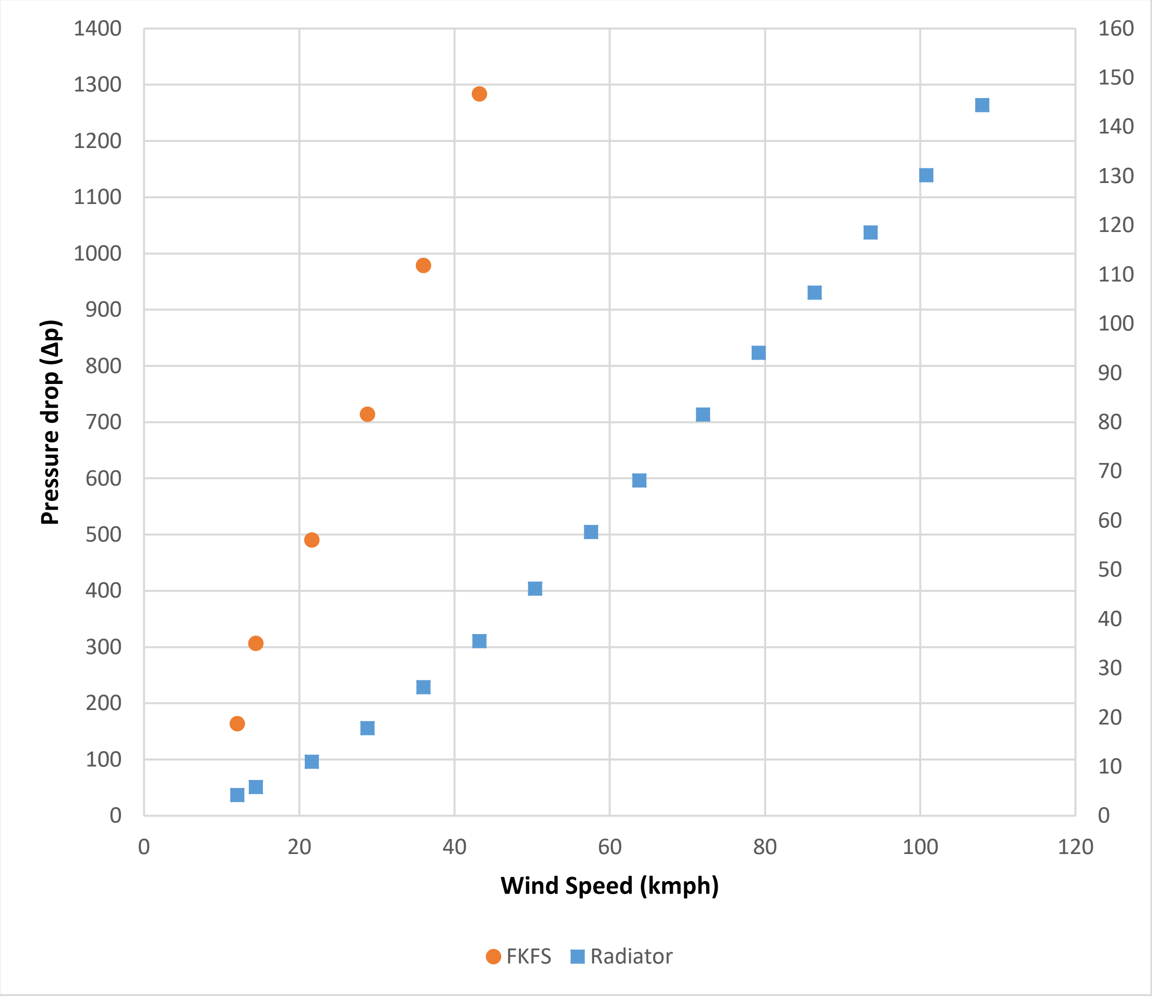

Figure C.1 Pressure drop comparison (Static pressure)

Appendix D - Frontal area comparison of test vehicle versus testbench

Figure D.1 Overlay of testbench on the test vehicle

Appendix E – Preliminary simulation results

Different number of holes and thicknesses of the plate were simulated and parameterized. For these, the number of holes were selected as 170, 176, and 180 in a plate of thickness 1 inch and 0.5 inches each. These are simulated with similar setup conditions as described in Section 4.2. The specific numbers of holes and plate thicknesses were chosen based on the closeness of the hydraulic resistance to that of the radiator as derived from the formula for the coefficient of hydraulic resistance (Eq. 3.2).

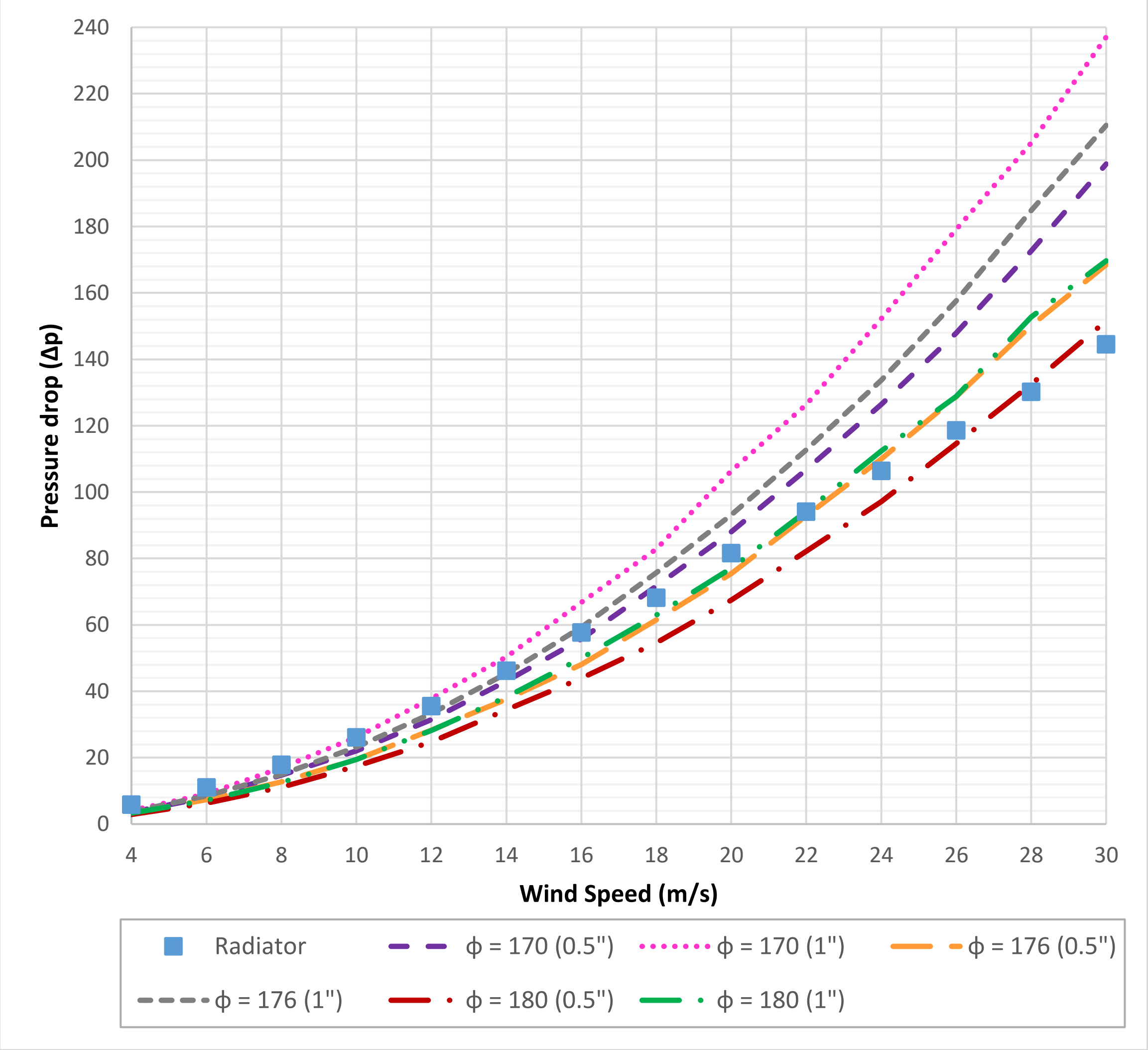

Figure E.1 Pressure plate design comparison

It was observed in Fig. E.1 that only the plates with $\varphi = 176$ and 180 and thicknesses of 0.5 inch and 1 inch, respectively, have values close to the radiator's pressure drop values.

It is seen that the pressure drop results from simulations are parabolic in nature for every plate configuration whereas the radiator shows an almost linear trend. This can be attributed to the experimental testing, where only 8 tubing and 7 probes are used for measuring the dynamic pressure on the entire front and back faces, respectively. Although the probes capture the essence of the dynamic pressure, the resolution is too low to measure the details captured by the numerical simulation. Note that the probes are located at only the central region of the radiator and their measurement of dynamic pressure is averaged to get the value on the entire surface of the plate. This is further supported by previous results from FKFS (Kuthada et. al 2014, 2016). It is worth noting that their results also show similar parabolic trends as the present study.

Table E.1 below shows the comparison of the radiators' pressure drop with the overall average of pressure for all the pressure plate designs. The color scheme is as follows: *Red*, if the difference between Δp of the radiator and the plate is greater than ±33%, *Yellow*, if the difference is within the range of ±33%, and *Green* if the difference is within ±10%. It is seen that two designs, $\varphi = 176$ and 180 with a thickness of 0.5" and 1" respectively, both show five values each which are within ±10%, whereas all other designs show either 4 or 3, with more values outside the range of ±33%.

Table E.1 Pressure plate design comparison

Speed	***Radiator***	***φ = 170 (0.5")***	***φ = 176 (0.5")***	***φ = 176 (1")***	***φ = 180 (0.5")***	***φ = 180 (1")***	***φ = 170 (1")***
4	5.814	3.593	**3.219**	3.748	2.891	**3.309**	4.091
6	11.007	8.052	**7.381**	8.522	6.329	**7.218**	9.065
8	17.829	14.738	**12.714**	14.957	11.077	**12.564**	17.002
10	26.102	22.024	**19.444**	23.157	17.459	**19.444**	26.146
12	35.496	31.461	**28.251**	33.288	24.693	**28.137**	37.803
14	46.160	43.091	**37.567**	45.415	34.402	**38.243**	50.327
16	57.703	55.746	**48.085**	59.327	43.926	**49.944**	66.763
18	68.116	71.704	**61.536**	75.715	54.563	**62.977**	82.818
20	81.536	88.020	**75.478**	93.109	67.506	**76.944**	106.380
22	94.066	106.736	**92.847**	112.702	82.165	**94.111**	126.315
24	106.338	126.442	**110.027**	133.744	97.111	**112.178**	152.280
26	118.548	146.952	**128.728**	157.642	114.605	**128.698**	179.163
28	130.161	172.646	**150.094**	184.828	132.431	**152.375**	205.116
30	144.459	198.826	**168.481**	210.469	151.573	**169.496**	237.064

These two designs, φ = 176 with 0.5-inch thickness, and φ = 180 with 1-inch thickness are the best representation of the radiator in terms of generating similar pressure drops. However, it is much easier to fabricate and machine a plate which is 0.5-inch in thickness rather than a 1-inch thick plate. And on top of this, the 0.5-inch plate would be much lighter than the 1-inch plate. Hence, the plate with φ = 176 and 0.5-inch thickness is chosen as the best representation of the radiator.

Fig. E.2 compares the pressure drop across the radiator and pressure plate.

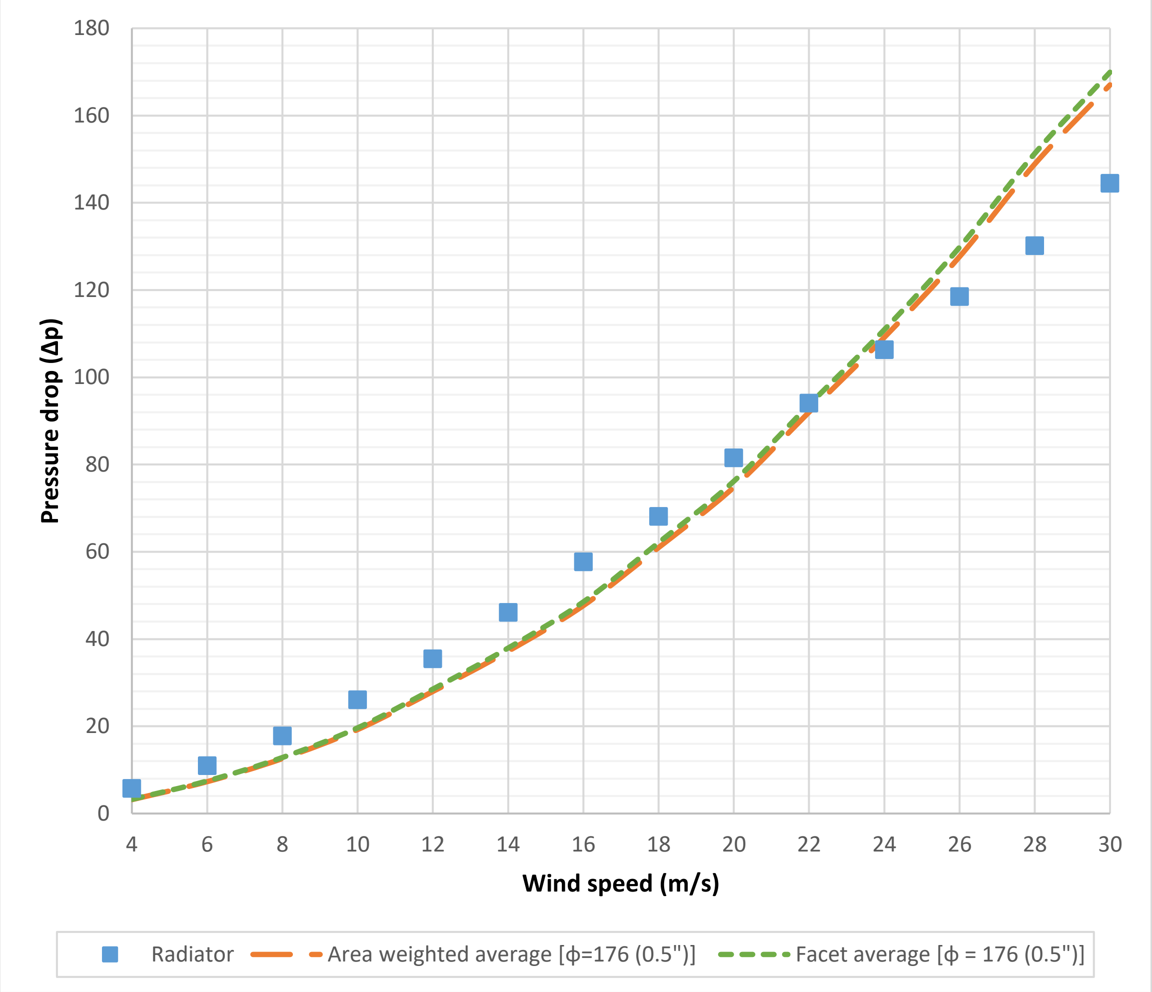

Figure E.2 Δp of radiator versus Δp of pressure plate

Two techniques have been used to estimate the pressure drop across the plate: facet average and area weighted average. The facet average function sums up the dynamic pressure of all the facets (each small mesh face) on the front and back surfaces of the pressure plate separately and then divides each by the total number of facets, irrespective of the size of the facet. However, the area-weighted average function multiplies the dynamic pressure of each facet with its area, adds up everything, and then divides by the total area of the plate. A brief description of these methods and the formulas used is given in Section 4.2.2.5 and 4.2.2.6. Fig. E.2 shows that the pressure drop trends of the plate are consistent with the radiator, and this proves that the design configuration chosen for the pressure plate is a good representation of the radiator.

As described in section 4.2.2.1, the design of the testbench was simplified before being uploaded to ANSYS to stabilize the simulations and their results. The actual dimensions of the inner region of the testbench are smaller, and the dimensions of the plate suggested above (φ = 176 and 0.5inch thick) had to be reduced so that it could be fitted inside the testbench. The dimensions of the earlier plate were 906mm × 543mm × 12.7mm and they were revised to be 850mm × 475mm × 12.7mm. To keep the hydraulic resistance of the new plate similar to the earlier plate, the number of holes were reduced to 144 (16 × 9) which resulted in the coefficient of hydraulic resistance being 0.78 as opposed to 0.72 for the earlier plate. The pressure drop for the revised plate was simulated and is plotted against the previous plate as shown in Fig. E.3.

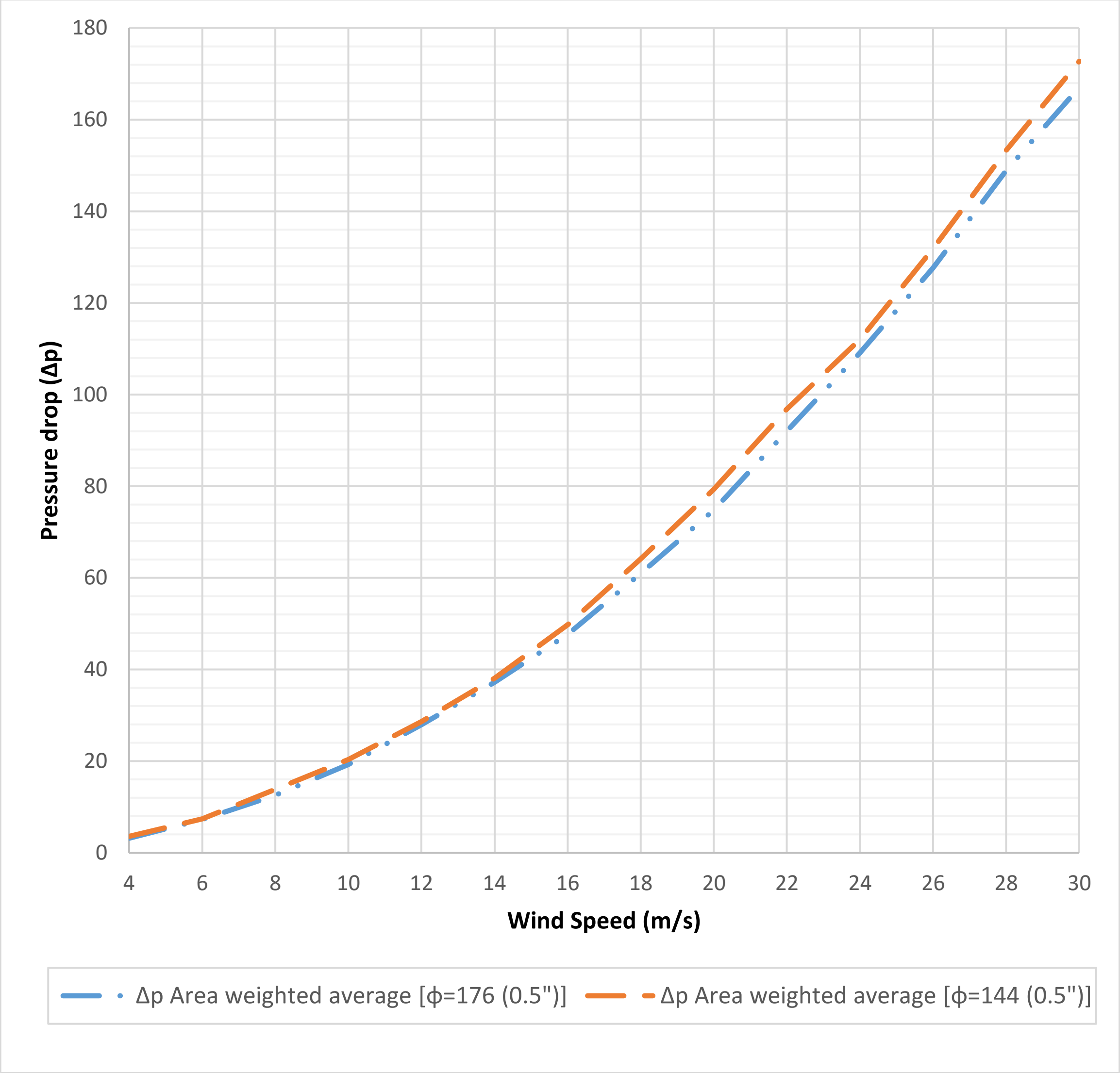

Figure E.3 Pressure drop comparison between the original plate and altered plate

As can be seen from the figure above, the difference in the pressure drop between the two plates is almost negligible. Hence, this plate was fabricated.

Appendix F – Preliminary simulation based experimental testing

The selected pressure plate design was pressure jet cut with the assistance of a commercial fabricating establishment.

Figure F.1 Pressure jet cut plate (φ = 144 and 0.5inch thick)

The plate was then fitted inside the testbench. The sides, top, and bottom of the plate were sealed in the same manner as before to restrict the airflow through the designated plate area.

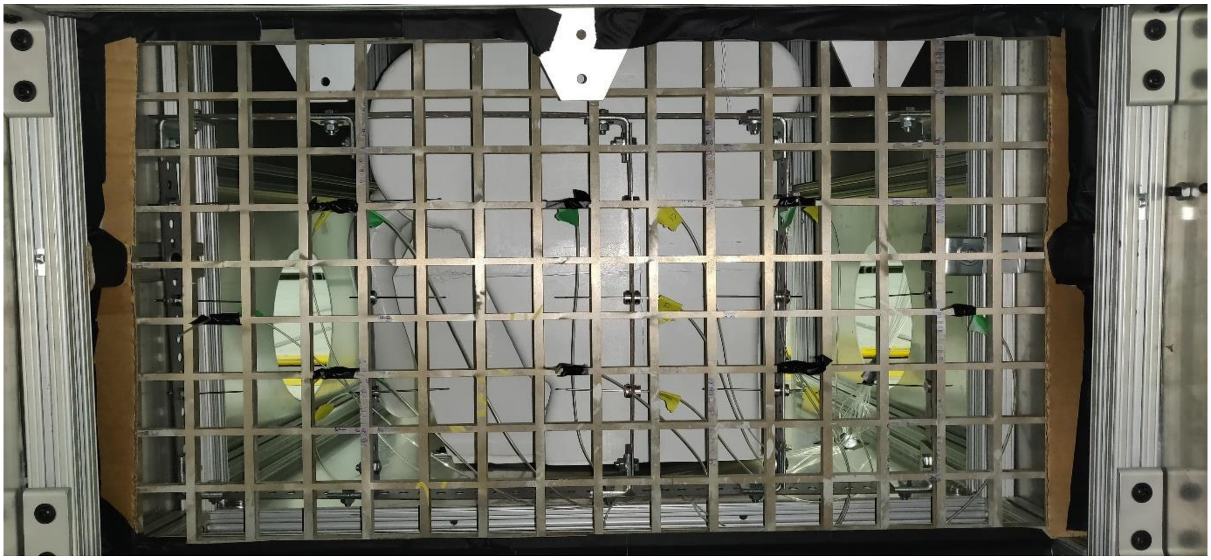

Figure F.2 Plate fitted and sealed inside the testbench

The measuring pressure tubing was fitted in the same positions as they were in the radiator when it was tested for pressure drop across it. Then the testbench was setup in the same position in the wind tunnel and the pressure tubing was connected to the Scanivalve in the same way as the tests before to ensure the similarity of test conditions.

Upon measuring the pressure drop across the pressure plate, it was found that the plate showed results that were very different from the radiator. This is due to the fact that the blockage offered by the plate is not enough for the airflow to display vena contracta, as is the case for the radiator. Instead of being accelerated after passing through the plate, the airflow gets decelerated and shows a positive pressure drop. The airflow that enters the testbench and reaches the pressure plate faces only a slight obstruction to flow as the cavities in the plate are too large while the plate material separating two square holes is very small in size. So this leads to a reduction in the speed of airflow instead of accelerating it, as was the case in the radiator. The results are depicted below:

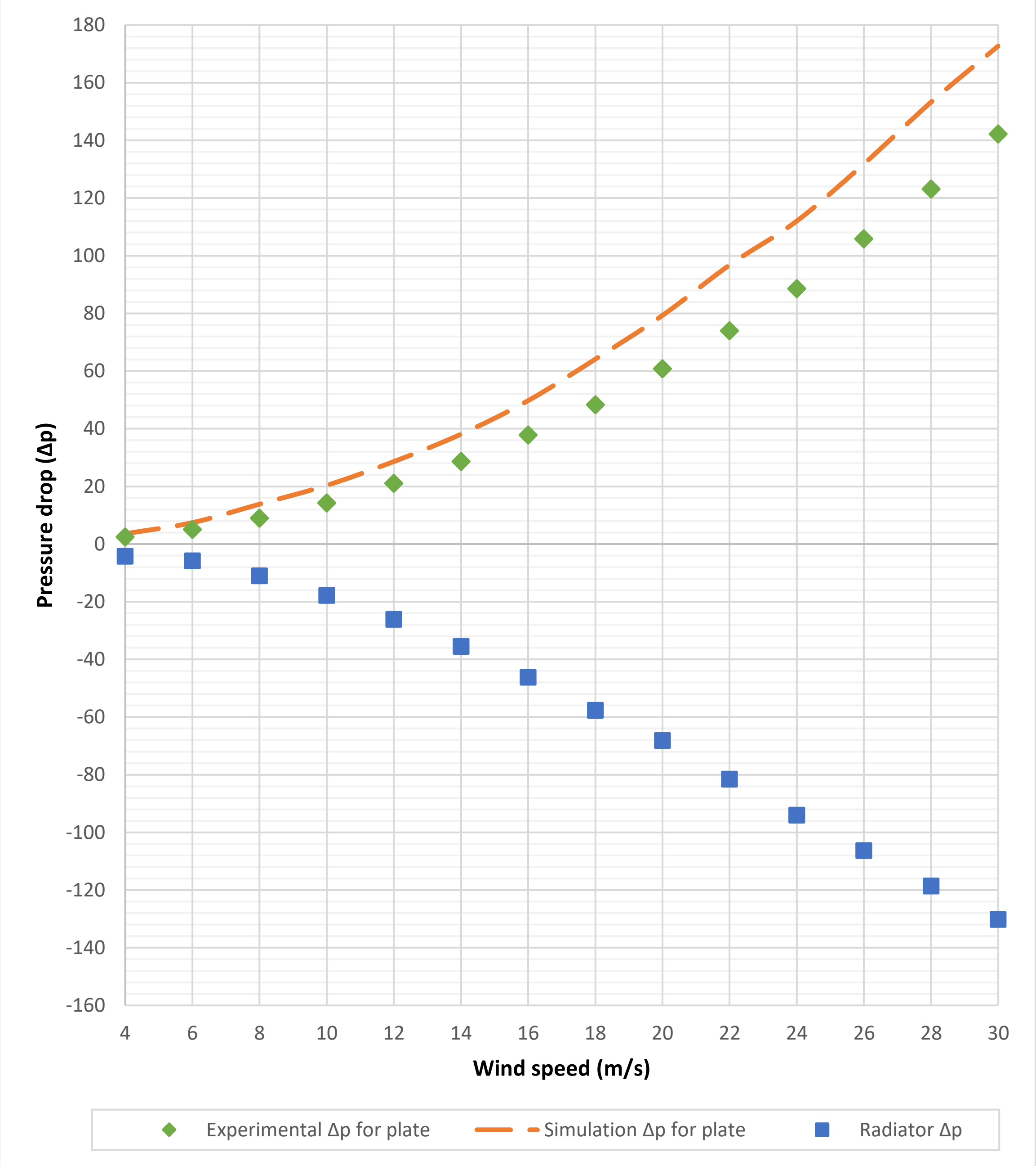

Figure F.3 Pressure drop comparison between radiator and pressure plate

Although there is a good level of agreement between the experimental and simulation results, there still exists a noticeable difference. This difference can be attributed to the fact that the dynamic pressure measuring points and the method used in the experimental testing and the simulations respectively, is different. The simulation uses an area or facet based function to average the dynamic pressure for the front and back surface of the pressure plate whereas the pressure tubing and the Kiel probes measure the dynamic pressure at those specific points only, which are 20mm in front (tubing) and 45mm behind the plate (Kiel probe) respectively.

Appendix G – Refined Fluent setup

Instead of measuring the dynamic pressure on the surface of the plate as was done in the preliminary simulations, the measuring points were now selected in such a way that their position corresponds to the measuring position of the tubing (front) and the Kiel probe (back) in the experimental testing. Instead of using area weighted or facet average method to calculate the dynamic pressure as was done prior, vertex averaging method (see Section 4.2.2.7) was used at these points. Various sizes of the enclosure and distance from the inlet were tested to obtain a similar incident speed on the front face of the plate as in the wind tunnel experiments (91.11kmph at the max speed of 108kmph).

Simulations were carried out again to prove that measuring dynamic pressure at those specific points yields a similar pressure drop for both the experimental and simulation results. After testing various sizes of the enclosure and distance of the inlet from the testbench, it was found that an inlet distance of 452mm gave an almost exact replication of the airflow speed striking the plate's front surface (91.23kmph). The side plates were added to the testbench design to make the simulation conditions as close to the real experimental testing as possible. The walls of this enclosure were kept at 1mm from the sides and the top so that most of the airflow passes through the testbench like before. However, the bottom wall was kept at 130mm from the testbench, which is the ground clearance of the testbench in real life.

The refined mesh setup is shown in Fig G.1 and G.2 while the dynamic pressure measuring points at the front and rear surface of the final pressure plate design are shown in Fig G.3 and G.4, respectively.

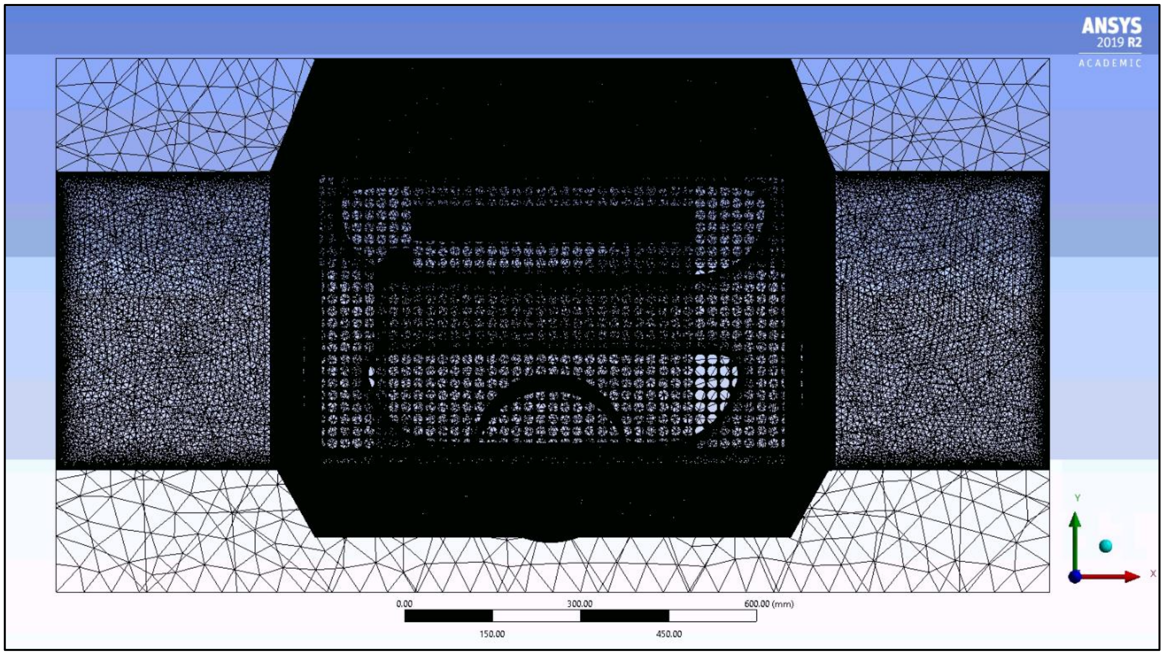

Figure G.1 Refined mesh setup - front view

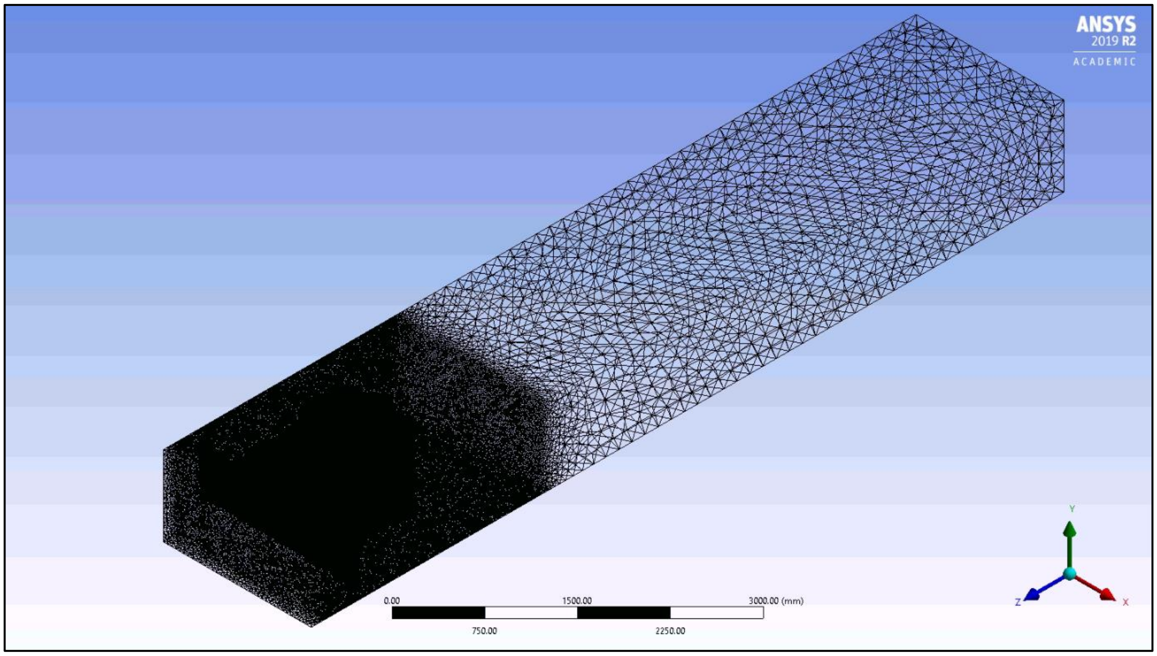

Figure G.2 Refined mesh setup - isometric view

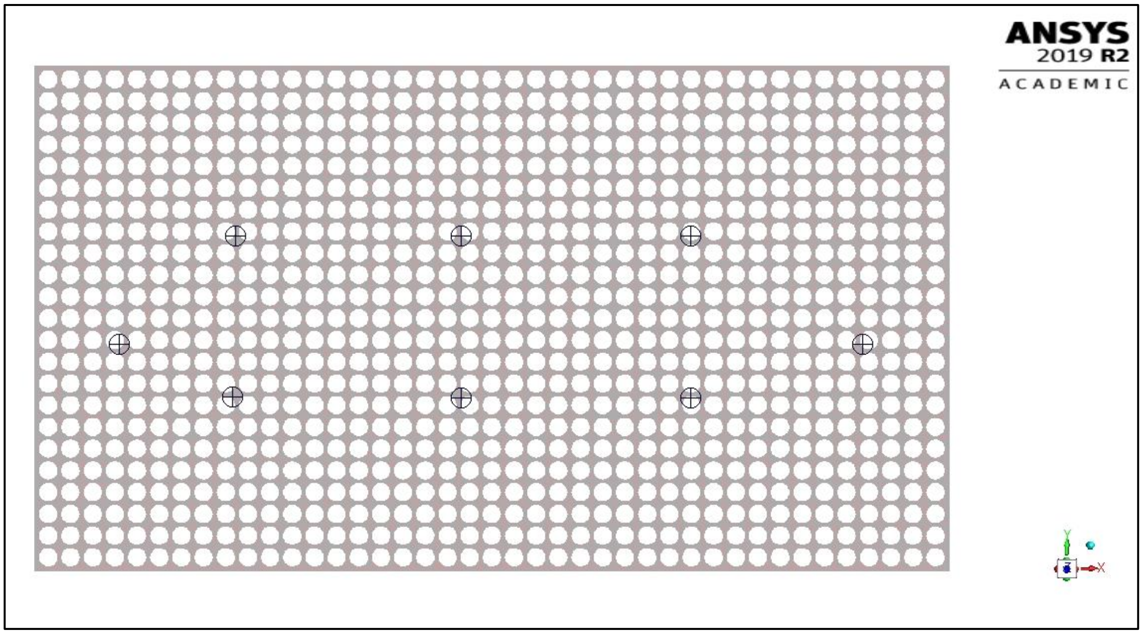

Figure G.3 Dynamic pressure measuring points at the front of final pressure plate

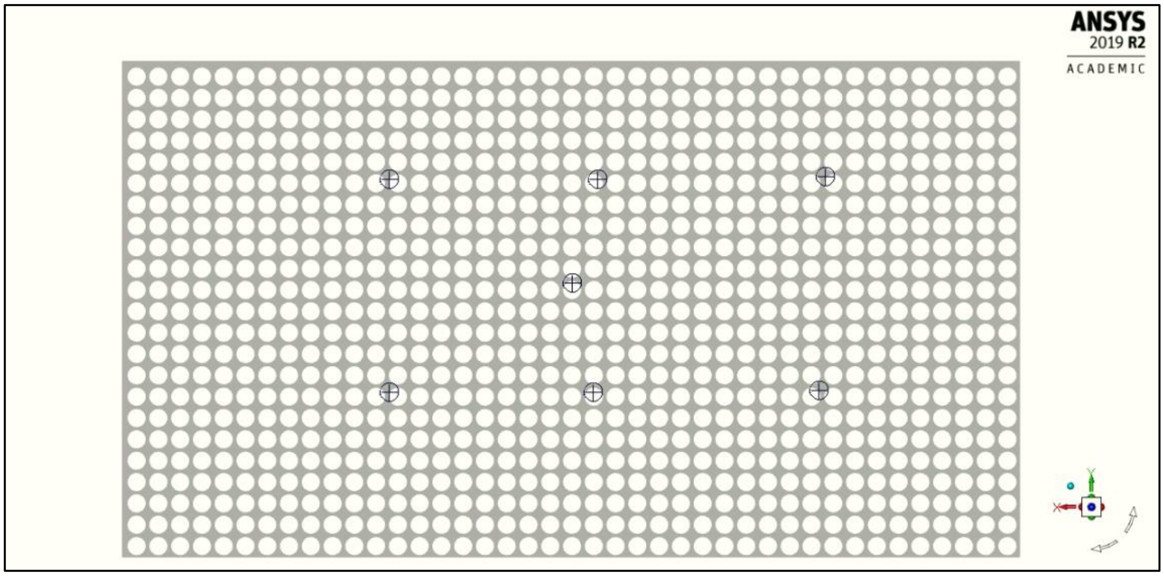

Figure G.4 Dynamic pressure measuring points at the rear of final pressure plate

Appendix H – Coefficient of pressure (C_p)

The change in dynamic pressure values (ΔQ) were converted into terms of the coefficient of pressure (C_p). Since C_p is a dimensionless quantity, it provides more generic results that are applicable to different scenarios. For calculating C_p, the ΔQ values for the test vehicle and the sealed and unsealed testbench were divided by the dynamic pressure value measured at the nozzle of the wind tunnel as shown in the equation below:

$$C_p = \frac{\Delta Q}{Q} \tag{H.1}$$

The graphs for the AGS open, partially open, and closed case are thus plotted between C_p and the wind speed.

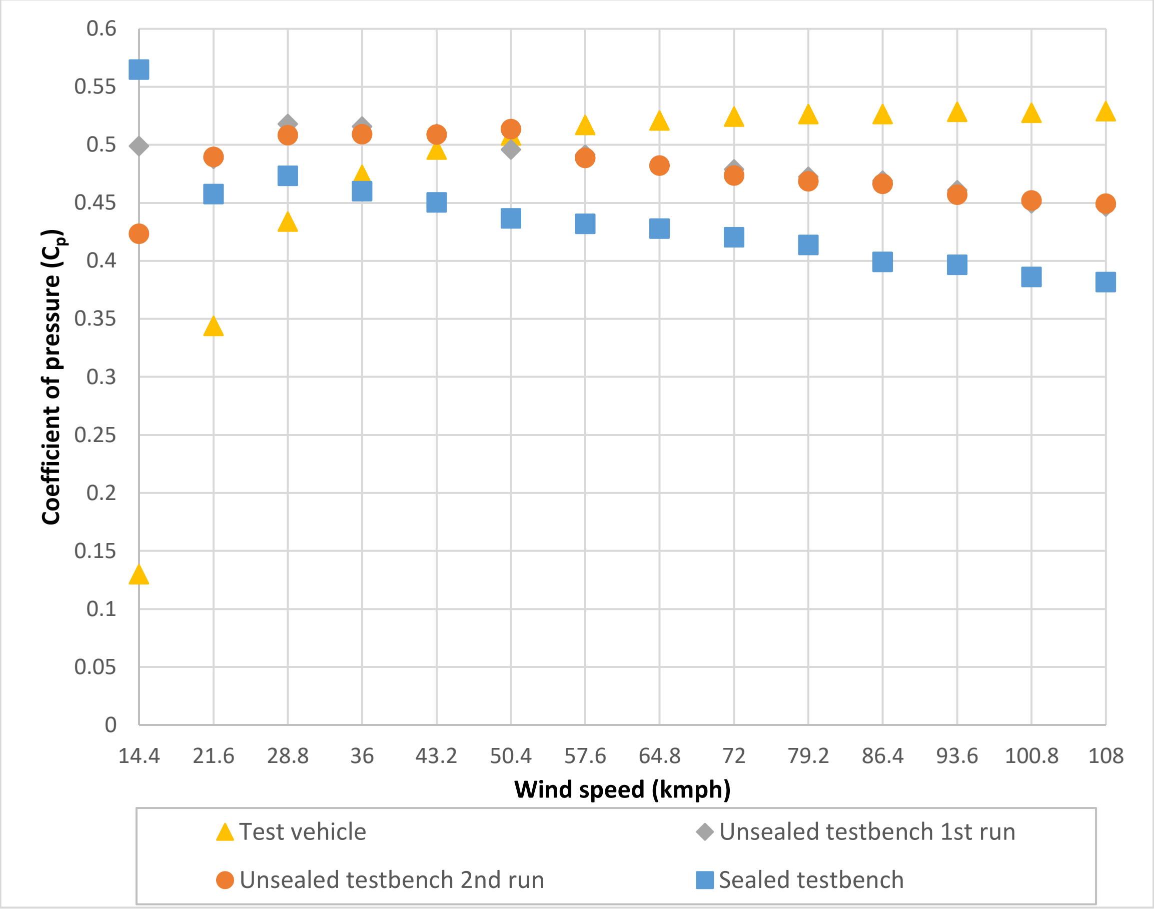

Figure H.1 Coefficient of pressure (C_p) behind the AGS vs wind speed (AGS open)

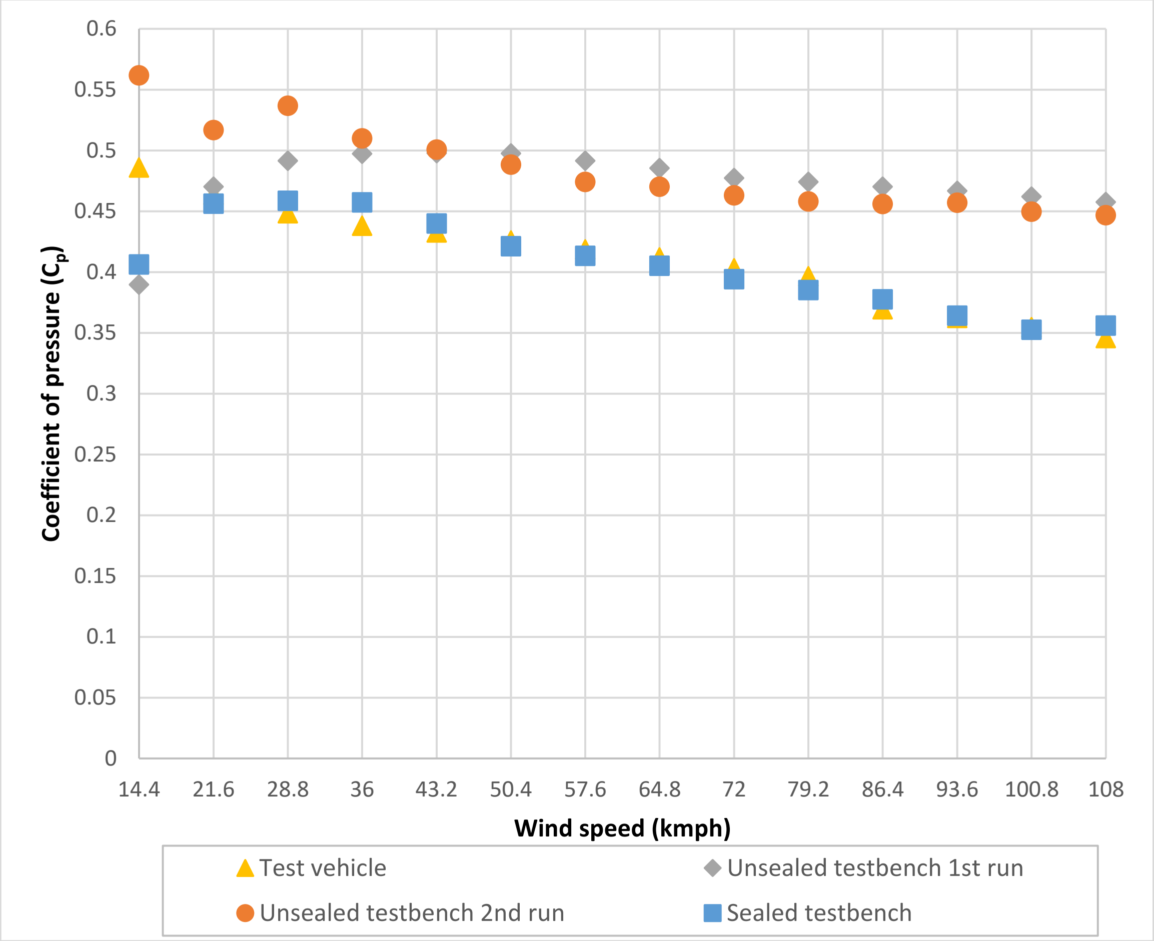

Figure H.2 Coefficient of pressure (C_p) behind the AGS vs wind speed (AGS partially open)

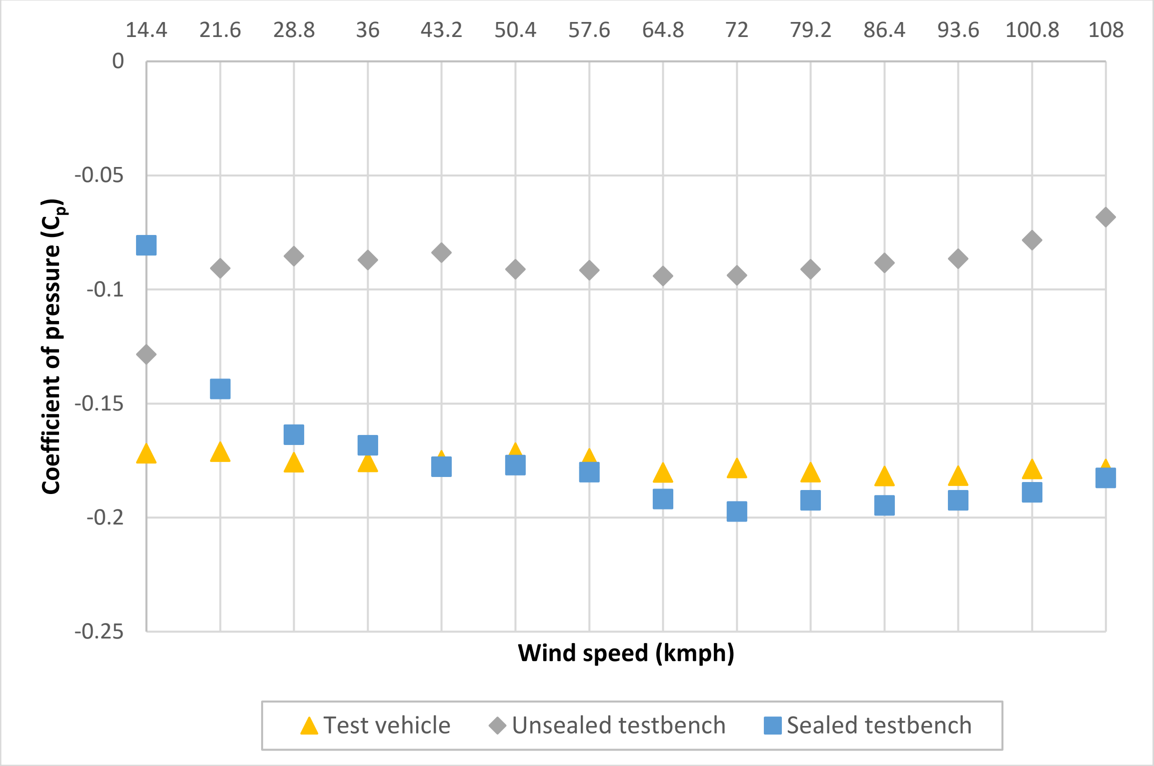

Figure H.3 Coefficient of pressure (C_p) behind the AGS vs wind speed (AGS closed)